Karlsruhe Institute of Technology (KIT)

Master Thesis

Thermodynamic Design of a Cryostat for a Radiofrequency Cavity Detector in BabyIAXO in Search of Dark Matter

Marc Siodlaczek

11th March, 2022

Assignment: Prof. Dr.-Ing. Steffen Grohmann
Supervision: Dr. rer. nat. Torsten Koettig
Dr. rer. nat. Babette Döbrich

Karlsruhe Institute of Technology

Institute of Technical Thermodynamics and Refrigeration
Organisational Unit: Refrigeration and Cryogenics
Prof. Dr.-Ing. Steffen Grohmann

Master thesis

for Mr. B.Sc. Marc Siodlaczek

Thermodynamic Design of a Cryostat for a Radiofrequency Cavity Detector in BabyIAXO in Search of Dark Matter

Thermodynamisches Design eines Kryostaten für einen Radiofrequenz Hohlraumdetektor in BabyIAXO auf der Suche nach Dunkler Materie

Background:

BabyIAXO is a demonstrator of the proposed full-size IAXO (International Axion Observatory). It is currently undergoing design and once installed, it will search for axions or axion-like particles originating from the sun. Axions can transform into photons in the presence of a significant magnetic field, and then be detected. The superconducting magnets of BabyIAXO generate an average magnetic field of 2.1 T in two 10 m long and 700 mm diameter bores.

Another way to detect Axions, if they are Dark Matter, is to look for their conversion to photons inside a resonating cavity. The emerged photon resonates in a specific frequency measurable in the cavity. It is planned to install one or multiple cavities inside one bore of BabyIAXO in a later stage. Presently, the bores are planned to be operated at room temperature, but low temperature is enabling a lower thermal noise, a higher figure of merit and allows the use of superconducting layers inside the cavity. Thus, the need for a cryostat to reach low enough bore temperatures arises.

The special and stringent internal and external requirements ask for a custom-made cryostat design.

Scope of work:

This Master thesis contributes to the design and the dimensioning of a cryostat for the BabyIAXO radio frequency resonant body detector, including the following work packages:

- familiarization with the BabyIAXO and RADES experiments,
- evaluation of the heat loads,
- thermodynamic design of a cooling method fulfilling the internal and external requirements,
- mathematical model of the cooling system,
- participation in cryogenic testing of remote cooling systems,
- inputs for the modelling of the cryostat in a CAD program.

Karlsruhe Institute of Technology

Institute of Technical Thermodynamics and Refrigeration
Organisational Unit: Refrigeration and Cryogenics
Prof. Dr.-Ing. Steffen Grohmann

The work will be carried out at CERN, Geneva, Switzerland. The results of the investigations are to be documented in a Master thesis written in English language. A two-sided summary in German shall be submitted together with the thesis. In addition, the results shall be presented in the ITTK Institute seminar at KIT.

The rules for safeguarding good scientific practice at KIT shall be applied.

Start of work: 01.09.2021

Thesis submission:

Supervisor: Dr. Torsten Koettig (CERN, TE Department, Cryogenics Group, torsten.koettig@cern.ch)

Prof. Dr.-Ing. Steffen Grohmann

Declaration of Originality

I hereby declare that I have composed this paper by myself and without any assistance other than the sources given in my list of works cited. This paper has not been submitted in the past or is currently being submitted to any other examination institution. It has not been published. All direct quotes as well as indirect quotes which in phrasing or original idea have been taken from a different text (written or otherwise) have been marked as such clearly and in each single instance under a precise specification of the source. The charter of the Karlsruhe Institute of Technology (KIT) for safeguarding good scientific practice in the currently valid version was followed. I am aware that any false claim made here results in failing the examination.

Karlsruhe, 11th March, 2022

Marc Siodlaczek

Abstract

Despite compelling evidence, dark matter (DM) has still not been directly detected yet. The promising DM candidate, the axion particle, is searched for by the International Axion Observatory (IAXO). BabyIAXO is the demonstrator of IAXO and will be built in the near future. The Relic Axion Detector Exploratory Setup (RADES) plans on installing a 10 m long resonant cavity detector at BabyIAXO. This serves as an additional experiment in BabyIAXO, which probes unexplored axion parameter space and for which low temperatures are stringent for the success of the operation. Thus, the need for a cryostat arises that fulfills the requirements of a dry cryostat, the operation in a low-temperature and magnetic field environment, and the low-interference with the sensitive measurements. This work develops a first design of the cryostat which is based on the cryocooler remote cooling via a closed circulation loop of helium. The heat loads of the components are estimated and a thermodynamic model of the cooling system is compiled. An experiment imitating the present system is conducted at the European Organization for Nuclear Research (CERN) as proof-of-concept and compared with the model. The operation of the experiment reveals a substantial background heat load and a susceptibility for thermal acoustic oscillations (TAOs), which is why the envisioned low temperature regime is not reached. Nevertheless, the remaining data suggest a satisfactory operation of the cooling system and an acceptable agreement of the temperature levels of the experimental setup and the thermodynamic model. Especially, the intermediate temperatures and the cryogenic circulator can be portrayed sufficiently. Thus, for now, the predictions of the thermodynamic model are cautiously trusted. The latter enables the optimization of the layout and operating parameters of the cooling system. The findings of the optimization are discussed in the present thesis. The present cooling system, consisting of two cryocoolers, a cryogenic circulator, a counter-flow heat exchanger (CFHX), and connecting cooling pipes, can reach cavity and low noise amplifier (LNA) temperatures of about 4.6 K. The results demonstrate the feasibility of the application of the resonant cavity detector in BabyIAXO. A more detailed design of the resonant cavity, the tuning mechanism, and the support structure inside the BabyIAXO bore seem exciting and are needed to progress in the cryostat design and to increase the accuracy of the model. Additionally, an electromagnetic and mechanical analysis must assess the influence of a quench of the BabyIAXO magnet on the present system.

Zusammenfassung

Trotz konkreter Anhaltspunkte für die Existenz Dunkler Materie (DM) ist es noch nicht gelungen diese direkt nachzuweisen, sowie die Bestandteile von DM zu ermitteln. Als ein vielversprechender DM-Kandidat gilt das postulierte Axion Partikel. Die Theorie des Axion Partikels geht aus einer möglichen Erweiterung des Standardmodels der Partikelphysik hervor, welche jedoch nicht die Masse und die Stärke der Wechselwirkungen des Axion Partikels festlegt. Daher existiert zunehmende Motivation das Axion Partikel experimentell nachweisen und seine Parameter, wie die Masse, zu bestimmen. Eines dieser Axion-Teleskope ist das International Axion Observatory (IAXO), das sich zurzeit in Planung befindet und mit welchem beträchtlicher unerschlossener Parameterraum abgedeckt werden soll. Der kleinere Demonstrator des IAXO, das sogenannte BabyIAXO, soll in den nächsten Jahren auf dem Gelände des Deutschen Elektronen-Synchrotron (DESY) gebaut werden. Die RADES-Gruppe (Relic Axions Detector Exploratory Setup) plant, ein 10 m langes Messgerät auf Basis von Hohlraumresonatoren zur Suche von DM-Axionen in BabyIAXO zu installieren. Dieses Messgerät ermöglicht weitere Experimente mit einem von BabyIAXO abweichenden Zielparameterraum. Um zufriedenstellende Messgenauigkeiten zu erzielen, die nicht durch thermisches Rauschen überdeckt werden, sind tiefe Temperaturen unter 10 K erforderlich. Diese Temperaturen sind mit einem 14 m langen Kryostaten zu erreichen, der die einzigartigen und strengen Anforderung des Experiments erfüllt. Hierfür muss ein trockener Kryostat bei tiefen Temperaturen in einem externen Magnetfeld, bei gleichzeitiger geringer Störung des hochpräzisen Experiments, betrieben werden. Die vorliegende Arbeit entwickelt ein erstes Design des Kryostaten, welcher auf Kryokühlern und der Fernkühlung durch einen geschlossenen Heliumzirkulationskreislauf basiert. Die parasitären Wärmeströme durch die Isolation und die Komponenten des Kühlsystems werden durch numerische Berechnungen abgeschätzt und ein thermodynamisches Modell des Kühlsystems wird entwickelt. Zusätzlich wird ein Experiment an der Europäischen Organisation für Kernforschung (CERN) durchgeführt, welches das geplante Kühlsystem imitiert und so als Machbarkeitsnachweis dient. Die experimentellen Daten werden mit dem Modell verglichen, um die Ergebnisse des eigenen entwickelten Modells zu validieren. Der Betrieb des Experiments zeigt eine erhebliche Hintergrundwärmebelastung und eine Anfälligkeit für thermoakustische Oszillationen, weshalb der angestrebte niedrige Temperaturbereich nicht erreicht wird. Dennoch deuten die Daten auf einen zufriedenstellenden Betrieb des Kühlsystems und eine akzeptable Übereinstimmung der Temperaturwerte mit dem thermodynamischen Modell hin, was motiviert den Aussagen des Modells vorsichtig zu vertrauen. Zukünftige geplante Messkampagnen am CERN müssen die Effektivität des Kühlsystems bestätigen. Mithilfe des Modells werden Layout und die Komponenten des Kühlsystems optimiert sowie die Betriebsparameter untersucht. Das da-

raus entstandene Kühlsystem aus zwei Kryokühlern, einem kryogenen Zirkulator, einem Gegenstrom-Wärmeübertrager, und den verbindenden Kühlrohren schafft es, den Hohlraumresonator und den rauscharmen Verstärker (LNA) auf ungefähr 4.6 K zu kühlen. Die vorgestellten Ergebnisse sprechen für die Durchführbarkeit der Installation und das Betreiben des Hohlraumresonatordetektors in BabyIAXO. Als nächste Schritte zur Konstruktion des Kryostaten sind das genauere Design der Hohlraumresonatoren, des Tuningsystems und der Tragkonstruktion von thermischem Schild und Hohlraumresonatoren in BabyIAXO von Seiten des RADES-Experiments erforderlich. Die genaue Auslegung der zuletzt genannten Punkte ermöglicht dann auch, die Genauigkeit des thermodynamischen Modells zu steigern. Außerdem ist eine elektromagnetische und mechanische Analyse des Einflusses eines Quenches des BabyIAXO-Magneten auf das geplante System unersetzlich.

Contents

Symbols and abbreviations

Symbols

Symbol (Latin)	Unit	Description
A	m^2	Area
B	T	External magnetic field
C	-	Geometrical form factor
c_p	$\mathrm{J/(kg\,K)}$	Isobaric specific heat capacity
d	m	Diameter
E	-	Effective emissivity
F	m^6	Figure of merit
g	$\mathrm{m/s}^2$	Gravitational acceleration constant
$g_{\mathrm{a}\gamma}$	1/eV	Axion photon coupling constant
h	J/kg	Mass specific enthalpy
i	-	Integer denoting the present volume element
I	A	Current
l	m	Length
$\dot{m}$	$\mathrm{kg/(m^2\,s)}$	Mass flux
$\dot{M}$	kg/s	Mass flow rate
$\widetilde{M}$	kg/mol	Molecular weight
m_a	kg	Mass of the axion
N	-	Integer denoting the total amount of e.g. volume elements
p	Pa	Pressure
Q	-	Quality factor
$\dot{q}$	$\mathrm{W/m}^2$	Heat flux
$\dot{Q}$	W	Heat flow
r	m	Radius
R	Ω	Resistance
R_gas	$\mathrm{J/(mol\,K)}$	Gas constant
t	m	Thickness
T	K	Temperature
T_sys	K	Detection noise temperature

Symbol (Latin)	Unit	Description
u	m/s	Velocity
U	V	Voltage
x	m	Spatial coordinate

Symbol (Greek)	Unit	Description
α	-	Accommodation coefficient
α_{eff}	$\mathrm{W/(m^2\,K)}$	Effective heat transfer coefficient
β	1/K	Isobaric expansivity
β_{cond} / β_{rad}	$\mathrm{W/(m^2\,K^2)}$ / $\mathrm{W/(m^2\,K^4)}$	Empirical corrective factor
γ	-	Heat capacity ratio
ε	-	Emissivity coefficient
$\varepsilon_{\text{CFHX}}$	-	Effectiveness of the CFHX
ζ	-	Darcy friction factor
λ	$\mathrm{W/(m\,K)}$	Thermal conductivity coefficient
Λ	$\mathrm{W\,K/m^2}$	Thermal boundary conductance
Λ_{l}	m	Mean free path
μ_{JT}	K/Pa	Joule–Thomson coefficient
ρ	$\mathrm{kg/m^3}$	Density
σ	$\mathrm{W/(m^2\,K^4)}$	Stefan-Boltzmann constant
σ_{yield}	Pa	Yield strength
τ_{relax}	-	Relaxation factor
χ	1/Pa	Isothermal compressibility

Abbreviations

Abbreviation	Description
ABC	Atomic recombination and deexcitation, Bremsstrahlung, Compton
ADMX	Axion Dark Matter Experiment
ALP	Axion-like particle
ALPS	Any Light Particle Search
AWG	American Wire Gauge
BIPM	Bureau international des poids et mesures (english: International Bureau of Weights and Measures)
CAST	CERN Axion Solar Telescope
CCCL	CERN Central Cryogenic Laboratory
CERN	Conseil Européen pour la Recherche Nucléaire (english: European Organization for Nuclear Research)
CFHX	Counter-flow heat exchanger
CM	Cold mass
CMB	Cosmic microwave background
COP	Coefficient of performance
DAQ	Data acquisition
DC	Direct current
DESY	Deutsches Elektronen-Synchrotron (english: German Electron Synchrotron)
DM	Dark matter
DFSZ	Dine-Fischler-Srednicki-Zhitnitsky
GM	Gifford-McMahon
HERA	Hadron-Electron Ring Accelerator
HEX	Heat exchanger
HP	High-pressure
IAXO	International Axion Observatory
KSVZ	Kim-Shifman-Vainshtein-Zakharov
LHC	Large Hadron Collider
LNA	Low noise amplifier
LP	Low-pressure
LSW	Light shining through a wall
MACHO	Massive astrophysical compact halo object
MADMAX	Magnetized Disc and Mirror Axion experiment
MLI	Multilayer insulation
NIST	National Institute of Standards and Technology
PID	Proportional–integral–derivative

Abbreviation	Description
P&ID	Piping and instrumentation diagram
PTFE	Polytetrafluoroethylene
RADES	Relic Axion Detector Exploratory Setup
RTD	Resistance temperature detector
QCD	Quantum chromodynamics
RF	Radio frequency
SM	Standard Model
SPB	Silver plated brass
SRF	Superconducting radio frequency
SST	Stainless steel
TAO	Thermal acoustic oscillation
TS	Thermal shield
VC	Vacuum chamber
VNA	Vector network analyzer
WIMP	Weakly interacting massive particle

1 Introduction

Dark matter (DM) denotes the hypothetical form of matter of which the universe is supposed to mainly consist of [1]. The evidence for the existence of DM seems compelling, though, it still has not been directly detected yet [1, 2]. Multiple theories exist that explain the existence and phenomena of DM by proposing a new particle. Promising DM candidates are the axion and the axion-like particle (ALP), that could even help explaining further astrophysical and cosmological phenomena [3, 4]. The experimental efforts for the search of axions and ALPs are increasing due to its convincing physics potential [4]. The largest experimental collaboration in axion physics plans on constructing the International Axion Observatory (IAXO), which is currently undergoing design [5]. BabyIAXO is the demonstrator of the full-size IAXO and its construction is planned to begin in the next few years at the German Electron Synchrotron (DESY). In addition to test the magnet and detectors at a technically representative scale for IAXO, BabyIAXO will probe an unexplored parameter space, and, thus, a discovery is already possible at this stage [6]. BabyIAXO and IAXO will primarily search for axions and ALPs originating from the Sun, that can transform into photons in the presence of a magnetic field, and then be detected [5]. For this purpose BabyIAXO will accommodate two 11 m long, 70 cm diameter bores that are enclosed by superconducting magnets generating an average magnetic field of 2.1 T. Another way of detecting axions that do not originate from the Sun but may constitute DM is pursued by the Relic Axion Detector Exploratory Setup (RADES) project [7]. There, a passing axion from the postulated local DM galactic halo converts into photons inside a resonating cavity [4]. The photon that emerges from the axion-photon conversion then resonates in a specific frequency, measurable in the cavity. It is planned to install one or multiple cavities inside one bore of BabyIAXO at a later stage thus pursuing the operation of a second experiment in BabyIAXO which can explore additional unrevealed axion sensitivities. The bores of BabyIAXO will not be actively cooled, but low temperatures would enable a lower thermal noise and a higher figure of merit for the RADES detection strategy. Additionally, low temperature operation enables the application of superconducting layers inside the cavity [8]. Therefore, the need for a cryostat to reach cavity temperatures $< 10\,\mathrm{K}$ arises. The special and stringent internal and external requirements for the cryostat include the necessity of a dry cryostat, the operation in a low-temperature, magnetic field environment, and the low-interference with the sensitive measurements.

This work aims to contribute to the design and the dimensioning of the cryostat for the BabyIAXO resonant cavity detector. A promising remote cooling method via an independent active circulation loop and a cryocooler is applied [9]. There, the heat is transported from the cooling interface by helium inside cooling pipes to the cryocooler in a more remote location outside the magnetic field.

An effective counter-flow heat exchanger (CFHX), currently in development [10] at the European Organization for Nuclear Research (CERN) at the CERN Central Cryogenic Laboratory (CCCL) is used to reach the required cooling performance at distance. The heat load and the influence of heat intercepts of all instrumentation is evaluated. The cooling system design, the thermodynamic performance and the respective optimization are investigated via a thermodynamic model of the system. A detailed study of optimal temperature of the thermal shield (TS) and the cold mass (CM) to the overall system effectiveness is conducted. The validity of the thermodynamic model itself is aimed to be evaluated with an experimental setup at the CCCL imitating the present system. Finally, a solution respecting the given physics and engineering parameters is proposed.

The present work is divided into eight chapters. Chapter 2 briefly introduces the theoretical background of dark matter, the axion particle and the axion and ALP searches, that are needed to understand the current experimental efforts. In Chapter 3 the status of the BabyIAXO project is described by introducing the aims of the IAXO collaboration and the RADES project. Chapter 4 provides an overview of the stringent requirements that the cryostat needs to fulfill and the possible cooling methods that were considered. Additionally, the remote cooling method as the most convincing option and the basic preliminary design of the cryostat are presented in more detail. The estimation of the heat loads as a design parameter of the cryostat is described in Chapter 5. This includes the discussion of the fundamental heat transfer mechanisms in vacuum and the numerical modeling of some components. Chapter 6 presents the approach of modeling the remote cooling system, with which the design of the cryostat can be optimized. Additionally, the experimental setup at the CCCL used to evaluate the validity of the thermodynamic model is presented. In Chapter 7 the results of the experimental investigation and the thermodynamic model are given. The temperatures to be expected, the findings of the optimization with the thermodynamic model, and the resulting design choices are discussed. Lastly, a brief conclusion and outlook is given in Chapter 8.

2 Theoretical motivation for dark matter and the axion particle

The following chapter shortly describes the theoretical background of dark matter and the postulated axion particle. It aims to give an understanding for the current experimental efforts like the BabyIAXO project. In order to grasp the theories fully, the reader is referred to the given references. First, the standard model of particle physics is introduced. Then, dark matter as the hypothetical form of matter which has not yet been directly detected is described in Section 2.1. Section 2.2 outlines the promising DM candidate, the postulated axion particle, and Section 2.3 relates the experimental searches for the axion particle.

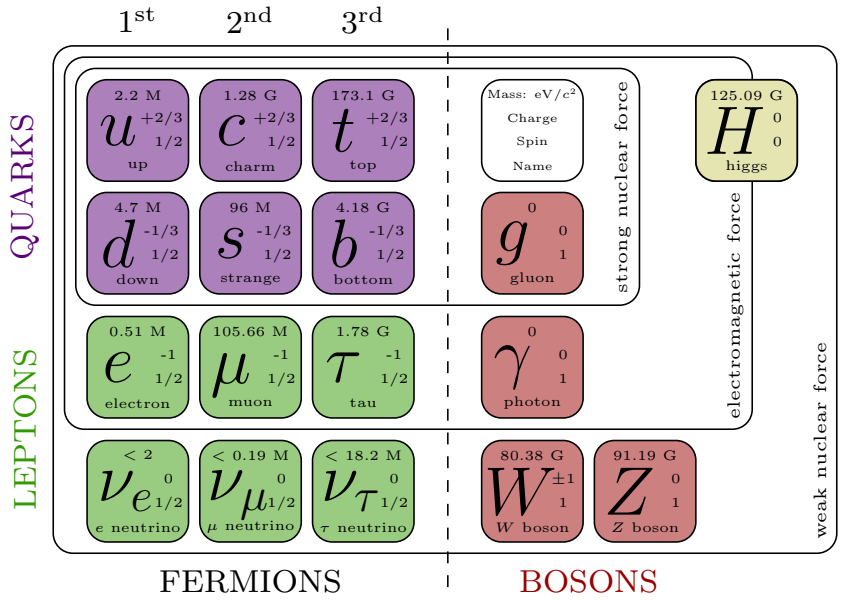

Figure 2.1: *The Standard Model of particle physics, classifying the known elementary particles. Image by Lubej [11].*

In physics there are four fundamental forces known to exist: gravity, the electromagnetic force, the weak nuclear force and the strong nuclear force. Particle physics aims to explain these forces by studying the fundamental elements of matter and their interaction. The theory of the Standard Model (SM) is currently the most successful model in describing all the phenomena of particle physics [12].

A graphical representation of the particle content of the SM is depicted in Figure 2.1. The SM is based on the properties and the interactions of a small number of elementary particles, which can be divided into two groups (fermions and bosons) and four distinct types: quarks (purple), leptons (green), gauge bosons (red), and scalar bosons (yellow). Each particle behaves according to quantum properties and is characterized by its mass, electrical charge, and spin. Fermions generally constitute matter and bosons generally carry force. The electromagnetic force is conveyed by photons, the weak nuclear force by the vector bosons W and Z, and the strong nuclear force by gluons [1]. The last fundamental force – gravity – can, until now, not be described by quantum theories. This absence is one of the biggest gaps of the SM, next to other phenomena that the SM falls short on explaining, see e.g. [13]. However, the SM has been successful in describing experimental results and even predicting particles with great accuracy, which were later proven to exist. The most recent experimental confirmation was the detection of the Higgs boson with the Large Hadron Collider (LHC) at CERN in 2012 [14], which has zero spin and no electric charge but gives mass to the elementary particles [12]. The SM also does not contain any viable non-baryonic dark matter particle. A baryon is a type of composite subatomic particle that is made out of quarks and interacts mainly via the strong nuclear force [13]. The most familiar baryons are protons and neutrons, each containing three quarks. Electrons, on the other hand, are not baryons but leptons and do not interact via the strong nuclear force. Baryonic matter is therefore part of the ordinary matter experienced in everyday life, while dark matter must be non-baryonic that remains hidden [13]. Why dark matter is highly relevant and what it could be made of, is discussed in the next section.

2.1 Dark matter

Dark matter is the name of the hypothetical form of matter of which our universe is supposed to mainly consist of, next to stars, gas, and other known forms [13]. This non-baryonic matter emits and absorbs no sort of currently detectable radiation, yet bends space and time. Today the evidence for the existence of DM seems overwhelming. The most convincing proof can be drawn from the rotation curves of spiral galaxies, gravitational lensing, the dynamics of galaxy clusters, galactic mergers, and the cosmic microwave background (CMB) [1, 13]. The unexpected behavior of the rotation curves of spiral galaxies as evidence for DM was first reported on in 1970 by Freeman [15], interpreting the data from Rubin and Kent [16]. A star, which has a distance r from the galactic center and tangential velocity u, behaves according to centrifugal and gravitational forces, exactly like the planets do in their orbits around the sun. The velocity distribution $u(r)$ outside the center is then expected to be proportional to $r^{-0.5}$. However, many rotation curves show an approximately constant $u(r)$ up to distances where the signal becomes too weak to measure [2]. This can so far only be explained coherently by a dark matter halo constituting most of the mass. Another interesting phenomenon is gravitational lensing: if a massive object lies between a distant star and an observer, the gravitational field deflects the light and acts as convergent lens. At perfect alignment the observer would see the star spread out into a ring, known as an Einstein ring [1]. Due to the deflection angle depending on

the lensing mass, the masses of galaxies have been observed to exceed their ordinary-matter mass by an order of magnitude [2].

When searching for a DM candidate a few restrictions apply: the DM candidates should account for about 85 % of the total matter content of the universe (according to the standard ΛCDM model [17, 18]) and explain the phenomena mentioned above. It should be a neutral particle, stable on the cosmological time scale, have mass, and have gravitational interactions with baryonic matter [19]. There exist multiple theories which take into account the existence of dark matter and propose a possible candidate. However, dark matter does not need to be made of just one of these candidates. The following mentioned DM candidates reveal by far no complete list and should only illustrate the existing wide range. One of the first candidates were massive compact halo objects (MACHOs) [20, 21], which are ordinary baryonic matter that do not shine. Through experimental evidence, which is gathered by taking advantage of gravitational lensing, it seems like MACHOs can be ruled out as the sole contender for dark matter [1]. Other candidates are neutrinos, which were also experimentally dismissed as a major contributor for DM [1], and weakly interacting massive particles (WIMPs). WIMPs are among the best motivated DM candidates as possible extensions of the SM independently predict particles with the right density to be dark matter and experiments today still do not exclude their existence [22]. At last there are also theories present, that postulate Kaluza-Klein particles [23, 24], which can propagate through extra dimensions. In this work the focus lies on the axion particle which originates from a proposed SM extension and is also an excellent DM candidate. The axion will be introduced in the following Section 2.2.

2.2 Axion particle

The axion particle emerged as a possible solution for the so-called strong CP problem in quantum chromodynamics (QCD). QCD is the theory of the strong nuclear interactions in the SM. A characteristic of QCD is that each of the six flavors or types of quark has the additional quantum number "color" [13]. The strong CP problem consists of the question of why QCD seems to preserve CP symmetry for the strong interactions. CP symmetry stands for charge conjugation (C) parity (P) symmetry. It states that the laws of physics should be the same if a particle were swapped with its antiparticle (C) and the sign of its spatial coordinates inverted (P). A non-conformity would be called symmetry breaking, which was already experimentally measured for the CP symmetry for the weak interactions [25]. According to the current formulation of QCD, a CP symmetry breaking in the strong interactions could and thereby should occur as well. However, no violation of the CP symmetry in the strong interactions has been observed in any experiment.

The most well-known and compelling solution to the strong CP problem is the Peccei-Quinn (PQ) theory [26, 27], which is an extension of the SM. Shortly after its publication, Weinberg [28] and Wilczek [29] independently realized that this solution implied a new boson particle, which Wilczek named axion after the laundry detergent of the same name because it "cleaned up" a problem with

an "axial" current [30]. The original PQ proposal was ruled out by experiments but it gave rise to the new axion particle looking to be found and explained in a model. Some properties of the axion are determined by the PQ mechanism and therefore independent of the model. For example the existing theory does not fix the value of the axion's mass m_a itself, but the strength of the axion's interactions must be proportional to its mass [4]. This creates a restricted parameter space, in which an axion could be detected. Nowadays, there are two benchmark models integrating the axion: the KSVZ model by Kim [31] and Shifman, Vainsthein, and Zakharov [32] and the DFSZ model by Dine, Fischler, and Srednicki [33] and Zhitnitsky [34]. Many more models can be closely related to either KSVZ or DFSZ and a review of them can be found in [35, 36].

Experimentally, the most important interaction of an axion would be its coupling to two photons with the coupling constant $g_{a\gamma}$ via the electromagnetic force [12]. This coupling is utilized in many axion searches where an axion, according to the inverse Primakoff effect [37, 38], would convert into two photons in the presence of a strong electromagnetic field. Due to the importance of the axion-photon interaction and also its generality in the axion models, the currently explored and unexplored $g_{a\gamma}$-m_a parameter space of a possible axion is depicted in Figure 2.2. The already explored parameter space is marked with different colors and the names of the experiments. The yellow band represents the standard QCD axion models and the brown lines the benchmark KSVZ and DFSZ models. Therefore the area of the yellow band is the most compelling and the aim of the sensitivity of experimental efforts. Here it should be pointed out that the dependency of the axion's mass and interaction strength is clearly visible in the slope of the yellow band. Additionally, there are models proposing an axion-like particle (ALP). The ALP is related to the axion but not to the PQ mechanism, which is why the ALP enjoys fewer model constraints than the axion [4]. Therefore an ALP could be found anywhere in the unexplored parameter space (see Figure 2.2).

Axions and ALPs are highly motivated as DM candidates but they could also help explain many astrophysical and cosmological phenomena like inflation, dark radiation, dark energy, anomalous cooling of stellar objects and soft X-ray excess from galaxy clusters [3, 4]. They could be produced in stars like the sun or could have been created shortly after the Big Bang, which are then called relic axions. The axions from the sun mainly form according to the Primakoff effect by the conversion of photons in the electromagnetic fields of the solar plasma [37]. This again depends on the axion-photon coupling $g_{a\gamma}$. Additionally there could be other production mechanisms called ABC (atomic recombination and deexcitation, Bremsstrahlung, and Compton) reactions [40]. The relic axion production is based on the vacuum realignment mechanism and, depending on the model, also on the production from global strings and from the decay of string-wall systems [3]. Relic axions could then have concentrated within the galaxies and galaxy clusters and be passing through the earth without interacting with ordinary matter. Since there are different axion and ALP origins and properties depending on the specific model, multiple detection strategies exist, of which the major ones are presented below in Section 2.3.

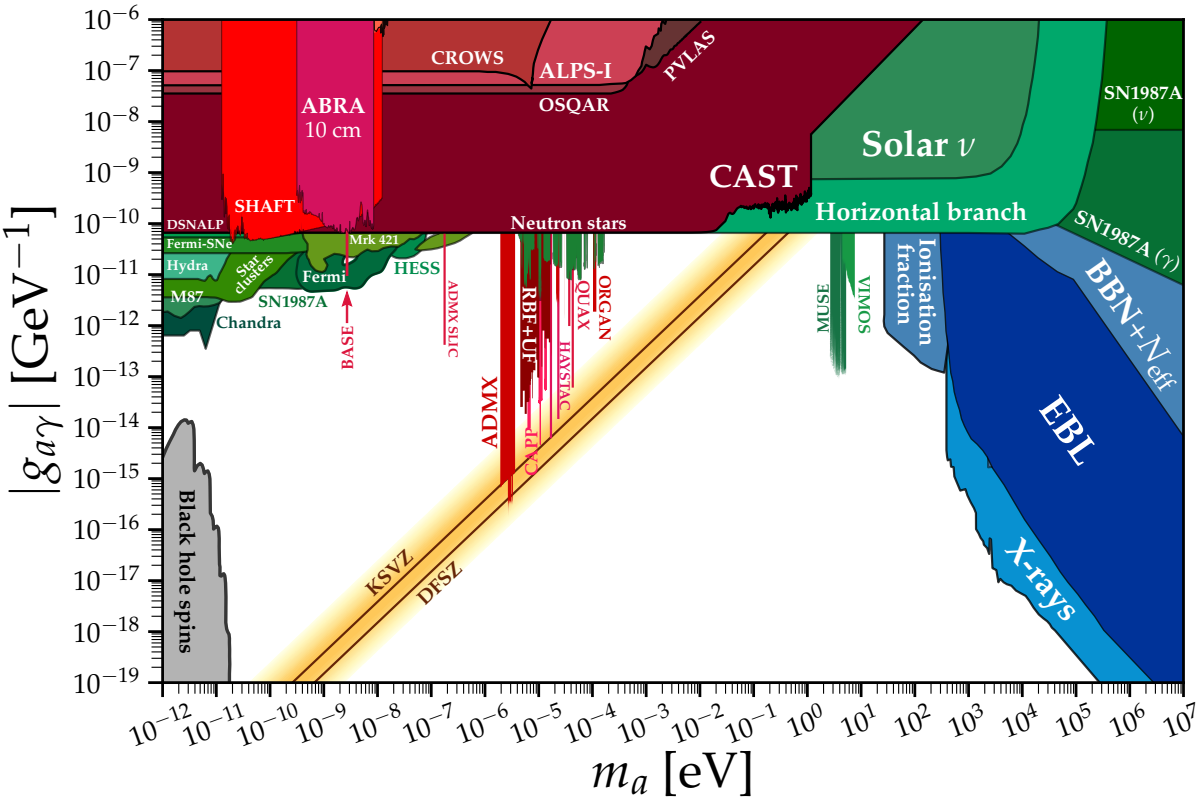

Figure 2.2: *Limit compilation by O'Hare [39] for the axion-photon coupling of current experiments and astrophysical data. The limits are depicted in the $g_{a\gamma}$-m_a parameter space. The yellow band represents the standard QCD axion models and the brown lines the benchmark KSVZ and DFSZ models.*

2.3 Axion and ALP searches

The experimental efforts of axion and ALP searches are growing in diversity and size of the projects as present technology allows to increasingly advance into the promising sensitivity ranges of the standard axion models. An extensive review of the experimental approaches can be found in the work of Irastorza and Redondo [35]; here, only a few characteristic examples, related to the present project, are given. The present work focuses on the strategies to directly detect axions in contrast to the detection of signatures of axions in cosmology or astrophysics. The most prominent detection strategies rely on the use of strong magnetic fields where axions can convert into photons, by the inverse Primakoff effect [37], which can be subsequently detected [6]. According to Irastorza [4] the experiments can be divided into three sorts, distinguishable by their assumed source of the axion:

- experiments looking for axions produced entirely in the laboratory,
- experiments aiming to detect axions emitted by the sun, called axion helioscopes,

- experiments searching for axions that constitute our local DM galactic halo, called axion haloscopes.

Purely laboratory based experiments do not rely on astrophysical or cosmological assumptions, however their sensitivity is limited by the very rare photon-axion-photon conversion in the installation thus not reaching QCD axion couplings sensitivity so far [35]. The most well-known idea is the light shining through walls (LSW) approach, where a powerful beam of photons (laser) is placed in a magnetic field with a wall in the middle of the line. Axions and ALPs spontaneously created on the side of the light source can travel through the wall and then reconvert into photons on the other side to be detected [4]. The Any Light Particle Search (ALPS) [41] experiment at DESY is making use of this concept and the ALPS-II [42] is currently finishing construction.

The other two approaches aim for the enormous flux of axions expected from extraterrestrial sources, with the difference that the helioscope has to follow the sun. The most sensitive existing helioscope is still the CERN Axion Solar Telescope (CAST) [43, 44], which consists of a 10 m long superconducting LHC prototype dipole magnet, providing an external magnetic field of up to 9 T, and X-ray detectors to search for converted photons. The IAXO collaboration mainly focuses on building a new helioscope, which will be outlined in the following Section 3.1.

A great variety of approaches exists for axion haloscopes. The conventional axion haloscope setup by Sikivie [38] applies a high quality factor resonant cavity inside a magnet in which the axion can convert into photons. If the resonant frequency of the cavity matches that of the axion, the conversion and ergo the signal is amplified. As the mass of the axion is not known, the resonant frequency of the cavity needs to be tunable to scan the parameter space. The Axion Dark Matter Experiment (ADMX) [45, 46] project is the leading effort for this technique at the moment. Their main setup includes a 60 cm diameter, 1 m long cavity with dielectric tuning rods inside a 8 T magnet. The RADES group is also researching an axion haloscope method based on a resonating cavity, which will be explained further in Section 3.2. Many other additional ideas are explored at the moment, for example the idea of a dielectric haloscope by e.g., the Magnetized Disc and Mirror Axion experiment (MADMAX) [47–49], where a dish antenna concept is utilized.

3 Fundamentals of BabyIAXO

The following chapter describes the origin and the current state of the IAXO project to enable the understanding of the later discussion and requirements of the cryostat. Section 3.1 introduces the IAXO collaboration and their experimental goals. Following this, the research area of RADES which is a subgroup of the IAXO collaboration is described in Section 3.2. In Section 3.3, the motivation for applying cryogenic systems in general and in similar projects is outlined.

3.1 Road to IAXO

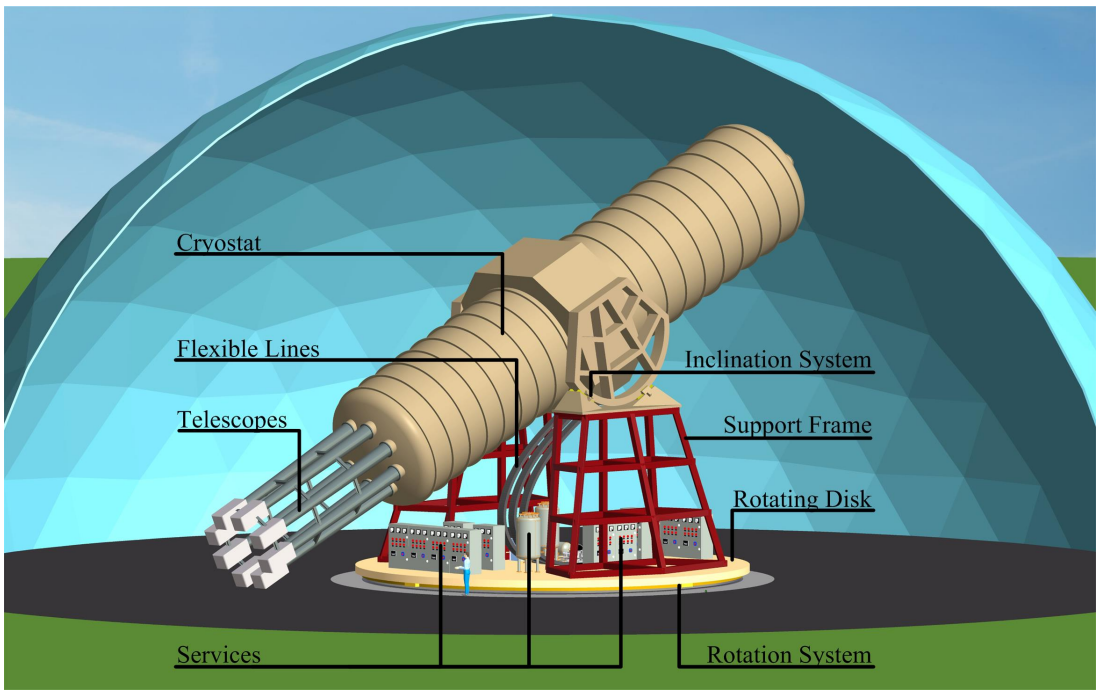

Figure 3.1: *Conceptual sketch of the IAXO helioscope from the conceptual design report. The most important components are labeled. The size of the system can be appreciated from the human figure standing next to it. Picture taken from [5].*

The successful operation of CAST established a sensitivity improvement on previous experiments and constraints on weakly interacting axions were established, however no axion was found. Consequently the plan emerged to build a stronger axion helioscope to detect even weaker interacting axions. For that, all helioscope projects are combined in the IAXO collaboration, the largest experimental collaboration in axion physics, with currently about 125 scientists from 25 different institutes participating. In 2011 the first feasibility study was published, where it was outlined how large improvements in magnetic field volume, optics, and detector with respect to CAST are possible [50]. The enormous physics potential and a detailed explanation of the theoretical, cosmological and astrophysical motivation of IAXO was reviewed and published in 2019 [3]. The whole project is divided into multiple stages. First, an intermediate experimental stage called BabyIAXO [6] will be constructed. BabyIAXO serves as a test version of the components at a technically representative scale for the full IAXO helioscope. Simultaneously, it will work as a fully functional helioscope with sensitivities beyond CAST and the option to detect axions or ALPs. It will be located at DESY in one of the old halls from the Hadron-Electron Ring Accelerator (HERA) and is expected to be built in two to three years. The goal of the collaboration is to build and operate the IAXO helioscope and a conceptual design was published in 2014 [5]. Possible updates to the IAXO helioscope are collected in IAXO+. The projected sensitivities of these experiments are shown in the limit compilation plot by O'Hare [39] in Figure 3.2. Figure 3.2 is a close up of Figure 2.2 and demonstrates the substantial amount of unexplored parameter space that the experiments of the IAXO collaboration will probe. Conceptual sketches of the helioscopes IAXO and BabyIAXO are depicted in Figure 3.1 and Figure 3.3, respectively.

BabyIAXO is designed as an axion helioscope but offers excellent properties to be used as an axion haloscope as well. This is the aim of the RADES project, which plans on operating BabyIAXO as an haloscope in a later stage in order to apply a second detection strategy at low additional costs. The RADES project and its ideas are presented below in Section 3.2.

3.2 Idea of RADES

The RADES project focuses on developing axion haloscopes for dipole magnets based on resonant cavities [7]. This includes research and development of the geometrical cavity design [51–53] and the coating of the cavity surfaces [8], while already producing relevant results [54, 55]. The goal of this effort is to take data in the BabyIAXO magnet in the future. In order to understand the unique characteristics of RADES and the motivation of using BabyIAXO as a haloscope, first, the properties of the conventional haloscope detection method by Sikivie [38] are explored further.

The axion signal power is enhanced in the resonant cavity if its resonance frequency corresponds to that of the axion mass tested. Since the axion mass is not known the cavity must be tunable in frequency to explore the parameter space. The scanning procedure then includes an exposure time at a fixed frequency before moving on to the next one. Furthermore, the level of noise fluctuations

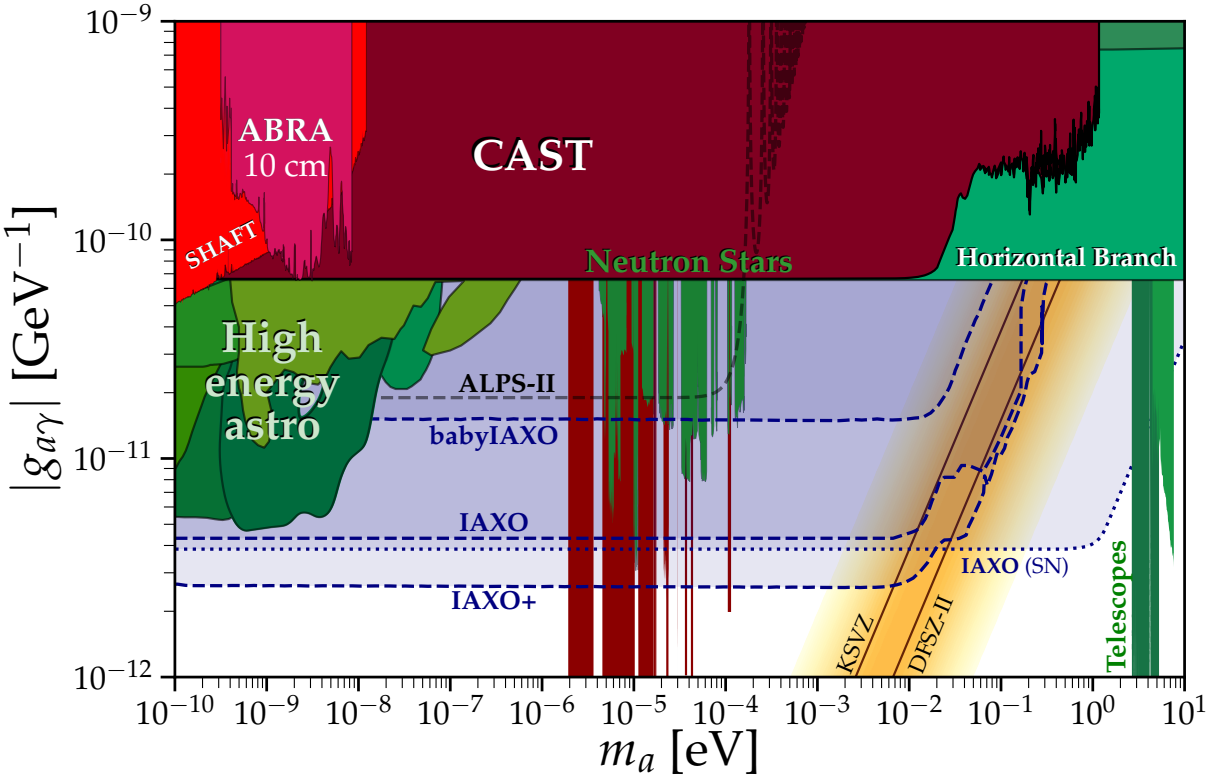

Figure 3.2: *Limit compilation by O'Hare [39] for the axion-photon coupling of current (solid) and future (dashed) experiments with a focus on the helioscope experiments. The limits are depicted in the $g_{a\gamma}$-m_a parameter space. The yellow band represents the standard QCD axion models and the brown lines the benchmark KSVZ and DFSZ models.*

determines the ability of seeing an axion signal and therefore the required exposure time at each frequency [4]. The figure of merit F of such haloscope experiments can be correlated to the extracted axion power signal, which appears above the background thermal noise, or the time needed to scan a fixed mass range down to a given signal-to-noise ratio [4]. For a given axion-photon coupling the dependency of F reads

$$F \propto g_{a\gamma}^2 m_a^2 B^4 V^2 T_{sys}^{-2} C^2 Q \,, \tag{3.1}$$

where B denotes the external magnetic field (assumed constant over the cavity volume), V the magnetic cavity volume, T_{sys} the effective detection noise temperature, C the geometrical form factor of the cavity mode [51], and Q the quality factor of the cavity, related to the resonance bandwidth [51]. T_{sys} is driven by the physical cavity temperature and the noise temperature of the first low noise amplifier (LNA) but includes additional constituents from the data acquisition. With the aim of maximizing F this equation enables the optimization of the design and focusing on single influencing factors.

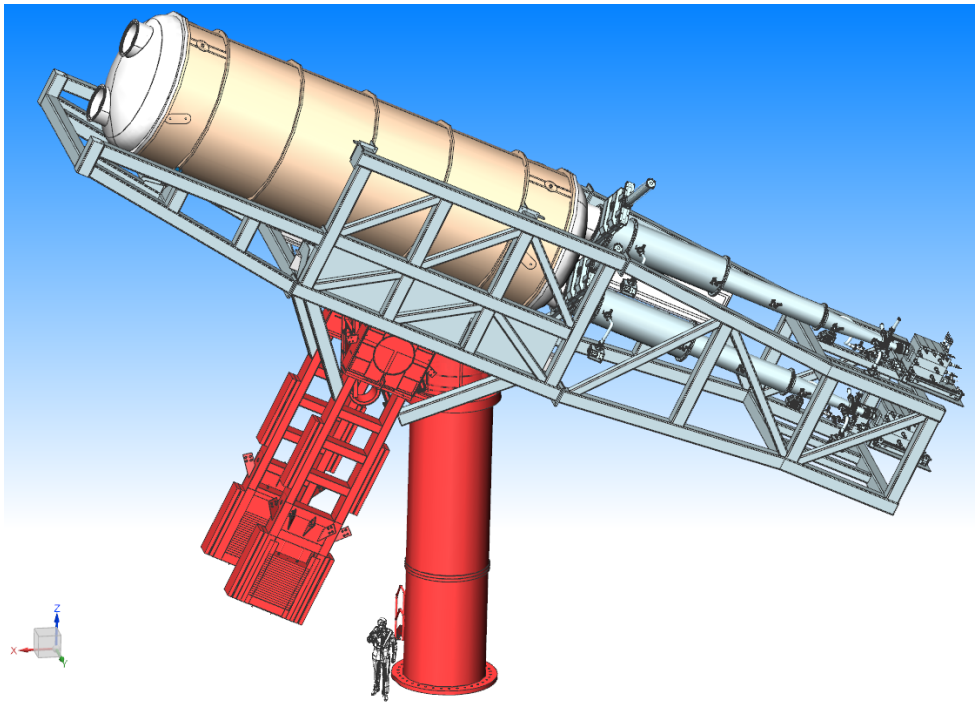

Figure 3.3: *Conceptual sketch of the BabyIAXO helioscope from 2021 including the magnet, cryostat, telescopes, detectors and support frame. Overall system length is about* 19 m. *Image taken from [6].*

One unique characteristic and the starting idea of RADES is its solution for the effective search for axions at high frequencies. High frequencies correspond to smaller resonant volumes V and lower quality factors Q. Unfortunately, the signal power decreases as the cavity's dimensions are reduced because it is both proportional to V and Q [7, 52]. The remedy is the novel design from RADES of a cavity structure with alternating irises. These irises allow a large volume while resonating at relatively high frequencies [52].

The motivation of utilizing BabyIAXO as a haloscope for RADES originates from its enormous dimensions. BabyIAXO allows one order of magnitude more volume in the external magnetic field than any existing setup (compare ADMX [46]). Therefore high values of F can be expected and it seems rewarding to place resonant cavities into one of the two bores at a later stage after the helioscope data taking phase. The RADES haloscope will only require the operation of the BabyIAXO magnet which encloses the two bores and will otherwise be an independent experiment. This enables a second detection strategy for the IAXO collaboration with a completely different target parameter space, since haloscopes typically reach higher sensitivities at a more limited mass range, as can be seen in Figure 2.2. The projected sensitivity limit of the RADES haloscope is well capable of covering QCD axion model space. In addition, the estimated costs of the haloscope are reduced due to the shared magnet and infrastructure of BabyIAXO.

This work focuses on reducing T_{sys} of equation (3.1) as this requires the use of cryogenics and the design of a unique cryostat, fitted for the requirements of BabyIAXO. As follows, the goal of the cryostat is the cooling of the cavities and the LNA to T_{sys} as low as possible while preserving large cavity volumes. A short introduction to the application of cryogenics is given in the following Section 3.3 and Chapter 4 describes the requirements of the cryostat and the resulting design choices.

3.3 Cryogenic application

The field of cryogenics includes the production of low temperatures and the study of physical phenomena and properties at low temperature. It differs from classical refrigeration by the level of temperature $T \leq 120\,\mathrm{K}$ [56]. This region seems especially compelling as many intriguing physical phenomena occur within it. Some of these phenomena are the magnetic ordering, the radical property changes, the solid-state transformation and the quantum effects including superconductivity and superfluidity [56]. The application of cryogenic technology is widely spread and only some examples are given here. Cryogenics is applied in the storage and transport of gases due to the densification at low temperature and the separation of gases based on adsorption. Cooling down of biological material helps in the area of preservation and medicine. Additionally, cryogenics is useful for electrical sensors as the low temperature reduces the thermal noise [56]. Lastly, the utilization of superconductivity in magnet technology is essential. Superconducting magnets conduct direct current (DC) with no resistance, which allows for the generation of high magnetic fields with acceptable electrical power consumption [57].

CERN has vast expertise in the area of cryogenics and operates multiple large-scale cryogenics projects, with the LHC being the largest cryogenic system in the world [58]. The LHC has a circumference of 27 km and consists of 1231 superconducting NbTi magnets, which need to be cooled down to 1.9 K [58].

The cooling of the BabyIAXO magnet [59, 60] is currently planned to be achieved by seven cryocoolers (four pulse tube two-stage and three Gifford-McMahon (GM) cryocoolers) [6, 61]. During cool down a remote helium gas circuit transports the heat from the magnet and the thermal shield to the cryocoolers. The final steady state, however, is achieved by conduction cooling via thermal links. At steady state heat loads of 1250 W at 50 K and 8.5 W at 4.5 K in the BabyIAXO magnet system are estimated [61].

4 Requirements and basic layout of the cryostat

This chapter focuses on the experimental requirements from BabyIAXO and RADES in Section 4.1, and the resulting design choices of the cryostat. For that the ongoing study of the resonant cavities to be applied in the BabyIAXO magnet from RADES is outlined in Section 4.2. Section 4.3 presents the basic standard cryostat layout and multiple considered cooling mechanisms for the present cryostat. Following this, Section 4.4 describes the most promising cooling mechanism as the topic of current research from the CCCL in greater detail. Finally, in Section 4.5 the preliminary design of the cryostat is presented. All following discussions of heat load estimation and thermodynamic model of the cooling system are based on this preliminary design.

4.1 Experimental requirements

First and foremost, it needs to be noted that the design of the BabyIAXO helioscope itself is still evolving. Furthermore, the R&D from RADES concerning the resonant cavities and the operation of haloscopes is an ongoing process. Therefore the experimental requirements described hereafter are merely assumptions resulting from the current state of BabyIAXO and RADES R&D. As the proposed layout of the cryostat is based on these assumptions it is crucial to iterate the requirements and adjust the design accordingly before actually progressing with the commissioning in the future. These circumstances lead to the first requirement of the design, which is to aim for high flexibility and easy adaptability. This is especially important for the geometry of the resonant cavities and their tuning mechanism as their design is currently not finalized. The experimental requirements below emerged in discussions with experts from both the BabyIAXO and the RADES project, respectively.

First, the limits given by the location and the BabyIAXO helioscope are presented. BabyIAXO will be located inside the HERA South Hall at DESY and, at the point of interest, stationary in its parking position. The geometry of the hall with BabyIAXO in its parking position is sketched in Figure 4.1. Each bore of BabyIAXO has a diameter of 70 cm and a length of 11 m. The length of the magnetic coil corresponds to 10 m. The bores will be warm bores, which means that they are not actively cooled and the conservative case of room temperature has to be assumed. However, the bores are exposed to the magnet thermal screen at 60 K. Unfortunately, there will not be any liquid helium cryogenic infrastructure available at the location, making a dry cryostat inevitable. Dry cryostats are closed-circuit cryostats where the cooling fluid is circulated inside a closed loop. The materials

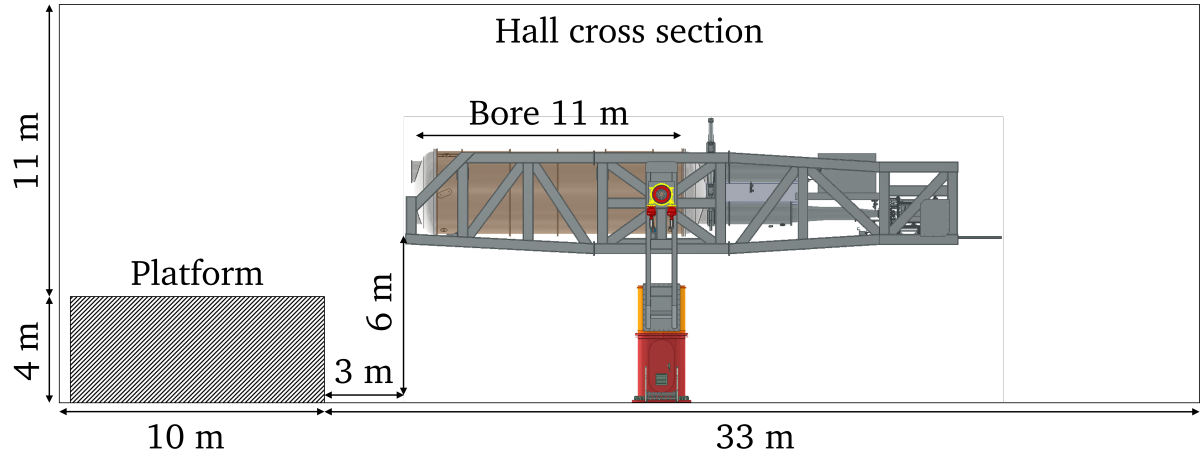

Figure 4.1: *Cross section of the intended hall at DESY with BabyIAXO depicted inside. CAD drawing of BabyIAXO courtesy of Frank Marutzky.*

need to be tolerant to the external magnetic field of 2.5 T and 3.2 T at the peak, respectively. Thus, auxiliary equipment that cannot be operated inside an external magnetic field needs to be located at an additional distance of 2 m from the end of the bore. At this distance the exposure is reduced to a stray magnetic field of less than 25 mT [62]. The whole cryostat needs to be insertable and removable into the bore without damaging its surface. Currently it is planned to insert the cryostat from the front (left side in Figure 4.1) so that the other side can be closed off with a vacuum valve and the helioscope detectors do not need to be dismounted. Additionally, it is assumed that the cryostat can be fully supported by scaffolding, which is needed since the weight distribution of BabyIAXO is precisely optimized to avoid torques during turning.

In the following paragraphs the requirements from the axion haloscope experiment are discussed. The vibrations occurring during operation of the cryostat should be minimized thus preserving the high sensitivity of the measuring devices. Furthermore, it is advantageous to reduce the temperature gradient along the cavity and keep it below 1 K difference. As hinted before the cryostat should be as independent from the cavity design as possible to allow for testing of new designs in the future. This includes the tuning mechanism which could include the opening of the cavity to adjust the resonant frequency. At the moment it is yet to be determined how many cavities will be inserted at the same time; many small cavities or one big cavity are both viable. In this work three cavities are assumed as a probable case.

For the operation of the haloscope the following auxiliary devices are needed. A single vector network analyzer (VNA) and a data acquisition (DAQ) system form the basis of the data taking and both devices will be located at room temperature. Coaxial cables conduct the radio frequency (RF) signal from the cavity at low temperature to the outside. Two coaxial cables are connected to each cavity at two ports, respectively; the so called critically and weakly coupled port. The RF signal from the cavity

must be amplified by an LNA to be read out and the LNA requires characterization by an electrical calibration load. The calibration scheme includes the heating of the load from the temperature of the LNA to an elevated temperature. As the temperature of the LNA contributes to the T_{sys} of equation (3.1), it is desirable to cool the LNA to the same temperature as the cavities. It is planned to deploy one amplifier per cavity and a single calibration load for all of them. Additional switches are required to change between the LNA characterization and the signal from the cavity. The RF signal from the critically coupled port contains the possible axion signal, which is why the attenuation in the coaxial cable between the critically coupled port and the amplifier should be minimized. This includes reducing the length of the coaxial cable and the number of SMA connectors. Finally a mix of electrical motors at room temperature and piezoelectric motors at low temperature will provide the tuning. The amplifier and the switch cannot tolerate any external magnetic field. The electrical layout of the system including the devices is displayed in Figure H in the appendix.

4.2 Resonant cavity studies

In order to give a basic understanding of the resonant cavity geometries the ongoing work by the RADES research group from Universidad Politécnica de Cartagena is outlined. Different cavity and tuning designs with the resonant frequency of about 0.5 GHz and a maximum diameter of 60 cm to be applied in BabyIAXO are studied. The aim is to maximize the volume and the quality factor of the cavities, while keeping the geometrical form factor as large as possible. Through simulations in CST Studio Suite [63] the shape of rectangular cavities with rounded edges was found as most versatile. The tuning could be done by the turning of metallic plates inside the cavity or by opening up the cavity into two half shells. There, the least amount of resulting misalignment in electric field is preferred. Higher resonance frequencies at large cavity volumes seem accessible by placing multiple plates in one cavity, called multi-cavity concept. All of the above mentioned concepts are depicted in Figure 4.2.

4.3 Basic layout and cooling options

The following section aims to help the reader understand the decision for the chosen cooling method as the most convincing solution for the requirements and restrictions outlined above. First, the basic layout of the cryostat, based on experience, is described. Afterwards different cooling method options are examined by outlining their biggest advantages and drawbacks.

As is standard practice in cryogenics the cryostat will be in vacuum and consist of multiple vessels and shields at different temperature levels. Inside the cryostat lie the resonant cavities or cold mass (CM) at the lowest temperature of about $4-10\,\text{K}$. In the middle at an intermediate temperature of about $35-55\,\text{K}$ lies the thermal shield (TS). The CM and the TS are both covered by multilayer

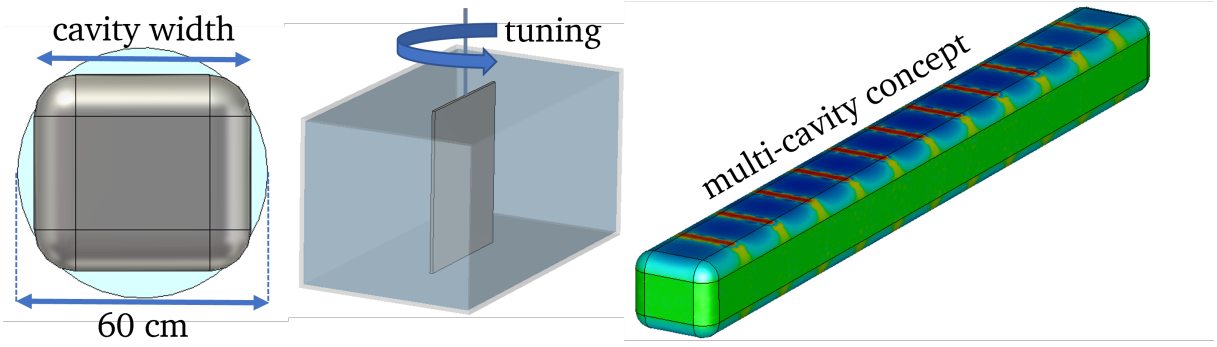

Figure 4.2: *Overview of the cavity design study for BabyIAXO. The picture includes the cavity profile with rounded edges (left), the possible tuning mechanism via metallic plates (middle) and the multi cavity concept (right), where a large cavity volume at higher resonance frequencies is preserved with the help of multiple plates inside one cavity. Images courtesy of P. Navarro (Department of Information and Communication Technologies, Universidad Politécnica de Cartagena).*

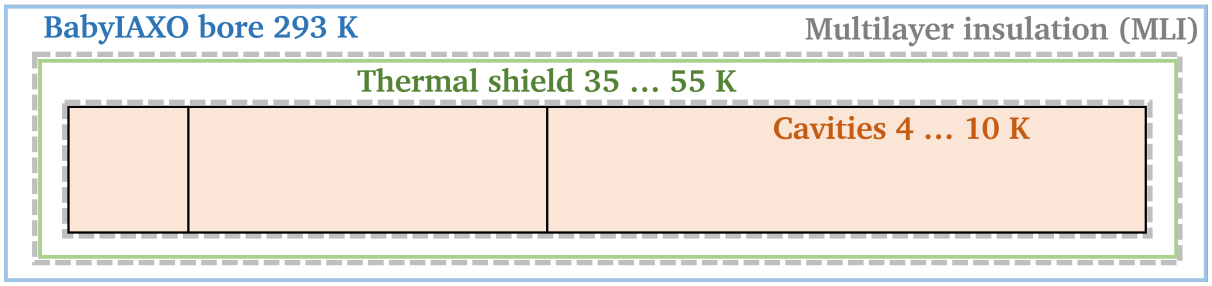

Figure 4.3: *Sketch of the basic layout of the cryostat and its different temperature levels. Here three cavities are assumed.*

insulation (MLI). On the outside is the vacuum vessel, here the BabyIAXO bore, at the highest temperature. Since the BabyIAXO bore is not actively cooled, the maximum temperature of about 293 K (room temperature) has to be assumed to be conservative. A sketch of the basic layout is presented in Figure 4.3. The cryostat for the axion haloscope in BabyIAXO has to be a dry cryostat, as explained in Section 4.1. This practically leads to the utilization of a cryocooler to extract the heat from the system. Cryocoolers are widely utilized and work by cycling helium in a closed loop. The helium absorbs heat at the cold head at a low temperature and transports the heat to room temperature. More information on the sophisticated working principles and the vast amount of different options can for example be found in [64, 65]. The different cooling options then differ in the answer to the question how to transport the heat from the CM, TS, and auxiliary devices to the cryocooler:

- The first possible option is the cooling via purely solid heat conduction. In that case the heat would be conducted in a solid thermal connector, which works passively without any cooling fluid and makes safety equipment redundant. However, substantial temperature gradients are

expected due to the long distances. The design of the cavities would always need to accommodate for the cooling method and its occupied space would restrict the thickness, material and shape of the cavities, as well as the tuning mechanism.

- The second cooling method consists of the convection of helium gas inside a leak-tight cavity. Helium does not affect the experimental sensitivity and the temperature could be precisely controlled. The drawbacks include the difficulty of creating an evenly distributed flow of helium inside the cavity, the complexity of the system for multiple cavities, the excluding of the tuning via opening of the cavity, and the immense effort of creating a tunable leak-tight cavity.
- The third possibility is to cool the cavities inside a helium liquid/gas bath. This would give the biggest flexibility for the cavity design because they could simply be submerged in the cooling fluid. Furthermore, it offers a simple temperature control and a large thermal stability. Though, less space would be available for the cavities, as an additional pressure vessel and additional safety equipment would be required, resulting in a highly complex system. Also, this solution would be very expensive due to the lack of the cryogenic infrastructure.
- The last cooling method discussed here is the remote cooling via cooling pipes around the cavities. There helium gas inside cooling pipes would transport the heat to the cryocooler. This would require some effort to create the thermal contact to the cavities and an effective heat exchanger to boost the cooling performance of the cryocooler. The small amount of helium gas inside the system allows for an easier handling compared to liquid helium and less stringent safety equipment. Furthermore, the available space in the BabyIAXO bore would be well exploited since only the TS and the cooling pipes must be mounted in between the cavities and the bore. Lastly, according to literature, remote cooling concepts reduce the exported vibrations from the cryocooler substantially [66].

Further advantages and drawbacks of the possible cooling method are listed in Table C.1 and Table C.2. It can be concluded from the short presentations of the different cooling methods, that the remote cooling method fulfills the above outlined requirements the best. Hence, the decision is made to develop a cryostat based on remote cooling via gas circulation inside cooling pipes. The following Section 4.4 introduces the remote cooling method in greater detail and presents current research on this topic by the CCCL.

4.4 Remote cooling method

The term remote cooling is applicable to every spatial and mechanical decoupling of the interface to be cooled from the cooling source. This includes flexible conductive straps connected to the cold head of a cryocooler [67, 68], sorption coolers [69], fluid circulation loops with and without the utilization of the Joule-Thomson cooling effect [66, 70, 71], and complex zero-boil-off cryostat arrangements [72]. The application of remote cooling allows, inter alia, to deliver cooling power to

installations which operate in harsh environments in non-easily reachable locations [73], and reduce the exported vibrations [66]. In the present work the focus lies on remote cooling methods based on a cryocooler and an independent active circulation loop. Such solutions offer a remote, dry, and minimized disturbance cooling. Furthermore, they are convincing as a compact and inherently flexible option [10]. Since the amount of cooling fluid required is low, the cost is reduced and the safety concerns compared to zero-boil-off cryostats are less serious, resulting in a less complex system [9]. These remote cooling methods seem attractive for many ultra-sensitive instruments requiring low temperatures like superconducting RF cavities in particle accelerators [68], superconducting quantum interference devices [73, 74], and cryogenic mirrors in gravitational-wave detectors [75]. Additionally, they appear to be the most compelling solution for the cooling of the resonant cavities of the BabyIAXO haloscope in the present cryostat.

The CCCL is doing extensive R&D on remote cooling methods based on a cryocooler and an independent active circulation loop. Their focus lies on the development of effective mesh-based counter-flow heat exchangers, as they and the cryocooler form the backbone of the cooling performance [10]. In the works of Onufrena et al. the design and a numerical study of such CFHX is presented [10] and the results are then reviewed by the discussion of the corresponding experimental data [76]. How to characterize the mesh placed in the CFHX is described in [77] and the application of remote cooling of superconducting RF cavities via capillary cooling pipes is analyzed in [9]. Due to their convincing findings it is planned to use a CFHX from the CCCL in the present cryostat.

4.5 Preliminary design of the cryostat

After discussing the requirements for the cryostat, the resonant cavity design, and the remote cooling method, the preliminary design of the cryostat can be presented. A complete sketch of the preliminary design is depicted in Figure 4.4. The cryostat is divided into three components: bore, transfer line, and service box. The bore of BabyIAXO contains the resonant cavities and the TS, which are both covered by MLI and are cooled via cooling pipes. A maximum outer diameter of the resonant cavities of 60 cm is estimated to reserve space for the support structure. Additionally the cavities are connected to coaxial cables and the tuning mechanism. The TS is made out of copper and the cavities are produced out of either stainless steel (SST) coated on both sides with copper or purely out of copper. Both structures might be required to be sectioned into multiple parts to avoid deformation during a quench of the BabyIAXO magnet (more details in Chapter 8). The 2 m long transfer line is attached to the flange at the end of the bore and the service box, respectively. It allows the operation of the auxiliary devices outside the BabyIAXO magnetic field. The TS, the coaxial cables, the cooling pipes, and the tuning mechanism are routed through the transfer line. Finally, the service box hosts all the auxiliary equipment for the operation of the axion haloscope and the remote cooling circuit. The auxiliary equipment is placed into an additional vacuum chamber (VC) called instrumentation vacuum chamber (IVC). The IVC allows to have two independent vacuum environments and, thus, accelerates

the purging and pumping process if maintenance of the electrical instrumentation is needed. The IVC is made out of G10 with a copper plate at the end for the thermal connection between the equipment and the cooling pipes. The service box also contains a TS which is assumed to be cooled completely via thermal links connected to the first stage of the cryocooler. In addition to the cryocooler and the CFHX a cryogenic circulator is needed to move the gas inside the pipes and overcome the resulting pressure drop. The components of the system are connected via small pipes, which are semi-flexible to achieve mechanical decoupling and reduce vibrations. For the cryocooler, a Cryomech® PT420 two-stage pulse tube cryocooler [78] is chosen because pulse tube cryocoolers are more reliable and introduce fewer vibrations than other cryocooler options. Furthermore, the Cryomech® PT420 cryocooler offers the highest cooling capacity available, next to the Cryomech® PT425 cryocooler, which is not yet well-studied as the present work is conducted. The Stirling Cryogenics® Cierzo cryogenic circulator [79] provides the highest efficiency at the envisioned volume flow range but might not overcome the emerging pressure head. Thus, the next size cryogenic circulator Stirling Cryogenics® Noordenwind [79] may be operated in a low efficiency regime depending on the system layout.

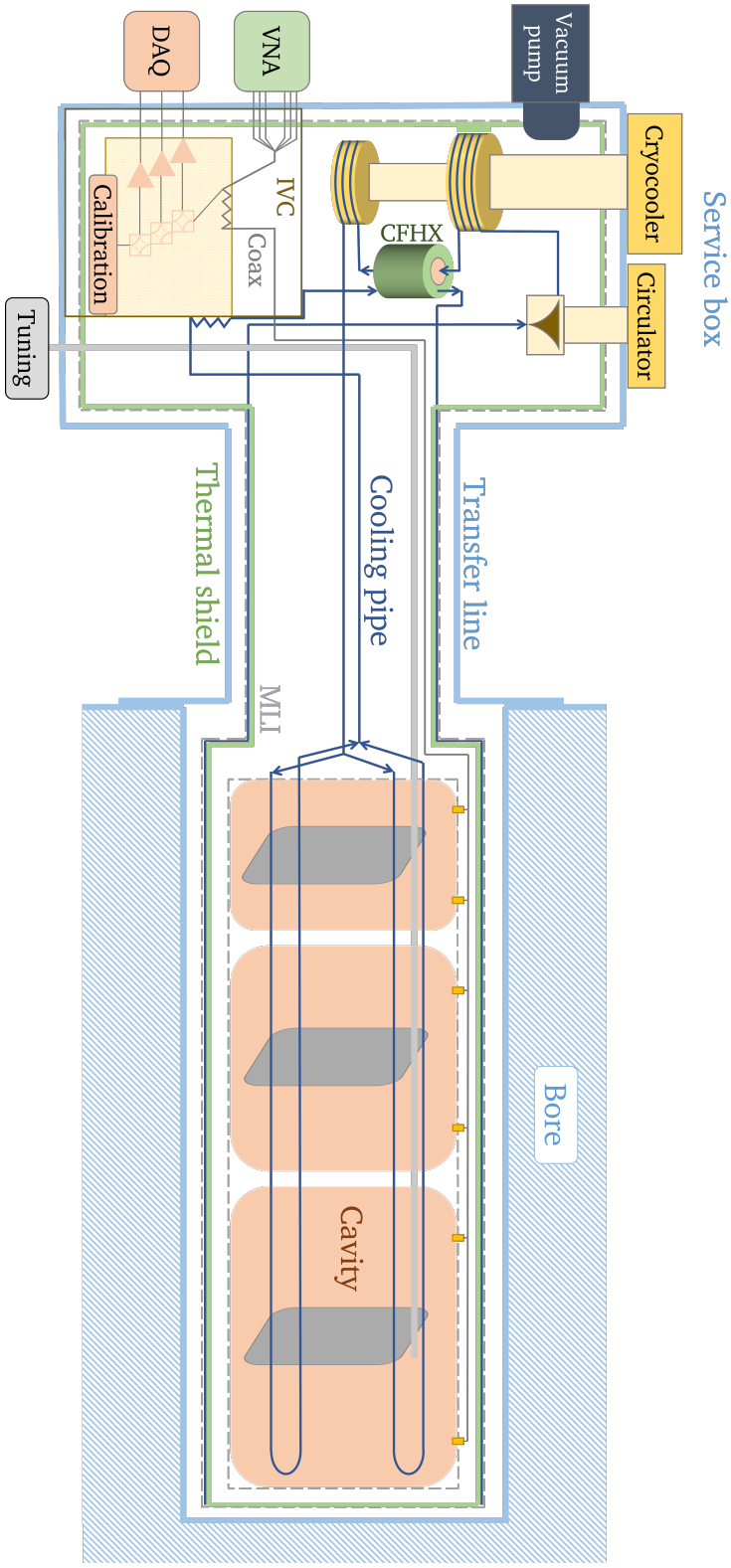

Figure 4.4: *Sketch of the preliminary system layout including the electrical system components, cooling system components, and the way of connecting those components with the cooling pipes. Three cavities are assumed.*

5 Heat load evaluation

This chapter presents the estimation of the heat load of the system. The heat load corresponds to the amount of energy the cooling system must extract. It is of paramount importance to minimize this heat load to reach low temperatures with the envisaged cryocooler based system and to save costs. The following values are merely estimations and need to be updated as the design of the resonant cavity system progresses. In Section 5.1 the fundamental heat transfer mechanisms are outlined. They form the basis to understand the different heat loads and the special cryogenic insulation methods. Afterwards, in Section 5.2 and Section 5.3 the substantial heat loads through the multilayer insulation and the coaxial cables are discussed. A numerical model for the heat transfer of the coaxial cables is given to increase the accuracy of the heat load estimation. Section 5.4 concerns the other smaller heat loads and Section 5.5 gives a summary of all heat load values and locations in the present system.

5.1 General heat transfer mechanisms in vacuum

5.1.1 Solid heat conduction

The first important heat transfer mechanism is the heat conduction through a solid connection with a temperature gradient, e.g. support structures, instrumentation wires, coaxial cables, and pressure pick-up lines. This mechanism usually contributes substantially to the overall heat leak. The heat transfer can be calculated by the application of Fourier's law for heat conduction [80]

$$\dot{\boldsymbol{q}}_{\mathrm{cond}} = -\lambda \boldsymbol{\nabla} T \ , \tag{5.1}$$

where $\dot{\boldsymbol{q}}_{\mathrm{cond}}$ is the area-specific heat flux vector in $\mathrm{W/m^2}$, $\boldsymbol{\nabla} T$ is the temperature gradient in K/m and λ denotes the material, temperature, and direction dependent thermal conductivity coefficient in $\mathrm{W/(m\,K)}$. For isotropic materials and the typical situation of a one-dimensional temperature gradient and uniform cross section, we can integrate (5.1) to obtain the heat flow $\dot{Q}_{\mathrm{cond}}$ in W in a solid element between the cold point 1 and the warm point 2

$$\dot{Q}_{\mathrm{cond}} = \frac{A}{l} \int_{T_1}^{T_2} \lambda(T)\,\mathrm{d}T \ , \tag{5.2}$$

where A denotes the cross-sectional area in m^2 and l the length of the element in m [81]. At low temperatures the thermal conductivity coefficient generally depends strongly on temperature, which is why its variation cannot be neglected. However, tabulated thermal conductivity integrals exist for many materials [81]. The thermal conductivity for solid materials spans over more than five orders of magnitude, making the careful selection of materials an elementary and essential step in the cryostat design process [81].

5.1.2 Residual gas conduction

The second important heat transfer mechanism is the heat transport through any residual gas remaining inside the vacuum vessel. Two very different regimes, depending on the mean free path Λ_l and the distance l between the two transfer surfaces, have to be considered. If $\Lambda_l \ll l$ holds, the collisions between gas molecules dominate the heat transfer and the hydrodynamic regime applies [81]. For $\Lambda_l \gg l$ the gas molecules travel from wall to wall without colliding with other molecules and the molecular regime applies [56].

In the hydrodynamic regime at pressures about $1-1000$ Pa the thermal conductivity of a gas is nearly independent of pressure and the heat flux is inversely proportional to l, analogous to solid heat conduction [56, 82]. The heat flux can be described as in (5.1) with an adapted gas thermal conductivity coefficient [81].

The molecular regime typically dominates at pressures $p < 0.1$ Pa and heat conduction depends on the transport of single gas molecules [82]. The heat conduction varies linearly with the number of molecules and therefore with pressure [81] but does not depend on l [83]. The modeling of heat transfer stems from kinetic gas theory and is given here without derivation. According to Van Sciver [56] the heat flux $\dot{q}_{\mathrm{gas}}$ in W/m^2 between two parallel surfaces in the molecular regime is given by the relationship

$$\dot{q}_{\mathrm{gas}} = \frac{\alpha_0}{4}\frac{\gamma+1}{\gamma-1}\left(\frac{2R_{\mathrm{gas}}}{\pi\widetilde{M}T}\right)^{0.5} p\,(T_1-T_2)\,\frac{\mathrm{W\,s^3}}{\mathrm{m^2\,K}}\,, \tag{5.3}$$

where γ is the heat capacity ratio ($\gamma = 5/3$ for helium), R_{gas} is the gas constant in J/(mol K), $\widetilde{M}$ the molecular weight of the gas in kg/mol, p denotes the pressure in Pa, and T the arithmetic mean of the two surface temperatures T_1 and T_2 in K. $\alpha(T)$ is an accommodation coefficient that accounts for molecules leaving a surface with an energy different than the surface temperature and is a function of the molecule, the temperature, and the geometry [56]. For simple geometries like parallel or concentric walls the averaged accommodation coefficient α_0 is given by

$$\alpha_0 = \frac{\alpha_1\alpha_2}{\alpha_2 + \frac{A_1}{A_2}(1-\alpha_2)\,\alpha_1}\,. \tag{5.4}$$

Here α_1, α_2, A_1, and A_2 are the respective accommodation coefficients and surfaces of the two walls. In this work the above equation is applied to calculate the heat transfer of the residual gas molecules between the layers of MLI (see Section 5.2.2).

5.1.3 Thermal radiation

The third heat transfer mechanism, thermal radiation, is by far the most important one in cryogenics as it is usually the cause of the largest heat leak into the system [83]. The Stefan-Boltzmann equation $\dot{q}_{\mathrm{rad}} = \sigma \varepsilon T^4$ describes the radiative heat flux $\dot{q}_{\mathrm{rad}}$ in $\mathrm{W/m^2}$ from a single surface. ε represents the emissivity of the surface at temperature T and $\sigma = 5.67 \times 10^{-8}\,\mathrm{W/(m^2\,K^4)}$ is the Stefan-Boltzmann constant. For more information on the emissivity coefficient and its dependency on temperature, wavelength, and surface condition, see the work of Ekin [81]. Since all surfaces emit radiation the net heat exchange has to be calculated to estimate the heat leak. The correlations for the net heat exchange depend on the surface properties of every surface involved and on geometrical view factors of the surfaces to each other. Of particular interest for cryostat design are the geometries of parallel plates and enclosed cylinders or spheres. The inner enclosed surface A_1 is typically colder than the outer surface A_2. The respective temperatures and emissivity coefficients are denoted with T_1, T_2, ε_1, and ε_2, respectively. With these variables it is then possible to calculate an effective emissivity coefficient E. According to Ekin [81], for specular reflection ($\varepsilon \ll 1$) for long coaxial cylinders or concentric spheres, E reads

$$E = \frac{1}{\frac{1}{\varepsilon_1} + \frac{A_1}{A_2}\left(\frac{1}{\varepsilon_2} - 1\right)} \,. \tag{5.5}$$

Using the effective emissivity coefficient and multiplying the heat flux with the enclosed surface A_1 the radiative heat flow $\dot{Q}_{\mathrm{rad}}$ analogous to the Stefan-Boltzmann equation can be calculated by

$$\dot{Q}_{\mathrm{rad}} = \sigma E A_1 \left(T_2^4 - T_1^4\right) \,. \tag{5.6}$$

It seems natural to place floating (not thermally anchored) reflective layers between the surfaces to break the temperature gradients into smaller pieces, due to the great temperature differences in cryogenics to the ambient temperature and the strong temperature dependency to the fourth power in (5.6). Introducing one intermediate layer in a cryostat reduces the heat leak to the cold surface by half [81]. If this layer is actively cooled, the effectiveness of the cooling system can be improved further, due to the lower emissivity at lower temperatures and the lower Carnot cooling cost at this increased temperature [83]. The cooling cost or the required cooling work at different temperatures can be compared via the coefficient of performance (COP). The COP is the ratio of the useful cooling power at low temperature to the work required at high temperature and is proportional to the efficiency of an ideal Carnot cycle, $T_{\mathrm{cold}}/(T_{\mathrm{hot}} - T_{\mathrm{cold}})$ [56]. From the Carnot efficiency it can be deduced that increasingly more energy is required to remove heat at lower temperatures, hence motivating the extraction of heat at a higher intermediate temperature. However, it needs to be noted that the Carnot efficiency does not contain the numerous loss mechanisms of reality, and the temperature levels of the present system should be optimized for the actual efficiency of the cryocooler.

The installation and operation of thermal shields is common practice in cryogenics and the principle of floating reflective layers is exploited in multiple design techniques. One important example is

multilayer insulation, where multiple reflective layers are placed around the cold surface for insulation. The fundamentals and the modeling of multilayer insulation are explored in the following Section 5.2. For other radiation shield techniques see the examples in the works of Ekin [81] and Balshaw [57].

5.2 Multilayer insulation

5.2.1 Principles of multilayer insulation

Multilayer insulation (MLI) is widely used in cryogenic systems as it offers one of the most effective insulation performances in proper vacuum conditions, is generally easy to apply and is commercially available [81, 84, 85]. MLI consists of several reflective layers kept separated by a thermally insulating material, replicating the principle of multiple floating radiation shields. A popular MLI choice is aluminized mylar layers with low-density fibrous insulating spacers such as polyester nets stacked together as blankets of multiple layers. More information on the design and installation of MLI can be found in the work of Donabedian et al. [86].

According to Scott [87], deploying N floating reflective layers reduces the radiative heat transfer by a factor of about $1/(N+1)$. Unfortunately MLI systems face effects of reality which worsen this ideal correlation. The overall number of layers and the distance between the layers mainly determine the effectiveness of the MLI and are both roughly functions of the layer density [56]. If more layers are used, the radiative heat leak decreases but if the MLI is compressed too tightly, the solid conduction through the spacers increases. Studies on this topic reveal an optimal layer density of about 30 layers/cm [83, 88, 89]. Other important influences on the effectiveness are the layer quality, the residual gas between the layers, and the mounting process. MLI tends to be compressed by its own weight on the top of the cryostat and looser at the bottom [83]. Degradation points of the MLI arise at discontinuities in the surface, such as covers, flanges, suspensions and supports [90]. Furthermore, degradation occurs at places of poor accessibility, deflection, and mechanical load, as well as for uncontrolled wrapping technique [90]. More information can be found in the work of Lehmann [90], who studied the effects of these degradations.

Thermal radiation usually accounts for the biggest heat leak into the cryogenic system and MLI reduces this heat leak substantially [91]. Therefore great motivation exists to study the properties and influences of MLI. The literature, however, is quite heterogeneous and several values of performance are found for seemingly the same conditions [92, 93]. These findings suggest that the ideal MLI application is a delicate procedure where small variations lead to very different results [94]. Thermodynamic models could help predict the performance and therefore aid the dimensioning of the cryogenic system. These models can take various parameters into account, such as reflective layer material, spacer material, number of layers, layer density, contact pressure, maintained vacuum, and

interstitial pressure [95]. However, owing to the factors described earlier, these models can seldom depict reality and the experimental results are difficult to transfer [88].

At CERN a semi-empirical model developed by Riddone [96] is used with reasonable success [83]. The two main contributions of solid conduction and radiation are considered with each having a parameter fitted against experimental data from the LHC. These parameters then include all the inefficiencies resulting from the real implementation of MLI protection on the large-scale accelerator [83]. According to Riddone [96] and Parma [83] the heat flux through MLI $\dot{q}_{\mathrm{MLI}}$ in $\mathrm{W/m^2}$ between temperature T_2 and T_1 is calculated with

$$\dot{q}_{\mathrm{MLI}} = \frac{\beta_{\mathrm{cond}}}{N+1}\frac{T_1+T_2}{2}(T_2-T_1)+\frac{\beta_{\mathrm{rad}}}{N+1}\left(T_2^4-T_1^4\right)\,, \tag{5.7}$$

where N is the number of the MLI layers, and $\beta_{\mathrm{cond}} = 1.401\times10^{-4}\,\mathrm{W/(m^2\,K^2)}$ and $\beta_{\mathrm{rad}} = 3.741\times10^{-9}\,\mathrm{W/(m^2\,K^4)}$ are the corrective factors.

5.2.2 Multilayer insulation in the present setup

To decide for the materials and the number of layers of MLI and to estimate the heat leak through the MLI it would be preferable to refer to experimental data. However, that is not possible for a system not yet built. As explained above, it is difficult to choose a fitting MLI model or experimental value due to the substantial differences. In the literature the estimated values for similar experiments are often based on experience as in [97]. The following section explains the estimation path chosen in the present work. First, experimental data from the LHC is presented, which is used as a baseline for the present layout. Then, the MLI model with additional application factors from (5.7) is defined. Lastly, the surface area of the MLI is estimated.

CERN has considerable experience with the building and operation of large-scale cryostats. Hence, experimental values of the LHC MLI according to Parma [83] seem trustworthy. These values were gathered and averaged over the whole LHC and contain all the degradation points coming from large-scale industrial application. For a 30-layer MLI between 300 K and 50 K a heat flux of about $1\,\mathrm{W/m^2}$ and for a 10-layer MLI between 50 K and 1.9 K a heat flux of about $54\times10^{-3}\,\mathrm{W/m^2}$ was obtained [83]. The data is in a conservative temperature range compared to the expected temperatures for the TS (35 −55 K) and the CM (4 −10 K). Additionally, the present MLI layout has a similar cylindrical shape. Hence, it is decided to cover the TS in 30-layer and the CM in 10-layer MLI. The main purpose of the MLI blanket mounted on the CM is to drastically reduce the heat load from vacuum degradation due to leaks or accidental air venting, as the heat leak from radiation is relatively small in the low temperature range [83]. Parma [83] links a nominal residual gas pressure of $p < 1\times10^{-6}\,\mathrm{mbar}$ to the experimental values. In the present setup, pressures of $1\times10^{-5}\,\mathrm{mbar}$ at warm and $1\times10^{-6}\,\mathrm{mbar}$ at cold are expected. It has to be noted that, in order to reach these pressure regimes, a vacuum pumping of three weeks before operation seems necessary due to the outgassing of the great surface area of the MLI.

The fixed heat load values from Parma [83] cannot describe the present system sufficiently. The MLI, the temperature levels, and the heat load values for the LHC stem from optimizations for the application in the LHC and the operation of cryoplants [83]. In the present setup, however, the cooling is provided by cryocoolers which operate at their own cooling effectiveness. Therefore, the optimum temperature levels for the specific present application are to be found, as shown in the following chapters. For that, it is beneficial to describe the heat leak through the MLI as a function of the shield temperature by applying the above described MLI model of (5.7) from Riddone [96]. The expected CM temperatures higher than 1.9 K lead to a higher residual gas pressure between the MLI layers compared to the LHC. Hence, according to Riddone [96], the contribution of the residual gas conduction of equation (5.3) is added to the model (5.7) as a third mechanism. The accommodation coefficient in (5.3) is approximated with $\alpha_0 = 0.5$ [81, 82]. Thus, the present MLI heat load is calculated as a sum of (5.7) and (5.3) with 30 layers on the TS, 10 layers on the CM, 1×10^{-6} mbar residual gas pressure, and variable temperatures. Additional application factors to be multiplied with the calculations are defined to ensure the operability of the cryostat as the present design is expected to have more degradation points than the LHC cryostat. The installation of the MLI on the CM is impeded by the discontiguous cavities and the feedthroughs of the cooling pipes, the support structure, the tuning mechanism, and the coaxial cables (see Figure 4.4). The installation process on the TS seems less complicated due to fewer degradation points from cooling pipes and support structure. Neumann et al. [98] experimentally investigated MLI performance for complex surface geometries with multiple degradation points. Based on this work an application factor of 1.2 for the MLI of the TS and 2 for the MLI of the CM is defined. The resulting specific heat load on the TS at 50 K corresponds to $1.333\,\mathrm{W/m^2}$ and the heat load on the CM at 4.5 K to $67.5 \times 10^{-3}\,\mathrm{W/m^2}$.

As the overall heat leak through the MLI depends on the surface area of the TS and the CM covered by MLI, these surfaces need to be estimated. The outer surface of the cavities is estimated with the shape of a cylinder with diameter of 60 cm and considering the influences of end caps, the feedthroughs of cooling pipes, support structure, tuning mechanism, and coaxial cables which results in $A_{\mathrm{CM}} = 19.42\,\mathrm{m^2}$. The surface area of the TS is split into multiple components: bore, transfer line, and service box (see Section 4.5). The shape of the TS in the bore roughly corresponds to a cylinder and its surface area is calculated analogous to A_{CM} to $A_{\mathrm{TS,bore}} = 21.08\,\mathrm{m^2}$. The surface of the transfer line $A_{\mathrm{TS,trans}}$ is approximated by $0.94\,\mathrm{m^2}$ and, finally, the surface of the service box $A_{\mathrm{TS,serv}}$ is about $2.45\,\mathrm{m^2}$. The resulting heat leak through the MLI at 50 K and 4.5 K is listed in Table 5.2 in Section 5.5.

5.3 Thermal modeling of the coaxial cables

The following section presents the approach to estimate the heat leak through the coaxial cables via a thermal model. First, typical coaxial cables are described and motivation is given, why they are a relevant candidate for more extensive modeling. Then the thermal model for the temperature

distribution inside two exemplary coaxial cables is outlined. Lastly, the results are discussed and the layout of the coaxial cables in the present system is proposed.

Coaxial cables refer to cylindrical electric cables consisting of an inner and an outer conductor, separated by a dielectric insulator. The signal's electric and magnetic field is contained in the dielectric between the inner and outer conductor. The outer conductor acts as shield, which reduces the interference between the electric and magnetic fields of the signal and the environment, resulting in less noise in the signal and less leakage into adjacent circuits of the signal. For high frequencies and sensitive measurements coaxial cables must be utilized [99], with the present setup falling into this category.

The following investigation of the coaxial cables is motivated by the expected substantial heat leak through them. Coaxial cables often pose a problem in cryogenics due to their relatively big physical size and the difficulty in heat sinking the cables [99]. The dielectric insulator often consists of Polytetrafluoroethylene (PTFE), which provides an excellent thermal insulation of the inner conductor due to its low thermal conductivity. Depending on the cable and the application, the cable might be thermalized by gently clamping it between two copper plates or it may be required to break the coaxial cable open and solder in a short section of metal foil, which is insulated from ground by a thin dielectric [99]. More unique thermalization techniques can be found in literature [81, 99].

The selection of the conductor material and the physical size of the coaxial cable is a compromise between minimizing the RF attenuation and the heat leak [81, 99]. The lowest heat leak is typically achieved with coaxial cables made of stainless steel, though they also possess high signal attenuation. Contrarily, coaxial cables made of copper have better electrical properties but a high thermal heat leak [81]. The final cable selection depends on the system and, next to attenuation and heat leak, also includes the factors of characteristic impedance, thermal contraction, and vacuum integrity [99]. Here, only two coaxial cables out of the numerous possibilities are discussed: QAXIAL® RG402-CU semi-rigid coaxial cable [100] and KEYCOM® ULT-05 semi-rigid coaxial cable [101]. The two chosen coaxial cables aim to represent the groups of copper and stainless steel based cables. Further, they seem to fit to the present system and have both been used at the CCCL. The QAXIAL® RG402-CU semi-rigid coaxial cable [100] consists predominately of copper and is henceforth named copper coaxial cable. Analogously, the KEYCOM® ULT-05 semi-rigid coaxial cable [101] is henceforth named SST coaxial cable. Unfortunately, insufficient data is available to compare the attenuation of the cables accurately. Thus, the RF attenuation per cable length at room temperature of 0.92 dB/m (at 0.5 GHz, scaled from data at 10 GHz) for the SST coaxial cable [101] and 0.27 dB/m (at 0.5 GHz) for the copper coaxial cable [100] from the manufacturers is assumed. The material and the diameter of the different layers in the respective cables are specified in the appendix in Table G.6. Figure 5.1 depicts the cross section of the cables, showing the layers of copper and SST cable as assumed for the model.

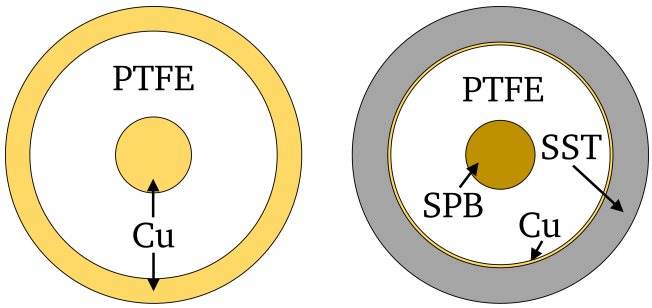

Figure 5.1: *Simplified sketch of the cross section of the QAXIAL® RG402-CU [100] (left) and the KEYCOM® ULT-05 [101] (right) semi-rigid coaxial cable with the respective layers. The proportions are merely approximate and the exact dimensions can be found in the appendix and the respective references. PTFE = Polytetrafluoroethylene, Cu = copper, SPB = silver plated brass, SST = stainless steel.*

5.3.1 Description of the modeling

For the present setup the coaxial cables are assumed to stretch from room temperature to low temperature while being thermalized at the TS via clamps at an intermediate temperature. A 2D model is developed to estimate the temperature distribution of the coaxial cables in equilibrium and the deposited heat loads. Here, the radial heat transfer has a substantial influence on the temperature distribution, due to the different thermal conductivity values and the thermalization only at the outer layer. The layers inside the cables possess central symmetry, which is why a 2D model seems sufficient and central symmetry in the temperature distribution is assumed. The model consists of volume elements which interact via the basic heat transfer equations. Each layer is modeled by a single element, resulting in three and four radial nodes, respectively. The number of longitudinal volume elements depends on the chosen resolution N. The different layers are modeled analogous to the sketch of Figure 5.1. There, the thermal conductivity coefficients of copper (OFHC, RRR = 100), stainless steel 304, and PTFE according to the National Institute of Standards and Technology (NIST) [102], the thermal conductivity coefficient of silver (RRR = 30) according to Cryocomp [103], and the thermal conductivity coefficient of brass according to Lake Shore Cryotronics® [104] are used. Silver plated copper is estimated by pure copper and silver plated brass (SPB) is modeled with a mean thermal conductivity of pure silver and brass weighed with the respective cross section. Note that assuming bulk PTFE properties for the foamed PTFE dielectric of the SST coaxial cable is a strong assumption. However, the thermal conductivity of foamed material can vary depending on the application since it involves solid conduction and conduction in the residual gas [56], making it too complex to represent accurately.

Isothermal conditions and steady state inside each volume element are assumed thus linearizing the heat transfer equations. This seems justified for high resolutions and is verified by checking if the results vary depending on the resolution. The longitudinal and radial heat transfer is based on Fourier's law of heat conduction. Additionally, thermal boundary resistances are added to describe

the heat transfer between the different materials [105]. Each volume element i can be exposed to up to four heat flows in W from the preceding element of the same layer $\dot{Q}_{i-1,i}$, the following element of the same layer $\dot{Q}_{i,i+1}$, from the inner layer $\dot{Q}_{i,\mathrm{il}}$, and the outer layer $\dot{Q}_{i,\mathrm{ol}}$. In equilibrium this leads to $\dot{Q}_{i-1,i} + \dot{Q}_{i,i+1} + \dot{Q}_{i,\mathrm{il}} + \dot{Q}_{i,\mathrm{ol}} = 0$. An illustration of the possible heat flows inside a single volume element i from its surrounding volume elements is depicted in Figure 5.2. The subscript i denotes the position along the length of the cable, *ol* is the outer layer, *pl* the present layer, and *il* the inner layer. The equations for the four different heat flows are given in the following. The notation of the

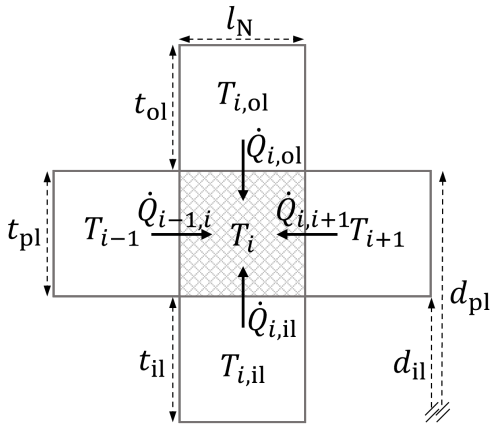

Figure 5.2: *Illustration of the possible heat transfer mechanisms of a single volume element inside the coaxial cable model. Each volume element has a constant temperature T. The subscript i denotes the position along the length of the cable, ol is the outer layer, pl the present layer, and il the inner layer. l_N describes the longitudinal length of one volume element, depending on N, t denotes the radial thickness of the layer, and d is the outer diameter of the layer in the cable.*

equations corresponds to Figure 5.2. $\dot{Q}_{i-1,i}$ is described by

$$\dot{Q}_{i-1,i} = A_\mathrm{cross} \frac{1}{l_\mathrm{N}} \frac{\lambda_{i-1} + \lambda_i}{2} \left(T_{i-1} - T_i\right) , \tag{5.8}$$

where A_cross denotes the total cross section of the present layer in m^2 and equals $A_\mathrm{cross} = \frac{\pi}{4}\left(d_\mathrm{pl}^2 - d_\mathrm{il}^2\right)$, with d_pl and d_il being the diameter in m of the present and the inner layer, respectively. l_N is the longitudinal length of one volume element in m, depending on N, and T in K and λ in $\mathrm{W/(m\,K)}$ are the temperature and the thermal conductivity of the respective element. The thermal conductivity is a function of the material and temperature. Analogously, $\dot{Q}_{i,i+1}$ can be calculated with

$$\dot{Q}_{i,i+1} = A_\mathrm{cross} \frac{1}{l_\mathrm{N}} \frac{\lambda_i + \lambda_{i+1}}{2} \left(T_{i+1} - T_i\right) . \tag{5.9}$$

The other two heat flows depict the radial heat transfer through two different materials. Thus, the effective heat transfer coefficient α_eff in $\mathrm{W/m^2}$ and the effective heat transfer area A_eff in m^2 consist of three components (bulk conduction and boundary conductance) added up as the sum of

thermal resistances connected in series [80]. The conduction perpendicular to the layers is calculated according to VDI Heat Atlas [80] for the heat conduction for hollow cylinders. This leads to the radial heat flow being estimated by

$$\begin{aligned}\dot{Q}_{i,\mathrm{il}} &= A_{\mathrm{eff}}\alpha_{\mathrm{eff}}\left(T_{i,\mathrm{il}} - T_i\right) \\ &= \left[\frac{\ln\left(\frac{d_{\mathrm{il}}}{d_{\mathrm{il}}-0.5t_{\mathrm{il}}}\right)}{2\pi l_{\mathrm{N}}\lambda_{i,\mathrm{il}}} + \frac{1}{\pi d_{\mathrm{il}} l_{\mathrm{N}}\Lambda_{\mathrm{il,pl}}} + \frac{\ln\left(\frac{d_{\mathrm{il}}+0.5t_{\mathrm{pl}}}{d_{\mathrm{il}}}\right)}{2\pi l_{\mathrm{N}}\lambda_i}\right]^{-1}\left(T_{i,\mathrm{il}} - T_i\right),\end{aligned} \tag{5.10}$$

and

$$\begin{aligned}\dot{Q}_{\mathrm{i,ol}} &= A_{\mathrm{eff}}\alpha_{\mathrm{eff}}\left(T_{i,\mathrm{ol}} - T_i\right) \\ &= \left[\frac{\ln\left(\frac{d_{\mathrm{pl}}}{d_{\mathrm{pl}}-0.5t_{\mathrm{pl}}}\right)}{2\pi l_{\mathrm{N}}\lambda_i} + \frac{1}{\pi d_{\mathrm{pl}} l_{\mathrm{N}}\Lambda_{\mathrm{pl,ol}}} + \frac{\ln\left(\frac{d_{\mathrm{pl}}+0.5t_{\mathrm{ol}}}{d_{\mathrm{pl}}}\right)}{2\pi l_{\mathrm{N}}\lambda_{i,\mathrm{ol}}}\right]^{-1}\left(T_{i,\mathrm{ol}} - T_i\right),\end{aligned} \tag{5.11}$$

where t is the thickness of the corresponding layer in m and Λ the thermal boundary conductance in $\mathrm{W/(m^2\,K)}$ between the respective layers. Here, Λ is a function of the joint pair of materials and its average temperature. The latter equals the arithmetic mean temperature of the two concerned elements. The correlations for the conductance are based on the work of Gmelin et al. [105]. A polynomial fit function of measured data from Gmelin et al. [105] is used for the contact between copper and copper (Cu/Cu), e.g. at the TS heat intercept for the Cu cable. A logarithmic interpolation between data from Berman [106] (Cu/PTFE/Cu) and Satter and Ashworth [107] (Cu/Nylon) describes the conductance between Cu/PTFE and SPB/PTFE. Lastly, the contact of SST and copper is estimated by a logarithmic interpolation between the conductance data from Salerno et al. [108] (SST/In/SST) and Michalski [105] (SST/Cu).

Applying the above detailed equations to every volume element leads to a system of linear equations. A schematic of heat transfer pathways for the copper coaxial cable model is shown in Figure 5.3. There, the subscript *Cuo* denotes the outer conductor copper layer, *PTFE* the dielectric PTFE layer, and *Cui* the inner conductor copper layer. Note that the volume elements representing the inner conductor are exposed to a maximum of three heat flows due to the symmetry of the cable. The Dirichlet boundary conditions of a fixed temperature, at room temperature, at low temperature, and at the TS heat intercept are highlighted by colored hatched regions. The SST coaxial cable model consists of four radial volume elements which are calculated analogously to the sketch in Figure 5.3.

It is possible to generate a matrix system of linear equations in the form of $\boldsymbol{A}\boldsymbol{x} = \boldsymbol{b}$. The coefficient matrix $\boldsymbol{A}$ consists of α_{eff} and A_{eff} from the above described equations. The temperatures of the volume elements constitute the solution vector $\boldsymbol{x}$. Lastly, all boundary conditions are collected inside the constant vector $\boldsymbol{b}$. Computing of the inverse of the coefficient matrix $\boldsymbol{A}^{-1}$ allows to resolve the system and the solution vector equals $\boldsymbol{x} = \boldsymbol{A}^{-1}\boldsymbol{b}$. Since the thermal conductivity coefficients and the thermal boundary conductances are a function of temperature, $\boldsymbol{A}$ and $\boldsymbol{b}$ depend on $\boldsymbol{x}$, which

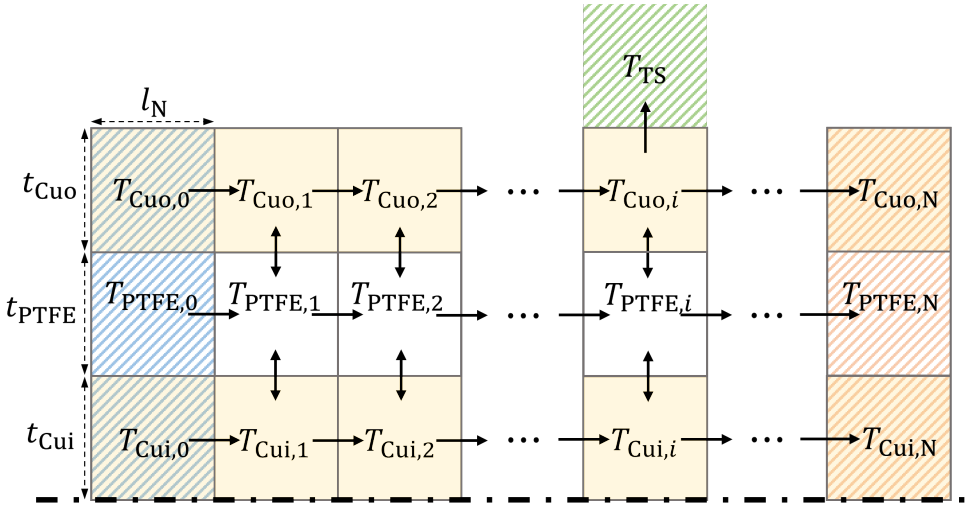

Figure 5.3: *Schematic of the 2D numeric model of the temperature distribution inside the copper coaxial cable. The longitudinal and radial heat transfer inside the cable and at the thermalization points are considered. The boundary conditions are highlighted by colored hatched regions.*

makes an iterative calculation necessary. The system is solved and updated until the changes in $\boldsymbol{x}$ are sufficiently small (relative change of the values $< 1 \times 10^{-5}$). Afterwards, the temperature of each volume element can be recovered from the solution, resulting in the temperature distribution of the coaxial cable in steady state. Additionally, the heat deposited at the TS and at the low temperature interface is calculated.

5.3.2 Findings of the coaxial cable model

The calculation results are based on the assumptions for the layout of the coaxial cables. The coaxial cables introduce their biggest heat leak inside the service box, where they penetrate the system from the outside at room temperature and get thermalized by being pressed in a meander to the thermalization plate of the IVC (see Figure H.10). The length of the coaxial cables between these two thermalization points is assumed to be 1 m. At an intermediate stage the cables get thermalized at the TS via flexible copper braids, which are clamped to the cables at a specific point. Room temperature is defined as 293 K, the TS temperature as 50 K, and the low temperature at the end of the cable as 4.5 K. The length of the intermediate intercept corresponds to 0.1 m and the center of the intercept point is located at 25 % of the total cable length for the copper cable and at 50 % for the SST cable, respectively. The heat intercept positions result from a preliminary study, where the heat loads at the intermediate and low temperature were weighed with the corresponding Carnot efficiency and the total weighed heat load was minimized. This is only valid as a first approximation by assuming that the Carnot efficiency ratio of the two temperature levels corresponds to the actual cryocooler efficiency ratio.

The temperature distribution of every layer inside the coaxial cable allows for detailed comparisons: The heat load at low temperature for one copper coaxial cable without an intermediate intercept at the TS corresponds to 0.710 W which is practically impossible to compensate with a cryocooler-based cooling system. The heat load at low temperature is reduced to 0.435 W by adding the heat intercept. In that case, the TS is exposed to an additional 1.20 W. Analogously, the heat load at low temperature for one SST coaxial cable without an intermediate heat intercept equals 0.027 W. In the setup with an intermediate intercept the heat load at low temperature corresponds to 0.007 W and at the TS to 0.09 W. Interestingly, the heat load at low temperature for the SST coaxial cable originates to 85 % from the 5 µm thin copper layer. The copper coaxial cable would induce the same amount of attenuation as the SST layout denoted above for a cable length of 3.41 m, which results in a heat load of 0.121 W at low temperature and 0.36 W at the TS. All heat loads at the two temperature levels of 50 K and 4.5 K from one coaxial cable in the discussed layouts are presented in Table 5.1. Table 5.1 also includes the approximated attenuation.

Table 5.1: *Summary of the heat load at* 50 K *and* 4.5 K *from one coaxial cable and the respective attenuation in different layouts. The heat loads are calculated with the thermal model for the copper and SST coaxial cables. The attenuation is approximated based on data provided by the manufacturer.*

Description	Heat load @50 K (W)	Heat load @4.5 K (W)	Attenuation* (dB)
Copper coaxial cable			
No TS heat intercept, length 1 m	-	0.710	0.27
TS heat intercept, length 1 m	1.22	0.433	0.27
TS heat intercept, length 3.41 m	0.36	0.121	0.92
SST coaxial cable			
No TS heat intercept, length 1 m	-	0.027	0.92
TS heat intercept, length 1 m	0.09	0.007	0.92

* merely a rough estimation, see text for more details.

Figure 5.4 shows the temperature distribution inside the Cu and SST coaxial cables, respectively, along their length. Additionally, the radial temperature difference between the inner most and outer most layer along the length is displayed. Note that apart from the peak in temperature difference at the TS heat intercept the radial temperature difference is small. However, this non-visible temperature difference is positive, which results in a radial heat transfer from the inside to the outside.

The manufacturer specified two experimental heat leaks through the SST coaxial cable [101], which allows to evaluate the model and its validity. For their setup a 0.1 m long cable was cooled at one end to 4 K and heated at the other end to 20 K and 100 K, respectively. For the first case of 20 K, this

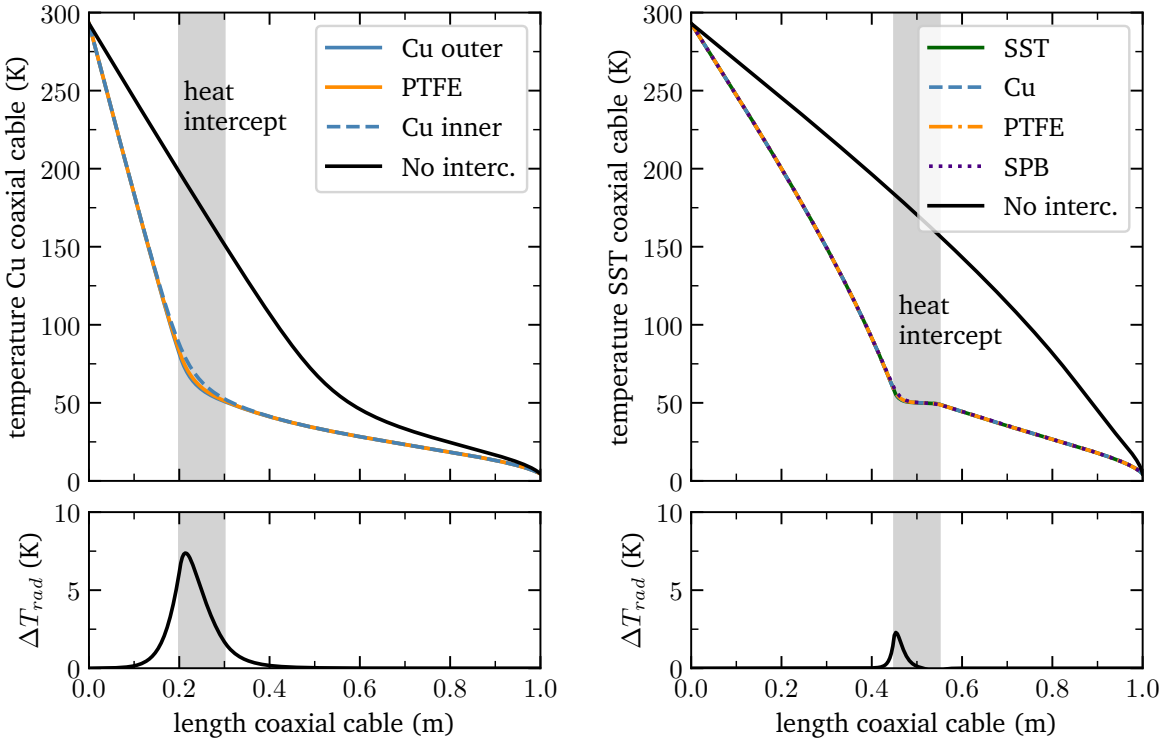

Figure 5.4: *Temperature distribution inside the Cu (left) and SST (right) coaxial cable layers along their length. The black line shows the average temperature inside the cable without heat intercept at the TS. The gray background highlights the position of the TS heat intercept. ΔT_{rad} displays the radial temperature difference between the inner most and outer most layer. Cu = copper layer, PTFE = Polytetrafluoroethylene layer, SST = stainless steel layer, SPB = silver plated brass layer.*

leads to an experimental heat leak of 0.010 W and a calculated value of 0.008 W. The second case of 100 K reveals 0.188 W and 0.067 W, respectively. The model matches the experimental data only for the first case in a satisfactory way and predicts less conservative values. This could be attributed to inaccurate choices of thermal conductivity and thermal boundary values but the small amount of data limits valuable insights. The inaccurate representation further motivates the experimental testing of the later chosen cable. For the present heat load estimation the results are multiplied by 3 in order to allow for margin.

The motivation of the preceding investigation was to find the setup with the lowest attenuation and heat leak. Following this, it is proposed to use the SST coaxial cable for the part between room temperature and the IVC thermalization plate (see Figure H.10). Utilizing the copper coaxial cable would lead to considerable higher attenuation for the same thermal behavior. The heat intercept at the TS at 50 % of the length of the cable via flexible links shows to be effective and convinces by substantially reducing the heat load at 4.5 K. The results of the temperature distribution suggest that the thermal contact at the heat intercept by clamping is sufficient to thermalize the inner conductor

layer. Between the feedthrough at the IVC thermalization plate and the connections to the cavities, the copper coaxial cable may be used in order to minimize the attenuation. There, the coaxial cables are covered by a single sheet of MLI to reduce the absorption of thermal radiation from the surrounding TS. A similar heat load is discussed for the tuning system in Section 5.4.3. For the coaxial cables no substantial heat load from thermal radiation inside the bore is expected. It has to be noted that the SST coaxial cable is considerably stiffer and, thus, not easy to thermalize at the copper plate. Therefore, it is proposed to thermalize the copper coaxial cable on the plate on the outside of the IVC. In summary Table 5.2, only the heat leaks from all SST coaxial cables in the above described layout with the additional multiplier of 3 are listed. However, it was shown that the heat load from the coaxial cables can be substantial and it seems compelling to experimentally test the coaxial cables that are chosen in the later stages of the project. Through such investigation it should be possible to improve the accuracy of the estimation for the expected heat loads.

5.4 Other heat loads

5.4.1 Support structure and IVC

The support structure denotes the needed mechanical support inside the BabyIAXO bore to secure the cavities, the TS, and the auxiliary equipment. The final and detailed design of the support structure is beyond the scope of this work, as it requires extensive studies of the mechanics and stability, as well as the finalization of the cavity design. Here, preliminary estimations for the choice of material and the heat leak through the support structure are given. When designing a support structure for a cryogenic environment, particular care must be taken in the choice of material. The material has to endure large temperature differences and an external magnetic field, while allowing small amounts of heat into the system. Following (5.1), a low cross section, a large distance between the thermalization points and a low thermal conductivity are preferred for the support structure. This leads to an optimization between the material properties of thermal conductivity, elasticity, and maximum allowable stress.

It is planned to use a support system made of G10 epoxy-fiberglass. G10 provides a high tensile strength of about 260 MPa [109], while offering an excellent low thermal conductivity, a reasonably low thermal contraction in the glass fiber direction, and a weak magnetic reaction [81]. Rods reach from the BabyIAXO bore to the CM and bearings of zirconium oxide ball transfer units, like the ball transfer units 515-0-15 from Alwayse Engineering® [110], are placed at both ends. The TS is permanently fixed to the rod system and the G10 rods are thermalized at the TS via copper braids to intercept the heat flow to the CM. The ball transfer units enable both the sliding of the structure of TS and support structure into the BabyIAXO bore and the sliding of the cavities onto the support structure, thus, fulfilling the requirements of easy insertion of the cryostat into the bore and interchangeability of cavities. Measurements at the CCCL revealed that the effective thermal conductivity

through the zirconium oxide ball transfer units is higher than of bulk G10 [111]. Following this, the heat transfer is limited by the G10 rods and the ball transfer units are neglected in the following thermal calculation.

To assess the heat leak through the support structure, first, the mechanical load on the supports needs to be estimated. The mechanical load results from the weight of the CM and the TS. The supports between CM and TS need to bear only the mass of the CM and the supports between TS and bore need to bear the combined mass. The corresponding weights are approximated with the surface area, described above in Section 5.2.2, the density of the material, and the wall thickness. The cavity is made out of SST, coated on both sides with copper, or purely out of copper and has an estimated thickness of 5 mm. To be conservative, the density of pure copper is used for the estimation. The TS is composed out of 2 mm thick copper. Thus, masses inside the BabyIAXO bore of about 900 kg for the CM and 400 kg for the TS, respectively, are estimated. The minimum cross section of the supports corresponds to the ratio of the specified mechanical load and the maximum stress of the yield strength. An additional factor of three is multiplied with the cross section to depict good engineering practice. This leads to the estimation of the effective cross section of the support structure as

$$A_{\mathrm{SS,eff}} = 3\frac{At\rho g}{\sigma_{\mathrm{yield}}}\,, \tag{5.12}$$

where A denotes the corresponding surface area of the CM and the TS in m^2, t the thickness in m, ρ the density in $\mathrm{kg/m}^3$, g the gravitational acceleration constant in $\mathrm{m/s}^2$, and σ_{yield} the yield strength in Pa which equals the tensile strength for G10. The effective cross section of the support structure between CM and TS corresponds to $1.0\,\mathrm{cm}^2$ and between TS and bore to $1.4\,\mathrm{cm}^2$.

Finally, the heat leak through the support structure is calculated by applying (5.1) with $A_{\mathrm{SS,eff}}$, the thermal conductivity of G10 in the normal direction according to NIST [102], and an assumed distance between the thermalization points of 5 cm each. The location of the heat intercept matches the ideal position of a TS for G10 for the present temperature range according to Association Francaise du Froid [112]. It is assumed that three of these support structures inside the bore are needed for stability. The resulting heat load corresponds to about 0.9 W at 50 K for the TS and 0.05 W at 4.5 K for the CM and is listed in Table 5.2.

The instrumentation vacuum chamber is placed inside the service box and all the electrical equipment is mounted in it. This IVC creates a separate vacuum environment for the electrical equipment and a sketch of the structure is given in Figure H.11. The chamber has a cylindrical shape with a diameter of 40 cm and a length of 30 cm. One end is attached to the flange of the outer vacuum chamber at room temperature and the other end must be cooled to low temperature. Substantial heat loads due to conduction along the short distances are expected. Therefore, the walls of the IVC are fabricated out of G10 in a meander or double wall structure, with a copper ring in a intermediate position of the meander and an end plate made out of copper (see Figure H.11). Thus, the distance between the thermalization at the TS and at the low temperature is maximized. The distance between the

outer flange and the copper ring corresponds to about 30 cm and between the copper ring and the copper plate to 40 cm. The copper ring is connected to the TS of the service box on the outside and to an inner TS on which the coaxial cables are thermally attached. The copper plate has a thickness of 1.5 cm and provides a good thermal contact between the cooling pipe at low temperature on the outside and the electrical equipment and the coaxial cables on the inside. Therefore, this copper plate is from now on named IVC thermalization plate. The thickness of 2 mm of the G10 walls results from static structural and eigenvalue buckling analyses using ANSYS® [113]. Finally, the heat leak through the structure can be calculated by simple conduction with equation (5.1). The related heat load of the IVC is appended by thermal radiation from the service box TS to the copper plate. Thus, a heat load of 1.0 W at the copper ring at 50 K and of 0.06 W at the IVC termalization plate at 4.5 K is assessed.

5.4.2 Electrical equipment

The following discussion includes the heat load of sensor wires, the switches, the LNAs, and the calibration system of the LNAs. The heat load due to the signal from the VNA through the cavities during the calibration process is estimated to be less than 1 mW and, thus, negligible compared to the other heat loads. The layout of the electrical equipment is shown in Figure H. The respective heat loads are summed up and listed in Table 5.2.

In cryogenics, sensors must be measured with a four-wire technique to eliminate the influence of the resistance of the instrumentation wires in the measurement [81]. Therefore, one sensor requires four wires which, here, consist of manganin with a diameter of AWG36 (American Wire Gauge). Equation (5.1) is utilized with the thermal conductivity of manganin according to Duthil [114]. This results in a heat load per sensor and per meter cable length of about 2×10^{-4} W m for the TS at 50 K and 1×10^{-5} W m for the CM at 4.5 K, respectively. To calculate the actual heat load, the given value needs to be divided by the length of the cable between the thermalization points. From this short estimation it seems sufficient to assume 0.1 W heat load at 50 K and 0.01 W at 4.5 K to cover the heat load from the cables.

The switches are relays which connect and disconnect electrical circuits in response to an electrical signal. The signal creates a negligible heat load and flows only a short amount of time. Therefore, the heat load from the switches is neglected.

The data taking requires one LNA for each cavity in a temperature regime where the noise curve reaches its lowest possible value. The LNA LNF-LNC4-16B from Low Noise Factory® [115] is used. In the corresponding data sheet a steady state heat load of 18 mW during operation of one LNA is specified. The resulting heat load for the present setup therefore equals 54 mW at 4.5 K.

The calibration system is needed to in-situ calibrate each LNA and consists of an electrical load connected via a coaxial cable to the switches and a manganin wire wound around the electrical load,

acting as a heater. For the coaxial cable the KEYCOM® ULT-05 [101] semi-rigid coaxial cable with a length of 10 cm is considered. The electrical load HUBER+SUHNER® 65-SMA-50-0-1/111-NE [116] seems appropriate. The electrical load itself is not thermalized, so that it can be heated up from the low temperature of the switches and the LNA to an elevated one, whereby a temperature difference of 20 K during operation is presumed. The operation cycle can be divided into three periods: heating up, steady state, cooling down. From these, the heat load during steady state can be assessed with the provided thermal conductivity of the coaxial cable [101], which corresponds to 13 mW. The duration of the other two periods is evaluated by solving the transient heat transfer from the calibration system to the switch via the coaxial cable. For that, the calibration system is conservatively approximated by 0.03 kg of brass and the specific heat correlation for brass according to Ekin [81] is utilized. This results in a total operation duration of 30 min. The maximum heat load during steady state is assumed for the whole operation cycle to be conservative. How often the calibration needs to be conducted will depend on operational experience and could be as seldom as once per day. In order to consider every influence the heat load of 13 mW at 4.5 K is added to the others but it must be kept in mind that it only arises during the calibration of the LNAs.

5.4.3 Tuning system

The components of the tuning system are assumed to be a stepper motor for each cavity, multiple piezoelectric motors, a tuning rod for each cavity and multiple metallic sheets inside the cavities. The stepper motors provide the coarse tuning movements and are located at room temperature because they have a holding current, thus a steady state heat load, and cannot tolerate external magnetic fields. After the coarse tuning movement the piezoelectric motors are used for fine tuning the cavities. Piezoelectric motors can operate in strong external magnetic fields and at low temperatures. Additionally, they offer high positioning precision and retain the position while not being powered. No substantial heat load is expected from the piezoelectric motors during their limited amount of time of active tuning. The tuning rods transmit the mechanical momentum from the motors from the outside to the metallic sheets that are mounted inside the cavities. For that, special leak tight flanges are needed that allow the turning or the rods without deteriorating the vacuum. Therefore, the only heat load on the cooling system stems from the tuning rods, that are thermalized at both room temperature and low temperature at the cavities. The following describes the approach to estimate the heat load from the tuning rods. As a simplification every tuning rod is assumed to have exactly the same thermal connections. Hence, the analysis focuses on a single tuning rod and its results are multiplied by the number of rods or cavities for the heat load summary in Table 5.2.

As a first estimation, the tuning rod consists of G10 in the shape of a hollow cylinder with an outer diameter of 12 mm and a thickness of 3 mm. It is covered by a single sheet of MLI to reduce the absorption of heat from thermal radiation. The rod enters the vacuum chamber at the service box from room temperature and gets thermalized at the TS. Afterwards it is routed through the transfer line and is connected to each cavity at two points, where the heat is deposited. A length of 13 m is

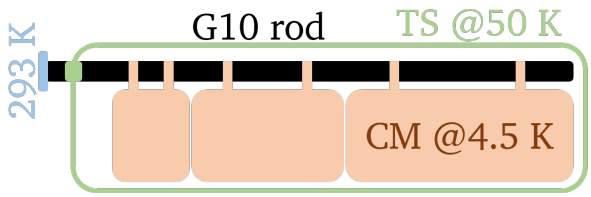

Figure 5.5: *Sketch of one tuning rod made out of G10. The rod is enclosed of the TS and has multiple thermalization points and connections at room temperature, the TS and the CM.*

assumed for the tuning rod inside the vacuum chamber. The center of the thermal connections from left to right along the length of the rod are as follows: at 0 m connection to the outside, at 0.3 m connection to the TS with a connection length of 10 cm, and at 4 m, 5 m, 6 m, 8 m, 9 m, and 12 m connection to the CM with a length of 5 cm. The tuning rod is enclosed by the thermal shield, which emits thermal radiation. The assumed layout is presented in Figure 5.5. This setup, consisting of multiple thermalization points and the continuous absorption of thermal radiation, leads to a complex temperature distribution inside the tuning rod. A 1D numerical model, sketched in Figure 5.6, approximates this distribution.

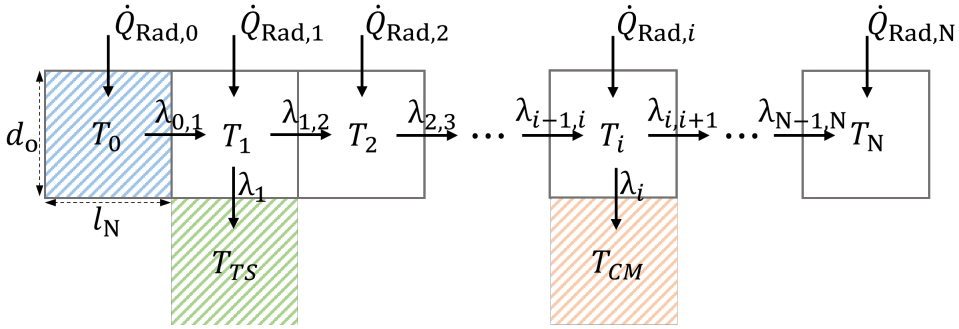

Figure 5.6: *Schematic of the 1D numeric model of the temperature distribution inside the tuning rod. Heat transfer via thermal radiation, solid conduction inside the rod, and radial solid conduction at the thermalization points are considered. The boundary conditions are highlighted by colored hatched regions.*

The tuning rod is divided into $N = 500$ volume elements of length l_N and a constant temperature, thus neglecting radial temperature differences. N is chosen so that the computing time remains reasonable and the solution does not depend on the resolution. One volume element is exposed to solid conduction with both neighboring elements, external heat load from thermal radiation and possible solid conduction to the thermalization points of the TS and the CM (see Figure 5.6). The thermal conductivity between the volume elements corresponds to the arithmetic mean of the two thermal conductivity values of the neighboring elements, which are calculated by the temperature dependent correlation for G10 in the normal direction according to NIST [102]. The external heat load is modeled according to (5.5) and (5.6) by assuming a constant temperature of the TS and a full enclosing by the TS. The emissivity of the TS made out of copper equals $\varepsilon_\mathrm{TS} = 0.06$ and the emissivity

of the single MLI covered tuning rod $\varepsilon_{\text{rod}} = 0.06$. Lastly, the heat transfer at the thermalization points is assumed to be dominated by the thermal conductivity of G10 of the volume element, therefore neglecting thermal boundary resistance, and assuming constant temperatures of the TS and the CM. A Dirichlet boundary condition of constant room temperature at the first element and a Neumann boundary condition of adiabatic behavior at the last node are defined. The heat transfer equations for every volume element are compiled into a matrix system of linear equations $\boldsymbol{Ax} = \boldsymbol{b}$ analogous to the system in Section 5.3, where the thermal conductivity coefficients constitute the coefficient matrix $\boldsymbol{A}$, the temperatures of the elements are the solution vector $\boldsymbol{x}$, and the external heat loads, boundary conditions, and temperatures of the thermalization points are put into the constant vector $\boldsymbol{b}$. Since the thermal conductivity values and the external heat load are a function of the temperature, $\boldsymbol{A}$ and $\boldsymbol{b}$ depend on $\boldsymbol{x}$, which makes an iterative calculation necessary. The system is solved and updated until the changes in the temperature vector are sufficiently small (relative change of the values $< 1 \times 10^{-5}$).

The temperature distribution of the rod and the heat transferred at the thermal connections can be recovered from the solution of the temperature vector. Following this calculation, the heat load from one rod covered by a single sheet of MLI in the above outlined configuration corresponds to 89.8 mW for the TS and 7.1 mW for the CM, respectively. In order to compare the heat load with a configuration where the tuning rod is not covered by MLI, the emissivity of the rod is set to $\varepsilon_{\text{rod}} = 1$, corresponding to the emissivity of G10. Simulations for an uncovered tuning rod reveal a heat load of 193.9 mW for the TS and 38.5 mW for the CM, respectively. It seems worthwhile to note that the heat load to the TS intercept more than doubles for the uncovered case which can be attributed to the thermal radiation absorption of the short part between the vacuum chamber and the TS. Figure 5.7 depicts the temperature distribution of the tuning rod along its length for the two discussed cases.

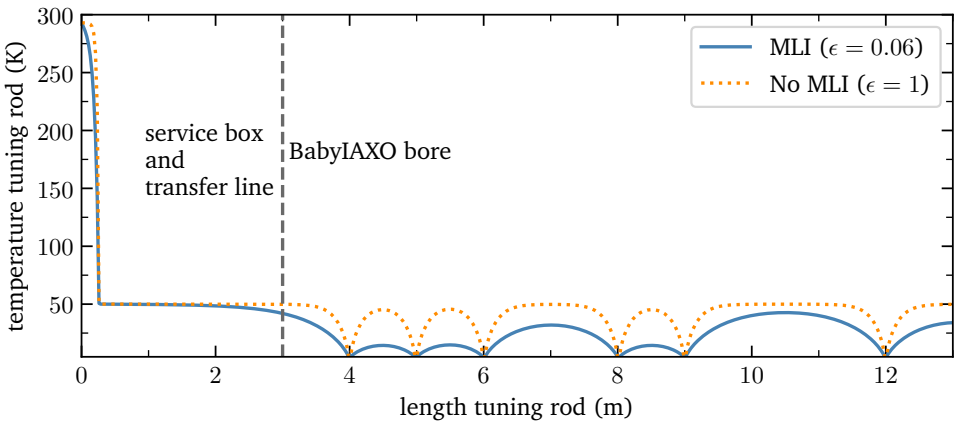

Figure 5.7: *Temperature distribution for one tuning rod along its length in steady state according to the presented 1D model. The rod is thermalized at the TS and at multiple connections at the CM. The options of covering the rod with a single sheet of MLI ($\varepsilon = 0.06$) and not covering the rod ($\varepsilon = 1$) and are compared. The boundary between the transfer line and the bore is marked with a grey dashed line and annotated accordingly.*

5.5 Heat load on the present system

The heat loads from the defined components are calculated in steady state following the above detailed descriptions, summed up and presented in Table 5.2. These heat loads correspond to a system with the three distinct temperature levels of room temperature (293 K), TS temperature (50 K), and CM temperature (4.5 K). Note that the heat loads occur and get absorbed by the cooling system at different places (see Section 4.5). The heat leak through the MLI of the TS inside the service box, through the coaxial cables, the heat load due to the electrical equipment, and due to the thermalization of the tuning system at the TS temperature all occur in the service box. This results in a heat load for the cooling system inside the service box of 7.1 W at 50 K and 0.31 W at 4.5 K. Consequently, the remaining heat leak through the MLI of the TS and the CM of the transfer line and the bore, through the support structure, and through the tuning system must be compensated by the cooling system inside the bore. The heat load inside the bore reads 30.2 W at 50 K and 1.38 W at 4.5 K.

Table 5.2: *Summary of heat loads in steady state at the two temperature levels of the RADES BabyIAXO cryostat. The heat load values, the sources and the locations of their occurrence are specified.*

Source	Heat load @50 K (W)			Heat load @4.5 K (W)		
	Service box	Bore	Total	Service box	Bore	Total
Radiation / MLI	3.3	29.3	32.6	-	1.31	1.31
Coaxial cables	2.4	-	2.4	0.18	-	0.18
Support structure & IVC	1.0	0.9	1.9	0.06	0.05	0.11
Electrical equipment	0.1	-	0.1	0.07*	-	0.07*
Tuning system	0.3	-	0.3	-	0.02	0.02
Total	7.1	30.2	37.3	0.31	1.38	1.69

* partly dynamic and not steady state heat load, see Section 5.4.2 for more details.

The listed heat load corresponds to the constant TS and CM temperatures of 50 K and 4.5 K, respectively, which are assumed to be a probable case. However, the cooling system may reach equilibrium at different TS and CM temperatures due to the characteristic cooling performance of the cryocoolers and the effectiveness of CFHX and circulator. Therefore, the accuracy of the description of the system increases by defining the heat load as a function of temperature. There exists a complex dependency between the heat load and the temperature for the multiple components. The heat load due to thermal radiation dominates the overall heat load (see Table 5.2). Thus, the MLI heat load function described in Section 5.2.2 is used in the following system optimizations, including the system layout and the thermal shield temperatures. The defined heat load function of the present system can now be applied to estimate the performance of the cryostat. For that, a thermodynamic model for the cooling system is compiled and discussed in the following Chapter 6.

6 Thermodynamic model of the system

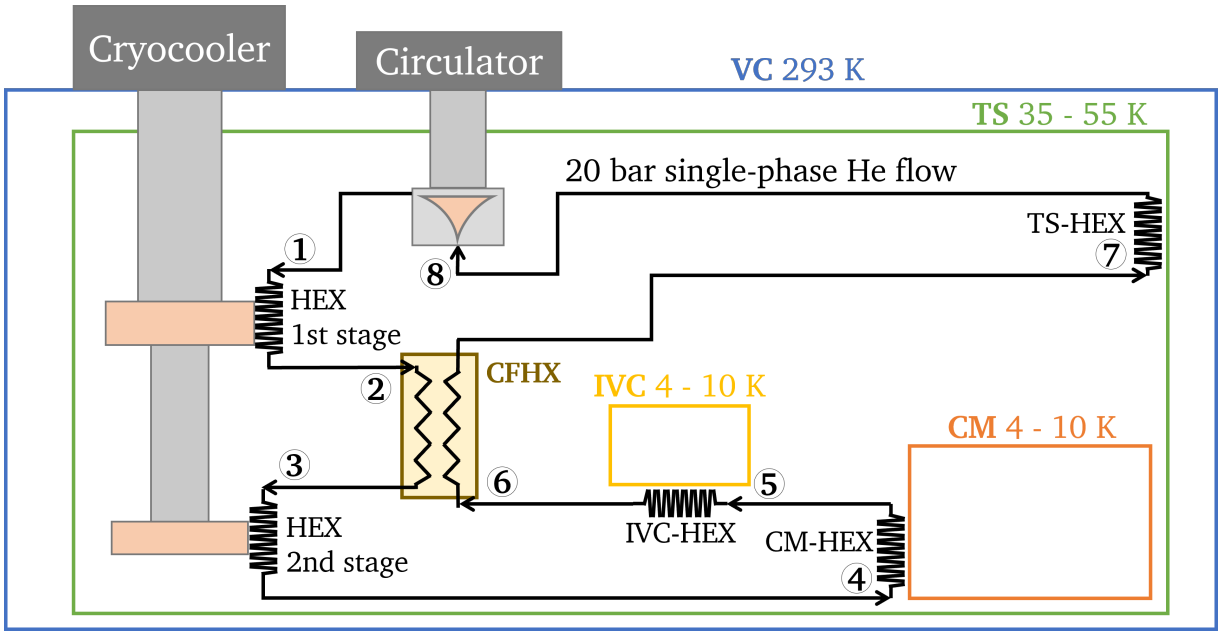

Figure 6.1: *Outline of the simplified thermodynamic system. The system is divided into separate components, allowing to calculate the change in temperature and pressure across every component. The assumed components include the circulator, the HEX at the first stage of the cryocooler, the CFHX, the HEX at the second stage of the cryocooler, and the HEXs that denote the remote cooling of TS, CM and IVC. Each location between the assumed components is numbered for reference.*

Following the definition of the values and the locations of the heat loads in Chapter 5, the next step is to investigate the cooling system. A thermodynamic model is compiled, which calculates the temperatures inside the system as a function of the heat loads while respecting the performance of the cryocooler and cryogenic circulator. It aims to estimate the temperature distribution of the cavities and to allow to optimize the mass flow rate, the cooling equipment, and the layout of the cooling system. Every change in the system can be related to its gain for the cavity temperature and the most effective design can be pursued.

The helium cooling fluid system described in Section 4.5 is displayed in Figure 6.1, where the layout is simplified and all irrelevant components are omitted. Additionally, it is divided into single components, that are connected via the cooling pipe and every point before and after a component is

numbered. For the present study nominal pressures around 20 bar are chosen, therefore, the flow is located in the supercritical regime. The mass flow rate $\dot{M}$ is varied around 0.5 g/s because this is the experimental data space for the CFHX based on first design calculations. The inner diameter d_i of the pipes is assumed to be 4 mm except for the pipe of the first stage heat exchanger (HEX), where $d_\mathrm{i} = 8\,\mathrm{mm}$ is defined.

In order to accurately describe the cooling system, first the separate components are modeled as discussed in the following Section 6.1. Then in Section 6.2 the components constituting the system are connected and the iterative calculation of the system is outlined. Lastly, Section 6.3 describes the experimental setup at the CCCL mimicking the present system.

6.1 Modeling of the components

6.1.1 Cryocooler heat exchanger

Each heat exchanger at the cold head of the cryocooler consists of a coiled copper tube that is attached to the cold head (see Figure 6.2 right). Hence, the cooling fluid can deposit the heat on the cold head stage and the length and the diameter of the pipe constituting the HEX can be customized for the expected heat load, mass flow rate, and corresponding pressure drop. The heat exchangers of the first and the second stage of the cryocooler are built analogous with different optimizations in length and diameter, respective to the different boundary conditions. This section describes the modeling of these heat exchangers, enabling the optimization and the incorporation into the model of the system.

It is assumed that the cold head and the heat exchanger pipe have the same constant temperature T_w. This seems reasonable as they are both made out of copper with a large thermal contact (see Figure 6.2 right). T_w is also called stage temperature and describes the temperature at which an equilibrium between the deposited heat on the stage and the extracted heat from the system exists. The stage temperature depends on the deposited heat load, the cryocooler model and, for two-stage cryocoolers, the other stage temperature. In order to estimate the possible extracting capacities, experimental measurements at different temperatures for the Cryomech® PT420 cryocooler [78] have been conducted at the CCCL by a preceding master student [117]. These measurements resulted in a 2D capacity map, which is attached in the appendix as Figure G.4. An interpolation between these measuring points was programmed in the previous work [118] by applying the SciPy® function CloughTocher2DInterpolator [119]. This allows to apply a mathematical function relating the extraction capacities and the temperatures of the two stages to each other.

The flow and the heat transfer in the heat exchanger is modeled by dividing the pipe into N small volume elements with the length l_N in m. The radial temperature and velocity gradients are neglected, hence, the flow is described in 1D. This assumption is compensated by the special friction

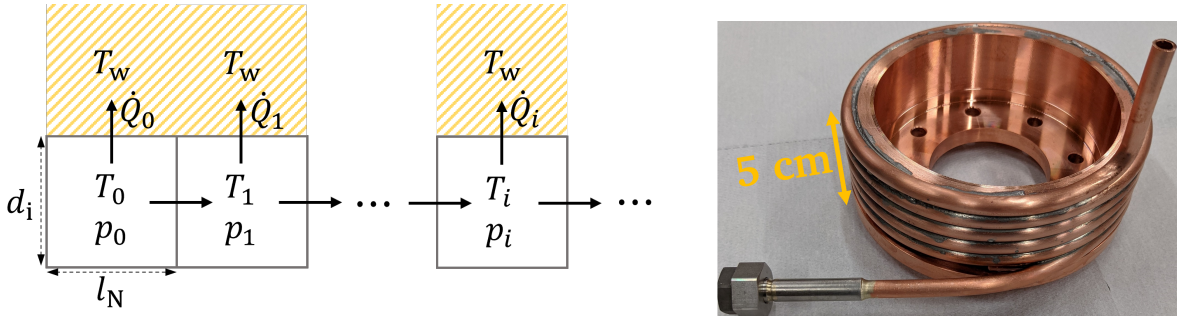

Figure 6.2: *Left: Outline of the numerical model of the heat exchanger at the cold head of the cryocooler. Right: Coiled pipe HEX to be mounted on the cold head of the cryocooler to create sufficient heat exchange.*

and heat transfer correlations for coiled tubes [80]. The changes in temperature and pressure over one volume element are neglected, thus assuming isothermal and isobaric elements. A sketch of the 1D model is displayed in Figure 6.2 left. Each volume element is exposed to the heat transfer with the wall and the convective transport to the following volume element. The emitted heat flow $\dot{Q}_i$ of one volume element i in W is calculated by

$$\dot{Q}_i = \alpha_{\text{eff}} \pi d_\text{i} l_\text{N} (T_i - T_\text{w}) \ , \tag{6.1}$$

where α_{eff} is the mean effective heat transfer coefficient in $\text{W}/(\text{m}^2\,\text{K})$, d_i the inner diameter of the tube in m, and T_i the temperature of the element in K. The heat transfer correlations for α_{eff} are taken from VDI Heat Atlas [80] for heat transfer in helically coiled tubes. The material properties required by the correlation are calculated as functions of T_i and p_i with HEPAK [120].

The present helium flow corresponds to high-pressure, low-temperature, single-phase vapor flow. Here, the compressibility of helium has a substantial influence on the flow behavior and cannot be neglected [82, 121]. The equations for 1D steady state flow of Arp [121] and Grohmann [82] are applied. The equations are based on the flow of a compressible fluid in a heated tube [121] and were validated with the experimental values of two temperature profiles in a long gaseous-helium-cooled tube by Dean et al. [122]. According to Arp [121] the pressure and temperature gradient in x-direction can be calculated by

$$\frac{\mathrm{d}p}{\mathrm{d}x} = \frac{-\frac{\zeta \dot{m}^2}{2\rho d_\text{i}} + \frac{4\dot{q}\dot{m}\beta}{\rho d_\text{i}(c_\text{p} - u^2\beta)}}{1 - \frac{\dot{m}^2}{\rho}(\chi + \beta\phi)} \ , \tag{6.2}$$

and

$$\frac{\mathrm{d}T}{\mathrm{d}x} = \frac{-\frac{\zeta \dot{m}^2 \phi}{2\rho d_\text{i}} + \frac{4\dot{q}}{\dot{m} d_\text{i}(c_\text{p} - u^2\beta)}}{1 - \frac{\dot{m}^2}{\rho}(\chi + \beta\phi)} \ , \tag{6.3}$$

with the support variable ϕ in K/Pa

$$\phi = \frac{\mu_\text{JT} c_\text{p} + u^2 \chi}{c_\text{p} - u^2 \beta} \ . \tag{6.4}$$

Here, $\dot{m} = \left(4\dot{M}\right) / \left(\pi d_\mathrm{i}^2\right)$ is the mass flux in kg/(m^2 s), $\dot{q} = \dot{Q} / \left(\pi d_\mathrm{i}\, \mathrm{d}x\right)$ the heat flux in W/m^2, and u is the flow velocity in m/s. ζ corresponds to the Darcy friction factor according to VDI Heat Atlas [80] for the pressure drop in technical smooth coiled pipes in laminar and turbulent regimes. The properties of helium are given by the isobaric specific heat capacity c_p in J/(kg K), the isobaric expansivity β in 1/K, the isothermal compressibility χ in 1/Pa, and the Joule–Thomson coefficient μ_JT in K/Pa. All properties are calculated as a function of temperature and pressure with HEPAK [120].

The gradients are approximated by $\Delta p/\Delta x$ and $\Delta T/\Delta x$, respectively, where Δx is replaced by l_N. Therefore, the solution for the volume element i reads $p_{i+1} = p_i + (\mathrm{d}p/\mathrm{d}x)\, l_\mathrm{N}$ and $T_{i+1} = T_i + (\mathrm{d}T/\mathrm{d}x)\, l_\mathrm{N}$. (6.2) and (6.3) are calculated with the element variables p_i, T_i, and $\dot{Q}_i$. The assumptions only hold true for infinitesimally small volume elements making it necessary to verify that the results are independent of the chosen N. The inlet boundary conditions T_0, and p_0 for the first volume element are provided by the preceding component in the system model.

This element-wise calculation continues until the last element from which the outlet conditions serve as result of the model. The sum of the transferred heat flows combined with possible external heat loads corresponds to the deposited heat load onto the cryocooler stage. The external heat loads include the amounts of heat which get deposited directly onto the cold head, e.g. via thermal links from the TS of the service box. There exists a complex dependency between the stage temperature and the extraction capacity. Thus, the above described calculations need to be repeated with an adapted T_w until equilibrium is reached. The full heat load of the stage determines the stage temperature in the next calculation loop.

6.1.2 Cryogenic circulator

The modeling of the cryogenic circulator is done in accordance with the specifications of the manufacturer. Attached in the appendix in Figure G.5 is the CAD drawing and Figure G.6 shows the flow graph of the Cierzo Cryofan provided by Stirling Cryogenics® [79]. Figure G.7 depicts the flow graph of the Noordenwind Cryofan also provided by Stirling Cryogenics® [79]. The flow graph characterizes the circulator by relating the provided pressure head at different volumetric flow rates for multiple impeller speeds. To determine the working point, first, the outlet pressure is chosen as the nominal pressure of the system. The inlet pressure is then calculated by estimating the pressure drop over the whole system. From this difference the pressure head that the circulator needs to provide is determined.

In order to model the temperature difference due to the circulator, three different heat loads have to be accounted for. The first one is the dynamic friction loss in the piping of the system. The circulator puts work into the gas to make it move against the pressure drop which is then emitted in the piping due to friction. This heat is therefore deposited over the whole system. Preliminary studies revealed that this heat load is small for the estimated small pressure drop and, hence, it is assumed to only occur at the circulator with the other heat loads. The second heat load comes from the non-ideal

efficiency with which the circulator is putting work into the gas. The amount of heat from these two mechanisms is estimated with two measured correlations from the manufacturer for 16 000 rpm impeller speed for the Cierzo and for 21 000 rpm for the Noordenwind circulator [79], respectively. These correlations depend on the volumetric flow rate and are assumed to be the same for all impeller speeds. The last heat load is the static heat load via conduction through the pump house and shaft of the circulator. For the Cierzo circulator [79] the manufacturer specifies two values depending on the cold temperature of the circulator: $< 5\,\mathrm{W}$ at 10 K and $< 3\,\mathrm{W}$ at 60 K. The temperatures at the circulator in the present system are expected to lie in between these two values. Therefore, the conservative value of 5 W is assumed for the static heat load. For the Noordenwind circulator [79] there is given only one static heat load value of 5 W at 30 K. Finally, the outlet temperature T_{out} is calculated by combining the three heat loads in $\dot{Q}_{\mathrm{circulator}}$ in W and estimating an arithmetic mean specific heat capacity $\overline{c}_{\mathrm{p}}$ between the inlet and outlet conditions of the flow in J/(kg K) with HEPAK [120], and reads

$$T_{\mathrm{out}} = T_{\mathrm{in}} + \frac{\dot{Q}_{\mathrm{circulator}}}{\overline{c}_{\mathrm{p}} \dot{M}} \,. \tag{6.5}$$

6.1.3 Counter-flow heat exchanger

It is planned to install a high-effectiveness CFHX from the CCCL in the present system. Information on the research can be found in Section 4.4 and in the works of Onufrena et al. [9, 10, 76, 77]. The sketch of the CFHX is shown in Figure 6.3 left and a picture of a CFHX of the CCCL from the outside is depicted in Figure 6.3 right. The CFHX consists of a coaxial tube, where the high-pressure (HP) flow runs through the center tube and the low-pressure flow (LP) runs in the outer ring-shaped tube. Mesh is placed in both flow streams to boost the heat transfer and is highlighted by a grey hatched region. The incoming and outgoing flows are labeled and marked by arrows. For the later setup in BabyIAXO a CFHX will be specifically produced and characterized, based on the current test campaign. For now assumptions have to be defined in order to be able to incorporate the CFHX in the model. Findings from the CCCL for a previous developed CFHX with a length of 22 cm at 1 bar nominal pressure, 0.5 g/s mass flow rate, and a temperature range of 5—40 K exist. These results based on experimental data and model calculations reveal a pressure drop of 4.8 mbar across the CFHX on the HP side and 5 mbar on the LP side, respectively. The experimentally obtained pressure drop needs to be scaled to the present nominal pressure of 20 bar. For that the fluid dynamics correlation of Darcy–Weisbach is assumed to be accurate and the friction factor to be constant. Then, the pressure difference of the system Δp in mbar corresponds to

$$\Delta p = \Delta p_{\mathrm{exp}} \frac{\rho}{\rho_{\mathrm{exp}}} \frac{u^2}{u_{\mathrm{exp}}^2} \,, \tag{6.6}$$

where Δp_{exp} is the experimentally obtained pressure drop in mbar, ρ the respective density in kg/m^3, and u the respective gas velocity inside the tubes in m/s. The densities are calculated with

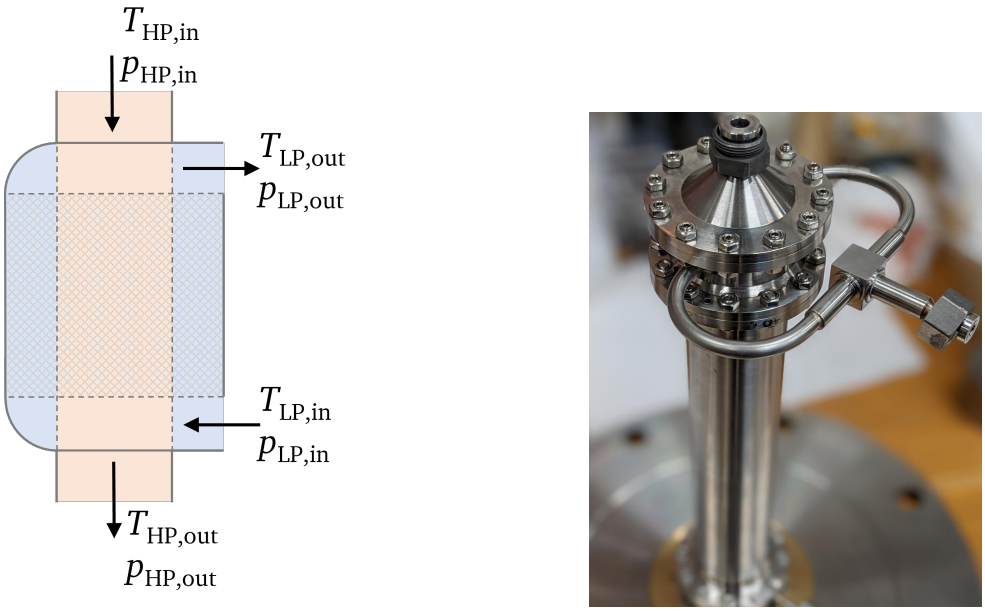

Figure 6.3: *Left: Sketch of the CFHX. The incoming and outgoing flows are labeled and marked by arrows. The high-pressure flow is colored with orange and the low-pressure flow with blue. Right: Picture of a CFHX of the CCCL from the outside. The middle inlet pipe and the outlet pipes from the side can be seen.*

HEPAK [120] as the arithmetic mean of the densities at the inlet and outlet temperature. The respective inlet pressure is known from the preceding component, therefore, the outlet pressure equals $p_{\mathrm{out}} = p_{\mathrm{in}} - \Delta p$.

The temperatures of the entering flows are known and the temperatures of the exiting flows can be calculated with the effectiveness of the CFHX [10, 118]. The effectiveness of the CFHX $\varepsilon_{\mathrm{CFHX}}$ is defined as the ratio of the actual heat transfer rate to the thermodynamically limited maximum possible rate [123], which corresponds to the specific enthalpy difference for a constant mass flow rate. For the present analysis an effectiveness $\varepsilon_{\mathrm{CFHX}} = 96.5\,\%$ is assumed based on experimental findings for the previous CFHXs. HEPAK [120] allows to calculate the specific enthalpy of helium as a function of pressure and temperature and the temperature as a function of the specific enthalpy and pressure. Thus, the maximum possible specific enthalpy difference Δh_{max} in J/kg can be calculated with

$$\begin{aligned}\Delta h_{\mathrm{max}} = \min\Big\{ & h\left(T_{\mathrm{HP,in}}, p_{\mathrm{HP,in}}\right) - h\left(T_{\mathrm{LP,in}}, p_{\mathrm{HP,out}}\right), \\ & h\left(T_{\mathrm{HP,in}}, p_{\mathrm{LP,out}}\right) - h\left(T_{\mathrm{LP,in}}, p_{\mathrm{LP,in}}\right) \Big\},\end{aligned} \tag{6.7}$$

where the minimal, limiting enthalpy difference must be used [123]. The subscripts refer to the locations in Figure 6.3. Inserting Δh_{max} in the definition of the effectiveness allows to obtain the exiting specific enthalpy with

$$h\left(T_{\mathrm{HP,out}}, p_{\mathrm{HP,out}}\right) = h\left(T_{\mathrm{HP,in}}, p_{\mathrm{HP,in}}\right) - \varepsilon_{\mathrm{CFHX}} \Delta h_{\mathrm{max}} \,, \tag{6.8}$$

and

$$h\left(T_{\mathrm{LP,out}}, p_{\mathrm{LP,out}}\right) = h\left(T_{\mathrm{LP,in}}, p_{\mathrm{LP,in}}\right) + \varepsilon_{\mathrm{CFHX}} \Delta h_{\mathrm{max}} \,, \tag{6.9}$$

respectively. Lastly, the temperatures of the exiting flows are extracted from the corresponding specific enthalpy values.

6.1.4 Remote cooling heat exchanger

The term remote cooling HEX in the present work denotes every instance where heat is transferred from an interface to helium gas that is flowing inside a cooling pipe. The TS inside the bore, the cavities, and the IVC thermalization plate are cooled via this setup. First, the modeling of the helium gas flow based on the above described fluid dynamic equations (6.2) and (6.3) is described. Then, the approach of choosing the boundary conditions that represent the remote cooling HEX is discussed.

The modeling of the remote cooling HEX is done similarly to the cryocooler HEX (see Section 6.1.1), where (6.2) and (6.3) are applied. Thus, the radial temperature gradients and velocity gradients perpendicular to the flow are neglected and single-phase compressible vapor flow is assumed [121]. The Darcy friction factor ζ according to VDI Heat Atlas [80] for technical smooth pipes for straight or coiled pipes is selected depending on the remote cooling application. The additional pressure drop across flow restrictions including bends, tees, oblique junctions, and changes in the cross section is estimated according to VDI Heat Atlas [80] with

$$\Delta p = \zeta_{\mathrm{loss}} 0.5 \rho_{\mathrm{out}} u_{\mathrm{out}}^2 \,, \tag{6.10}$$

where ζ_{loss} describes the drag coefficient of the specific restriction. ζ_{loss} is assumed to be 1.3 for a 90° arc in the pipe, 2.6 for a 180° arc, and 1 for divergent and convergent flow of multiple pipes. The subscript *out* denotes the condition directly after the flow restriction and the variables are calculated with HEPAK [120]. Isenthalpic flow across the restriction is assumed and the temperature and pressure changes are calculated iteratively in order to calculate the material properties of the outgoing flow.

The remote cooling of the TS and the CM inside the bore is planned to be achieved by creating a good thermal contact to the cooling pipes. For that, the cooling pipe is split into four pipes that are brazed onto the TS along its length (see Figure 6.4). At the end of the TS the pipes are merged into the return line, which is not thermalized to the TS. The layout for the CM-HEX could be made analogous or, alternatively, by not directly brazing the cooling pipes onto the cavities but onto a cooling rack

around the cavities. There, the thermal contact between the cooling pipes and the CM is ensured by flexible copper braids, which allows for a more flexible design of the cavities and avoids the need of brazing cooling pipes on the cavity surface. This additional heat transfer would require about 5 cm radial distance, reducing the maximum cavity diameter from 60 cm to 50 cm. A sketch of the possible layouts of the remote cooling HEX for the TS and the CM is depicted in Figure 6.4. The second option for the CM cooling is displayed. The remote cooling of the IVC thermalization plate consists of the cooling pipe which is brazed onto the plate in a meander.

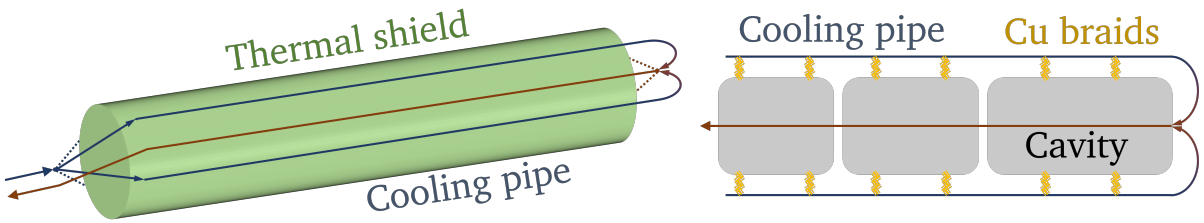

Figure 6.4: *Sketch of the remote cooling HEX via cooling pipes for the TS (left) and CM (right). The thermal contact via copper braids is displayed for the CM cooling, however, the thermal contact analogous to the TS cooling is equally possible.*

The external specific heat load $\dot{q}$ in (6.2) and (6.3) is defined to approximate the heat transferred from the cooling surface to the flow. It is assumed that the heat transfer to the helium gas is the dominating transfer. Therefore, the heat load in steady state for the respective cooling surface, presented in Chapter 5, is divided by the surface area of the pipe, and inserted as a uniform constant value. Preliminary thermal simulations with ANSYS® [113] revealed that the radial temperature gradient between the cooling pipes is substantially smaller than the longitudinal temperature gradient of the helium gas along the length of the pipe. Thus, the radial temperature gradient is neglected in the following analysis and the temperature of the helium gas is assumed to approximately describe the temperature of the cooling surface.

6.1.5 Piping inside the service box

The influence of the piping inside the service box between the above described components needs to be considered as well. The pipes are exposed to thermal radiation from the TS of the service box which is heating up the helium stream. Also there exists additional pressure drop inside the convective helium flow system due to the length and arcs of the pipe. The influence of the thermal radiation is included by applying (6.2) and (6.3) with the specific heat load $\dot{q}$ from (5.6). There, the emissivity coefficient of the TS and the pipe is assumed to be 0.05 as in Section 5.4.3. The pressure drop across the flow restrictions is approximated with (6.10) as described in Section 6.1.4. The total

length of the connecting cooling pipe inside the service box is estimated to 2.5 m and the total amount of flow restrictions inside the service box corresponds to 25 90° arcs.

6.2 Numerical model of the system

The components of the thermodynamic system have been modeled and structured into functions as described in Section 6.1. Every function requires at least one set of inlet variables, that is pressure and temperature, and gives at least one set of outlet variables. The connection of these functions aims to represent the cooling system by computing the state, that is specific enthalpy, pressure, and temperature at every labeled location of Figure 6.1. A flowchart of the numerical model, displaying the connections of the functions and the result of the respective function, is given in the appendix in Figure D.1.

The results of the functions depend on the inlet variables, thus creating a circular dependency and making an iterative calculation necessary. For the initialization of the calculation loop and for the first calculation of the CFHX, estimated values have to be defined. The convergence criterion of the calculation loop must be fulfilled before continuing with the normal calculation or finishing the simulation and saving the results. The criterion is satisfied if the relative change of the target values per full calculation loop lies below 1×10^{-5}. If convergence is not reached the estimated inlet values get updated with the calculated results by

$$\text{state}_{\text{new}} = (1 - \tau_{\text{relax}})\,\text{state}_{\text{old}} + \tau_{\text{relax}}\text{state}_{\text{calc}}\,, \tag{6.11}$$

where τ_{relax} is the relaxation factor. Choosing a relaxation factor < 1 may increase the stability of the simulation.

6.3 Experimental setup for the validation of the model

Current investigations at the CCCL include the examination of the cryocooler and helium circulation loop based remote cooling of superconducting radio frequency (SRF) cavities. In a first step a heavily reduced setup is installed to prove the feasibility of the cooling system. This setup is similar to the envisioned present system and, therefore, also used to validate the above detailed modeling. The piping and instrumentation diagram (P&ID) of the installed setup is depicted in Figure 6.5. The setup consists of a horizontal cryostat with an actively cooled liquid nitrogen aluminum thermal shield in which an insert with the cooling equipment is placed. A picture of the insert with the fundamental components of the cooling system is shown in Figure I.12. Figure I.13 displays the resistance temperature detectors (RTDs) mounted on the insert. The cooling application "simulated cavity" is separated from the insert and must merely be connected to the helium circulation loop in order to receive cooling power at low temperature as shown in Figure I.14. One Cryomech® PT420

cryocooler [78], one Stirling Cryogenics® Böhmwind cryogenic circulator [79], and one in-house produced CFHX constitute the cooling system. Copper and SST pipes connect the components and act as HEXs at the two cryocooler stages. The HEX pipe at the first stage is made out of copper and has a length of 2.4 m and an inner diameter of 16 mm. The second stage HEX has a length of 2.3 m, an inner diameter of 6 mm and is also made out of copper. The remaining connecting pipes also have an inner diameter of 6 mm. A copper shield is connected to the first stage of the cryocooler, providing active cooling to the 10-layer MLI by which the insert is covered. A flexible electric heater glued to a copper plate is installed as cavity mockup. Electric heaters produce heat as a function of electric current and resistance due to Joule heating [81]. The copper plate is cooled by the helium gas flow inside an 8 mm inner diameter pipe in a meander. The helium system pressure can be regulated with a supply bottle at room temperature (see Figure 6.5). The mass flow rate is controlled by the cryogenic circulator and the temperatures of the cryocooler stages are regulated by electric heaters, which are each connected to a proportional–integral–derivative (PID) controller.

In order to imitate the present system an electric heater after the first stage HEX introduces the heat load due to the remote cooling of the TS inside the BabyIAXO bore. Analogously, the cavity mockup mimics the CM at low temperature. Both electric heaters can introduce a defined amount of heat into the system at the two temperature levels, thus, producing meaningful data. However, the experimental setup is no perfect representation of the present system as the cryostat includes the liquid nitrogen-cooled aluminum thermal shield and the Böhmwind instead of the Cierzo or Noordenwind cryogenic circulator [79] is installed. The Böhmwind cryogenic circulator [79] provides circulation for a vastly greater volume flow range, hence, working ineffectively at the estimated low mass flow range of the present system [79]. The above detailed thermodynamic model is adjusted to the experimental setup. The Böhmwind cryogenic circulator [79] is modeled analogously to the Cierzo circulator [79] (see Section 6.1.3) in accordance with the manufacturer. The cryocooler HEXs are matched to the above described dimensions. Every length, flow restriction, and heat input due to radiation of the connecting pipes are taken into account as outlined in Section 6.1.5. This modeling of the experiment aims to enable the study and verification of the influences and trends in the experimental setup, as well as demonstrating the transfer from model to reality. Different pressures and mass flow rates are to be adjusted and the resulting possible cooling powers at the TS and CM mockups are compared.

The locations of the installed sensors are depicted in Figure 6.5, where TT = temperature transducer, PT = pressure transducer, PDT = differential pressure transducer, EH = electric heater, HV = hand valve, and SV = safety valve. The temperature is assessed with Pt100 (TT850–T854) and TVO (TT855–TT858) RTDs. These sensors change their resistance as a function of temperature, where the resistance increases with temperature for the Pt100 sensors and decreases with temperature for the TVO sensors. The sensitivity, that is the gradient of resistance as a function of temperature, reaches its maximum at high temperature for the Pt100 sensors and at low temperature for the TVO sensors [82]. Thus, the Pt100 sensors are installed at the high temperature locations of the system ($> 50\,\mathrm{K}$) and the TVO sensors at the low temperature locations ($< 20\,\mathrm{K}$), respectively. Applying a defined current

and measuring the voltage drop across the sensor allows to determine the resistance and, hence, the temperature of the sensor. Such voltage drops need to be measured in a four-wire configuration to eliminate the influence of the resistance of the instrumentation wires and their variation with temperature [81]. The fluid pressure is measured as differential pressure in order to quantify the pressure drop inside the CFHX and as absolute pressure to determine the overall pressure in the piping system and the insulation vacuum. The differential pressure sensors are based on the expansion of a membrane and are located outside of the system at room temperature. For that, small pressure pick-up capillaries are attached to the cooling pipe at least ten pipe diameters away from the last flow disturbance at flow equalizers to reduce the influence of the flow distribution in the measurement. The absolute pressure sensor transforms pressure into current via a piezoelectric device. Finally, the mass flow rate is assessed via the temperature difference of the flow due to the heat input from electric heater EH732 (see Figure 6.5). This was the chosen method due to size restrictions of the installation. The electric heater is mounted on a pipe and the temperature of the flow is measured with two neighboring Pt100 sensors. The sensors are placed at a distance to the electric heater on a SST pipe to reduce the influence of heat conduction through the walls of the pipe. It is assumed that the flow is not influenced by external factors and that the temperature of the sensors describes the mean temperature of the flow with sufficient accuracy. Then, the mass flow rate $\dot{M}$ in kg/s can be calculated as a function of the electric heater heat load $\dot{Q}_{EH}$ in W by

$$\dot{M} = \frac{\dot{Q}_{EH}}{\overline{c}_{\mathrm{p}} \Delta T} \,, \tag{6.12}$$

where ΔT is the temperature difference of the two sensors in K and $\overline{c}_{\mathrm{p}}$ is the mean isobaric heat capacity in J/(kg K) between these two temperatures calculated with HEPAK [120]. The two Pt100 sensors are adjusted to each other in-situ at the same conditions without any heat load to improve the accuracy of the calculation, thus, taking into account the parasitic heat loads, the thermal contact to the pipe, self heating, and other effects of reality. Also, the applied heat load must create a substantial temperature difference in the flow to reduce the influence of parasitic heat inputs. It is known that this assembly cannot reach the precision levels of commercial mass flow transducers but is installed nevertheless as a practical solution in the first system design. More information on the measurement procedure, the installed devices, and the calculation of uncertainty in the measurement is given in the appendix in Chapter E.

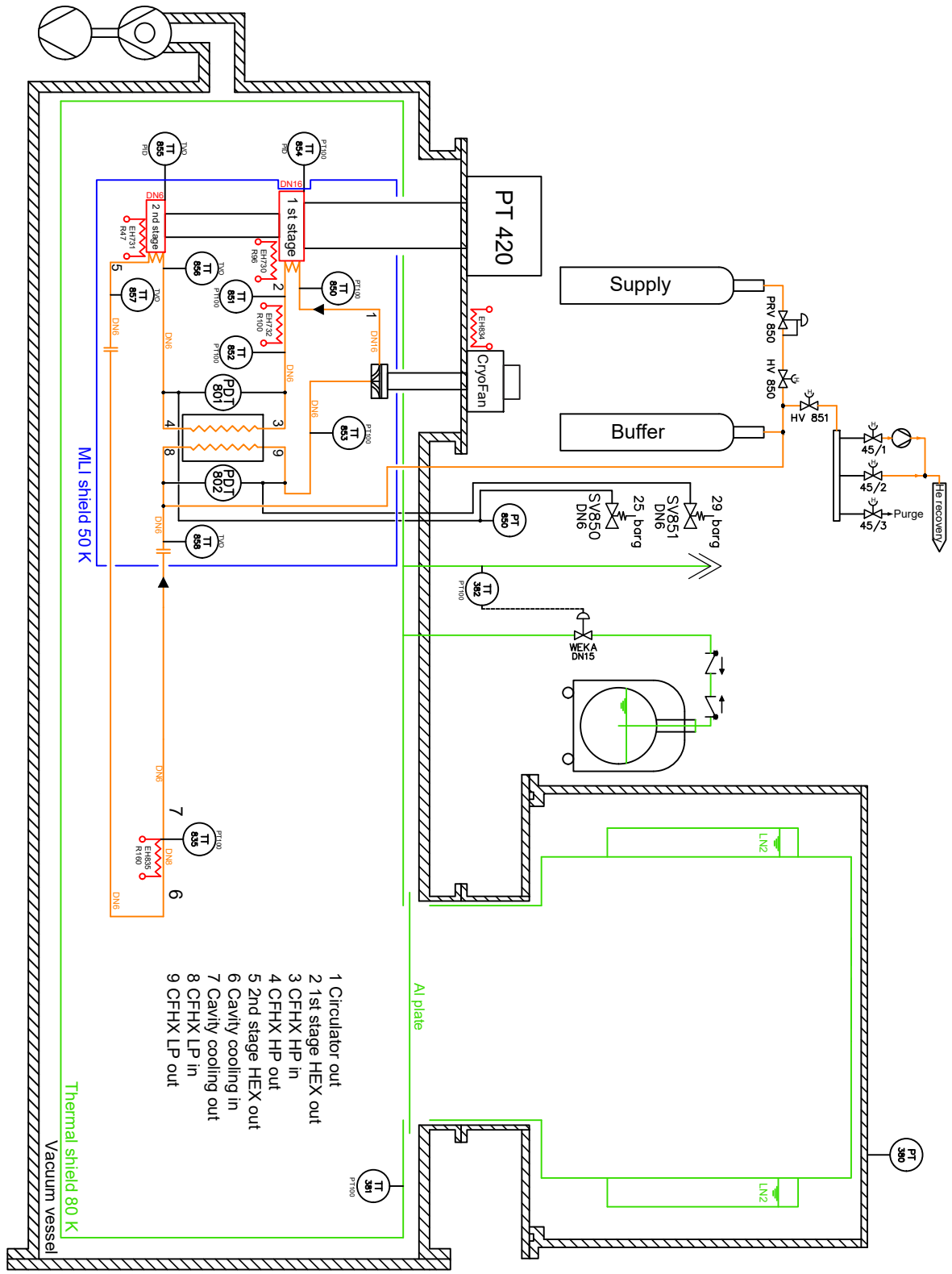

Figure 6.5: *P&ID of the experimental setup at the CCCL for the investigation of the cryocooler and closed helium circulation loop based remote cooling . The orange lines indicate the helium circulation loop. In a first step electric heaters are used to simulate the cooling of the CM and the TS inside the BabyIAXO bore. TT = temperature transducer, PT = pressure transducer, PDT = differential pressure transducer, EH = electric heater, HV = hand valve, SV = safety valve.*

7 Results and discussion

This chapter discusses the results of the experimental validation and the thermodynamic model. In Section 7.1 the measured values of the experimental setup at the CCCL are presented and compared with results from the corresponding model. The operation of the cryogenic circulator and the temperature levels of the cooling loop are discussed. Afterwards, in Section 7.2 various parameters of the cooling system are analyzed with the thermodynamic model and the consequent optimal layout and operating conditions are proposed. Section 7.3 summarizes the whole layout of the BabyIAXO-RADES cryostat as the result of the findings of the present study.

7.1 Experimental results

The operation of the present experiment faced some challenges. Only a low temperature level of about 13 K instead of the envisioned $4-10$ K was reached due to an excessive background heat load and the system demonstrated a susceptibility for pressure oscillations. However, this acted as the first commissioning and operation of such a cryocooler and circulator based system without relying on the Joule-Thomson cooling effect and the compression of the flow at room temperature as in [76]. The results clearly indicate that the cryogenic circulator is able to overcome the required pressure drop in a large mass flow rate range as intended and that the system works in principle. The unexpected high heat load at low temperatures is attributed to a poor installation of the liquid nitrogen thermal shield and of the MLI around the insert of the cooling system. Additionally, pressure oscillations causing temperature oscillations, as well as the formation of ice on the pressure pick-up lines indicated the occurrence of spontaneous thermal acoustic oscillations (TAOs) or Taconis oscillations [124]. These TAOs can transport a substantial amount of heat into the system and are often observed in tubes in cryogenic systems where a large temperature gradient along the length of the tube exists and the tube is closed at room temperature [82], making the lines in the present system predestined for oscillations. However, no TAOs have been detected at the pressure pick-up lines of similar setups at the CCCL so far. The stable and unstable regions of TAOs depend on the existent inertial force and the viscous resistance and, thus, are a function of many parameters including the temperature gradient, the pressure regime, tube diameter, and possible buffer volume at room temperature [125, 126]. In the present system the stability against TAOs could be increased by installing a small orifice at the warm end, acting as a resistor-capacitor filter, or inserting a wire along the tube to increase friction. Additional thermalization of the pick-up lines at the thermal

screen of the first stage of the cryocooler can further reduce the tendency to form TAOs in the pick-up lines. The areas of improvement, therefore, include the renewal of the presumably faulty MLI around the insert of the cooling equipment, improving of the thermal contact of the cover to the cryostat top unit, the investigation of the TT857 sensor (maybe the sensor touches the MLI or got damaged during installation), and the increase of stability against TAOs. These improvements seem feasible and were only not possible to execute in the present work due to time constraints. Thus, they remain to be implemented for the planned subsequent measurement campaigns.

The mass flow rate is measured according to the above outlined description in Section 6.3 and Figure 6.5 at two nominal pressures of (12.21 ± 0.07) bar and (18.45 ± 0.07) bar (PT850). During these measurements the first and second stage of the cryocooler were controlled at (55.0 ± 0.1) K (TT854 and EH730) and (13.0 ± 0.2) K (TT855 and EH731), respectively. First, the circulator was set to a defined impeller speed and the in-situ adjustment of the two Pt100 sensors was recorded. Then, a heat load of (2.28 ± 0.03) W (EH732) was applied and the arising temperature difference was inserted in equation (6.12). The resulting mass flow rates for the two nominal pressures at different circulator impeller speeds are depicted in Figure 7.1 left. The mean temperature between inlet (TT853) and outlet (TT850) of the circulator spanned between (58.0 ± 0.9) K at the lowest mass flow rate and (67.5 ± 0.9) K at the highest mass flow rate. Tabulated data including the uncertainty of the measurement is given in Table F.4. The results suggest a satisfactory control of the mass flow rate via the cryogenic circulator by achieving stable operation between (0.11 ± 0.01) g/s and (0.96 ± 0.29) g/s. A near linear correlation is visible between the impeller speed and the mass flow rate for both pressure regimes. Figure 7.1 right depicts the heat load introduced by the cryogenic circulator (see Section 6.1.2). Experimental and calculated results are compared at the measured mass flow rates. The experimental data is obtained by applying equation (6.12) for the two temperature sensors that measure the temperature of the inlet and outlet flow of the cryogenic circulator (TT853 and TT850). The experimental and modeling approach yield a positive correlation between the mass flow rate and the heat load in a similar range. The experimental data, however, shows a steeper dependency and the model overestimates the heat load at low mass flow rates and underestimates the heat load at high mass flow rates. A possible reason for this discrepancy might be that a constant static heat load is assumed in the model, independent of temperature and impeller speed. Also, the parasitic heat loads in the system could interfere with the measurement result.

The aim of the experiment was to validate the presented thermodynamic model. However, the high parasitic heat loads demanded adjustments in the modeling. The capacity map for the PT420 cryocooler [78] in Figure G.4 is exceeded by the present temperatures and needed to be extended by unpublished data. Also, an offset heat load due to radiation and TAO is added at the cooling interface. This offset heat load is obtained from previous measuring points at similar operating conditions without external heating of the cavity mockup. The operating conditions of these measuring points are applied to the model and the artificial heat load on the cavity mockup is increased until the second stage temperature matches the experimental data. Following this approach a constant offset heat load of 6.3 W was found. Figure 7.2 depicts the comparison between the experimental and

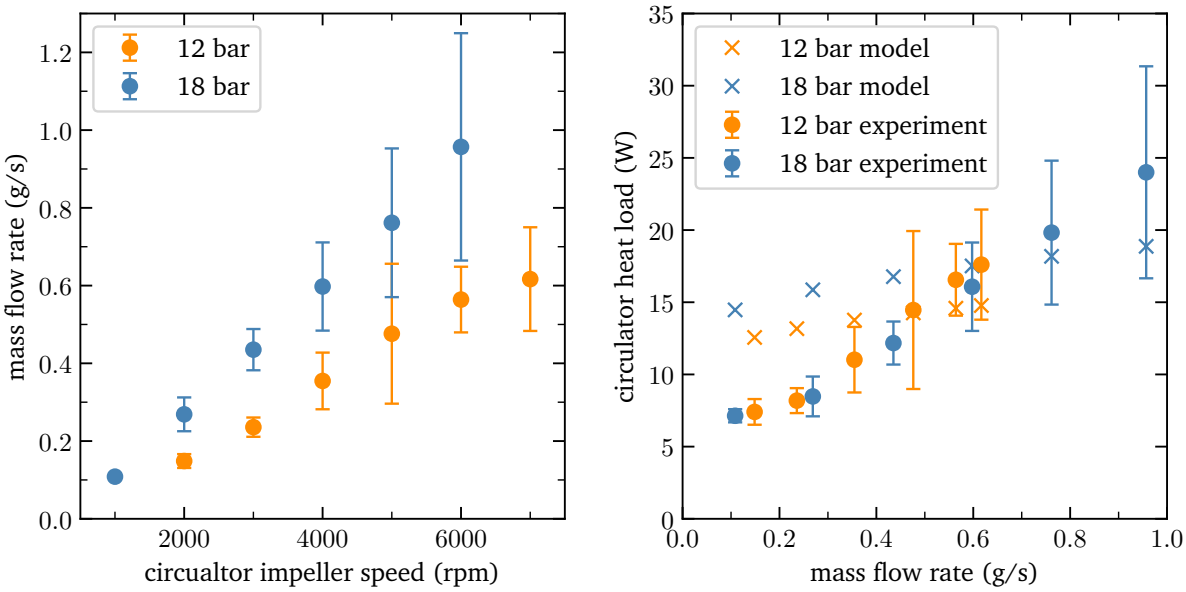

Figure 7.1: *Left: Experimental mass flow rate of the supercritical helium flow for different Böhmwind circulator [79] impeller speeds at two nominal pressures* ((12.21 ± 0.07) bar *and* (18.45 ± 0.07) bar) *and at* (55.0 ± 0.1) K *and* (13.0 ± 0.2) K *first and second stage of the PT420 cryocooler [78], respectively. The mean temperature between inlet and outlet of the circulator corresponds to* (58.0 ± 0.9) K *at the lowest mass flow rate and* (67.5 ± 0.9) K *at the highest mass flow rate. Right: Experimental heat load from the Böhmwind circulator [79] for different mass flow rates at two nominal pressures* ((12.21±0.07) bar *and* (18.45±0.07) bar). *Additionally, the heat load from the circulator calculated with the thermodynamic model is depicted. The operating conditions are the same as in the left plot and the horizontal error bars of the mass flow rates are omitted to increase clarity.*

modeled temperatures in the system for two pressure and mass flow regimes. The temperature is plotted against the names of the sensors of Figure 6.5 in arbitrary distance to illustrate the cooling loop. The first measuring point is obtained at (12.41 ± 0.07) bar, (0.48 ± 0.18) g/s (5000 rpm), by regulating the first stage of the cryocooler at (55.0 ± 0.1) K (TT854 and EH730) and introducing (6.36 ± 0.14) W at the cavity mockup (EH835). The second measuring point is recorded analogously at (18.74 ± 0.07) bar, (0.60 ± 0.11) g/s (4000 rpm), and (6.36 ± 0.14) W. The tabulated data of this comparison together with the respective measurement uncertainty is presented in Table F.5 in the appendix. The two temperature levels separated by the CFHX are clearly visible in Figure 7.2 and the data shows little difference between the two pressure regimes. The calculated data matches the measured temperatures at the second stage level convincingly, given that the adjustment of the offset heat load was done at a different measuring point. At the first stage temperature level the model predicts temperatures lower than the measured data by about 5 K. The good fit at low temperatures and the underestimation at high temperatures might suggest additional parasitic heat loads at high temperatures that are not covered by the assumed heat load of 6.3 W. Also, the measured substantial temperature increase in the piping between the first stage HEX (TT854) and the CFHX inlet (TT852)

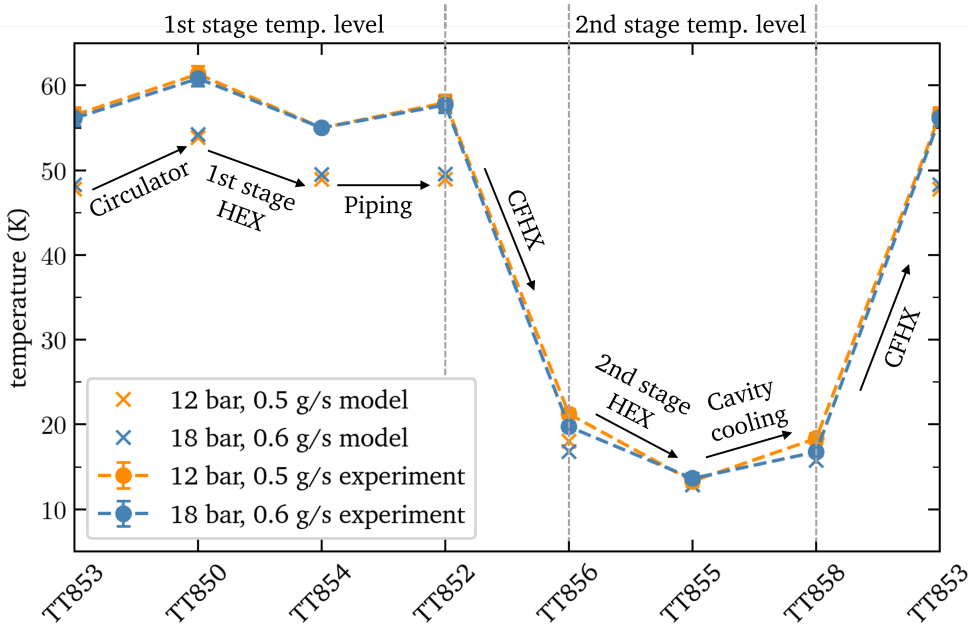

Figure 7.2: *Experimental and modeled temperature results illustrating the cooling loop at two pressure and mass flow regimes. The system is operated at a nominal pressure of* (12.41 ± 0.07) bar *and* (18.74 ± 0.07) bar *and a mass flow rate of* (0.48 ± 0.18) g/s *and* (0.60 ± 0.11) g/s*, respectively. An external heat load of* (6.36 ± 0.14) W *and* (5.20 ± 0.12) W*, respectively, is introduced at the cavity mockup. The first stage of the PT420 cryocooler [78] is regulated at* (55.0 ± 0.1) K *and the second stage is not regulated. The conditions of the experiment are applied to the thermodynamic model and an offset heat load of* 6.3 W *from a measurement without external heating of the cavity mockup is added to the cavity. Naming of the sensors according to Figure 6.5.*

provides evidence for the existence of additional parasitic heat loads. The modeled results indicate only a marginal temperature increase in this pipe part due to pressure drop and thermal radiation. However, given the required adjustments, these findings should be validated in the next measurement runs.

Overall, the presented findings suggest an acceptable first operation of the system. The high parasitic heat loads at low temperature made a conclusive validation of the thermodynamic model impossible. Future research will have to confirm the effectiveness of the envisioned cooling system and the matching of the thermodynamic model. For now the predictions of the model are cautiously trusted. However, no model can depict reality perfectly, which is why the calculated values should be interpreted with a large uncertainty.

7.2 Optimization with the thermodynamic model

First, the optimal system layout, i.e., the sequence of the components in the cooling system, is investigated with the thermodynamic model. Then, different cryocooler and circulator options and their influence on the CM outlet temperature are discussed. The optimal pressure and mass flow regime according to the model are presented. Lastly, the influence on temperature of using a cooling rack around the cavities and not installing the IVC is estimated.

The thermodynamic model for the BabyIAXO-RADES cryostat and its calculated temperatures at every position allow to find the optimal system layout, i.e., the sequence of components that results in the lowest temperature for the cavities and the electrical equipment. The physical temperature of the cavity and the LNA, respectively, can dominate the thermal noise temperature for the RADES experiment. Hence, the temperature of the helium gas flow at the outlet of the CM is the primary performance indicator, while the temperature at the IVC should not deviate substantially. The components are connected via the cooling pipes and differing sequences in the cooling system result in different temperature levels, effectiveness, and heat loads. In order to find the optimal system layout, various sequences for a system consisting of a single PT420 cryocooler [78], a Cierzo circulator [79], a first stage HEX length of 2 m, and a second stage HEX length of 2 m for a nominal pressure of 20 bar and a mass flow rate of 0.5 g/s are investigated. Table 7.1 shows the resulting temperatures of the helium gas flow at the TS and CM inlet and outlet, respectively, as well as at the IVC outlet. The default layout is sketched in Figure 6.1 and the change in sequence is then highlighted in Table 7.1 in bold. From the data in Table 7.1 it becomes apparent that the optimal system layout is not trivial and contains many complex dependencies. The temperature difference between CM and IVC seems minor. Consequently, layouts in which the CM is cooled before the IVC are pursued further in accordance with RADES. Additionally, the default layout of Figure 6.1 results in the lowest outlet CM temperature and the temperature difference of 0.5 K across the CM seems acceptable. Therefore, this layout is proposed for the BabyIAXO-RADES cryostat.

An additional PT420 cryocooler [78] can be considered, if the cooling power of one cryocooler produces insufficiently low temperatures and system optimization options are exhausted. This additional cryocooler costs about 60 000 € at the time of writing and the two cryocoolers can be connected to the cooling pipe system in series or parallel. For a setup of two cryocoolers in series the cooling pipes connect from the first stage of the first cryocooler to the first stage of the second cryocooler. The second cryocooler, thus, can extract heat at a lower temperature level. In the case of two cryocoolers in parallel the mass flow is split in half and each half runs through the stage HEXs. There, a lower extraction temperature is reached due to the lower mass flow rate and the resulting lower transferred amount of heat. The presented options of a single PT420 cryocooler [78], two cryocoolers in parallel and two cryocoolers in series are compared by displaying the temperature of the CM outlet for different mass flow rates in Figure 7.3 left. Here, the pressure head of the system for high mass flow rates surpasses the Cierzo circulator [79] capacity. Thus, all calculations are conducted with the Noordenwind circulator [79] and at 20 bar in order to enable a comparison.

Table 7.1: *Comparison of temperatures at multiple locations of various layouts (sequences) of the cooling system. The first sequence is assumed to be the default and the distinctive positions of the respective sequence to be examined are highlighted with bold text. See Figure 6.1 for clarification. The temperatures are obtained for a system consisting of a single PT420 cryocooler [78], a Cierzo circulator [79], a first stage HEX length of* 2 m*, and a second stage HEX length of* 2 m *for a nominal pressure of* 20 bar *and a mass flow rate of* 0.5 g/s*.*

Sequence of components	T CM in (K)	T CM out (K)	T IVC out (K)	T TS in (K)	T TS out (K)
1st stage→CFHX→2nd stage→ CM→IVC→CFHX→TS→Circulator*	6.1	6.6	6.8	32.5	43.7
1st stage→CFHX→2nd stage→ **IVC→CM**→CFHX→TS→Circulator	6.3	6.8	6.3	32.5	43.7
1st stage→CFHX→2nd stage→ CM→IVC→CFHX→**Circulator→TS**	6.2	6.7	6.9	24.7	45.8
1st stage→TS→CFHX→2nd stage→ CM→IVC→CFHX→**Circulator**	7.1	7.5	7.7	35.4	46.6
1st stage→CFHX→**CM→IVC →2nd stage**→CFHX→TS→Circulator	7.5	7.9	8.0	32.5	43.6

* default and optimal layout, depicted in Figure 6.1.

The system with two cryocoolers in series yields the lowest CM outlet temperature, where the parallel layout shows a constant 0.5 K higher temperature across the different mass flow rates. The various mass flow rates enable the estimation of the optimal mass flow rate for the respective cooling system. This, again, depends on the complex relation of cryocooler capacity curve, efficiency of the circulator, and temperature gradients of TS and CM. The system with a single cryocooler demonstrates a pronounced mass flow rate dependency with an optimum temperature of 6.6 K at 0.3 g/s. The CM outlet temperature depends less strongly on the mass flow rate for the systems with two cryocoolers. The simulation diverges for low mass flow rates as the stage temperature of the cryocoolers lies outside the capacity map of Figure G.4. Yet, a minimal temperature is reached for the layout of two cryocoolers in series at 4.6 K and 0.5 g/s. The option of two PT420 cryocoolers [78] in series is chosen as the 2 K lower temperatures compared to a system with a single cryocooler, justify the additional costs. Furthermore, the second cryocooler provides a greater stability against unexpected heat loads and malfunction for the cooling system.

The system layout with two PT420 cryocoolers [78] in series is calculated with different nominal pressures in order to investigate the influence of the pressure on the cooling performance. Figure 7.3 right displays the CM outlet temperature for different mass flow rates as a function of different

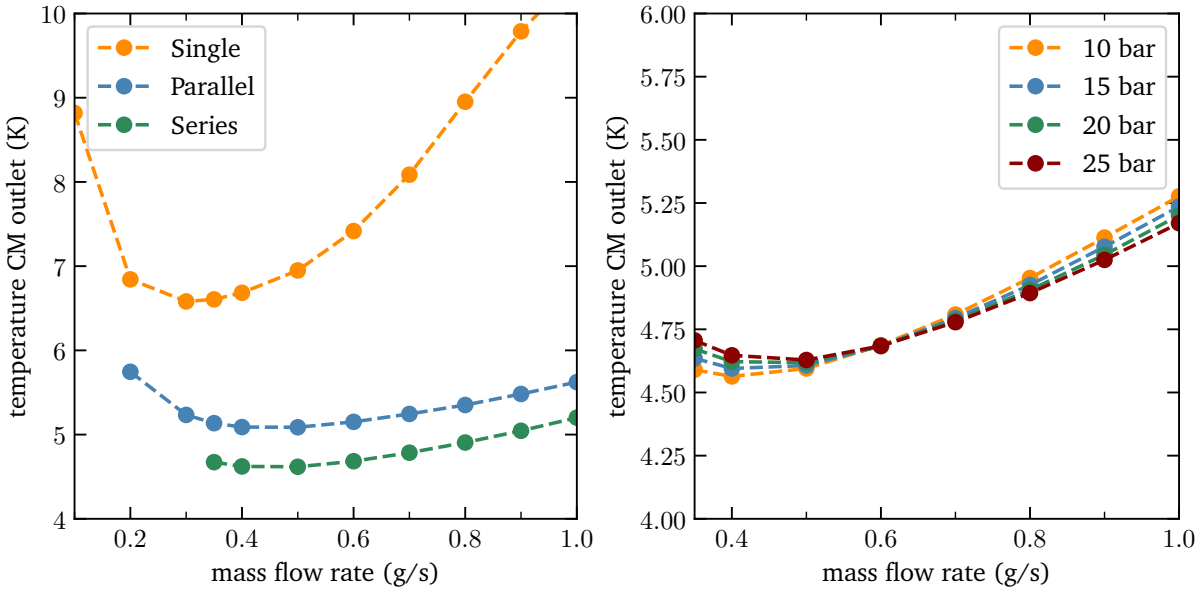

Figure 7.3: *Temperature of the CM outlet at different mass flow rates for a system consisting of a Noordenwind circulator [79], a first stage HEX length of* 2 m*, and a second stage HEX length of* 2 m*. Optimal mass flow rates can be estimated from the minimum of the temperature of the CM outlet. Left: The system layouts of a single PT420 cryocooler [78], two cryocoolers in parallel and two cryocoolers in series are compared for a nominal pressure of* 20 bar*. The stage temperature of the cryocoolers in parallel and in series for low mass flow rates lies outside the capacity map of Figure G.4, i.e., it is too low, and the simulation diverges. Right: Different nominal pressures are compared for the layout of two PT420 cryocoolers [78] in series.*

pressures. No substantial difference in the CM outlet temperature for the compared pressure regimes is evident. The lower the pressure, the lower the CM outlet temperature at lower mass flow rates, and the higher at higher mass flow rates. Interestingly, every pressure regime seems to reach the same CM outlet temperature at 0.6 g/s mass flow rate. Note, however, that due to the different pressures the volumetric flow rate differs vastly for the same mass flow rates. Thus, the cryogenic circulator has to move a substantially higher amount of gas volume at lower pressures to reach the set mass flow rate. This results in a higher pressure head that the Cierzo and also the Noordenwind circulator [79] cannot overcome. Only the systems with 20 bar and 25 bar stay in the regime provided by the Noordenwind circulator [79]. Lower pressure regimes soften the pressure requirements of the equipment. Hence, the Noordenwind circulator [79] and 20 bar nominal pressure are favored for the present cryostat.

Following the optimization of the layout and the components of the system, the above presented options for the cryostat and their influence on the system temperature can be quantified. The installation of the IVC introduces additional heat leaks through the walls of the IVC that the cooling system needs to compensate. According to the model in the above defined layout the temperature

at the CM outlet corresponds to 4.62 K and at the IVC outlet to 4.83 K. Without the IVC these two temperatures equal 4.59 K and 4.77 K, respectively. This negligible difference is expected to be lower than the uncertainty from the model and, thus, there exists no convincing argument from the heat load perspective against the installation of the IVC, which offers the advantage of maintenance of the electronics without full vacuum break. The installation of a cooling rack is estimated to result in 1 K temperature increase of the CM due to the less ideal thermal contact. This would lead to a CM outlet temperature of 5.62 K and an IVC outlet temperatures of 4.83 K. Therefore, it would reverse the temperature difference between these two points which might be advantageous. Finally, the temperature and pressure results from the thermodynamic model in the proposed layout are displayed in Table D.3. There, the numbers refer to the positions according to the sketch in Figure 6.1.

7.3 Proposed layout of the cryostat

The present section aims to summarize the proposed layout of the BabyIAXO-RADES cryostat as result of the above described findings. The cryostat has three distinct temperature levels: room temperature at the VC, intermediate temperature at the TS, and low temperature at the CM and IVC thermalization plate. The TS is made out of 2 mm thick copper and covered by a 30 layer MLI blanket. A 10 layer MLI blanket covers the 5 mm thick cavity or cavities which consist of either copper or copper-coated SST and have a maximum outer diameter of 60 cm, and the IVC thermalization plate (see Section 5.2.2 and Section 5.4.1). The cryostat is supported by scaffolding from the outside to comply with the mechanical load optimization of BabyIAXO. The cryostat is divided into three parts: BabyIAXO bore, transfer line, and service box. Inside the 11 m long, 70 cm diameter bore, a support structure made out of G10 epoxy-fiberglass sustains the TS and the cavities at their defined position and minimizes the heat load due to thermal conduction. Additionally, zirconium oxide ball transfer units enable the insertion of the support structure and the TS into the BabyIAXO bore and the sliding of the cavities on top of the structure (see Section 5.4.1). Two copper coaxial cables are connected to each cavity at two ports. The cavities, the coaxial cables and the tuning mechanism constitute the CM. The tuning mechanism is equipped to accurately turn metallic plates inside the cavities and consists, in the present work, of stepper motors at room temperature, piezoelectric motors at low temperature, and one hollow G10 tuning rod per cavity (see Section 5.4.3). The tuning rod is covered by a single layer of MLI and has a diameter of 12 mm and a thickness of 3 mm. Here, all tuning rods are connected to every cavity at two points (see Section 5.4.3). The 2 m long, 20 cm diameter transfer line extends the vacuum chamber of the bore to protect the auxiliary equipment from the external magnetic field of the BabyIAXO magnet. The tuning rods, the coaxial cables, and the TS are routed through the transfer line (see Figure 4.4). Lastly, the service box hosts all the auxiliary equipment of the cooling system as well as the electrical equipment for RF data taking (see Figure H.10). The service box has a roughly cylindrical geometry with a length of 1 m and a diameter of 60 cm, with four flanges to be attached to the transfer line and to install and maintain the two

systems (RF and cooling system). The thermal shield of the service box is thermalized at the first stage of one cryocooler via copper braids.

The cryocooler and closed helium circulation loop based remote cooling system is used to effectively cool the CM and the TS inside the bore. It consists of two Cryomech® PT420 cryocoolers [78] connected in series, one Stirling Cryogenics® Noordenwind cryogenic circulator [79], one CFHX, specifically produced by the CCCL, and cooling pipes in which supercritical helium is circulated. The remote cooling pipes are made of copper, have an inner diameter of 4 mm, and are brazed onto the TS along its length and either brazed onto the cavities directly or onto a cooling rack around the cavities which transports the heat from the cavities via flexible copper braids (see Section 6.1.4). The use of the cooling rack would improve the flexibility of the cavity design, in addition to avoid the need of brazing cooling pipes on the cavity surface. However, this additional heat transfer would require about 5 cm radial distance, reducing the maximum cavity diameter from 60 cm to 50 cm, thus reducing the cavity volume (compare equation (3.1)). The electrical equipment is cooled by brazing the cooling pipe in a meander of 0.5 m length onto the IVC thermalization plate and thermally attaching the equipment to the plate. The sequence of connection of the components in the cooling system can be seen in the system sketches of Figure 4.4, Figure 6.1, and Figure H.10. The connecting pipes have an inner diameter of 4 mm and are made of copper and SST, respectively. The HEX at the first stage of the cryocoolers has a length of 2 m and an inner diameter of 8 mm and the HEX at the second stage has a length of 2 m and an inner diameter of 4 mm. From the optimizations with the thermodynamic model, the operating conditions of about 0.5 g/s mass flow rate and 20 bar nominal pressure seem optimal.

The electrical equipment consisting of one LNA per cavity, electrical switches, and the calibration system is mounted inside the IVC (see Figure H.10). The IVC is made of 2 mm thick G10 in a meander double structure with an intermediate copper ring for the thermalization with the TS and a 1.5 cm thick copper plate at low temperature (see Figure H.11). The LNAs and the switches are thermally connected to the thermalization plate. The copper coaxial cables coming from the transfer line are attached to the feedthrough of the thermalization plate after being cooled down at the latter. At the other side of the feedthrough SST coaxial cables conduct the signal to the VNA and the LNA/DAQ, respectively. One additional SST coaxial cable per cavity is needed for the calibration of the cavity and connects the calibration system with the VNA. The coaxial cables inside the IVC have a length of about 1 m and are thermalized at the TS by clamps at about 50 % of their length (see Section 5.3). A possible separate vacuum pump may be installed on the outside flange in order to control the vacuum of the IVC.

8 Conclusion and outlook

In this work, a first design of the cryostat for the RADES resonant cavity detector for BabyIAXO is examined. This is done by introducing the BabyIAXO and RADES project and discussing the resulting requirements for the cryostat. The most promising cooling method based on cryocoolers, a cryogenic circulator, and an active circulation loop is selected. The arising heat loads of the components of the cryostat and associated instrumentation are numerically estimated and their design, where possible, optimized. A thermodynamic model of the cooling system is compiled and described, with which the layout of the cooling system is optimized and the operational parameters investigated. Additionally, an experiment imitating the present system is commissioned and conducted at the CCCL, acting as a proof-of-concept. This is the first successful operation of such a cryocooler and circulator based cooling system and valuable insights are obtained and possible improvements identified. The present experiment, however, reveals a substantial background heat load and a susceptibility for TAOs. Therefore, the cooling system reaches its equilibrium at a low temperature regime of about 13 K instead of the envisioned 4 — 10 K. Nevertheless, the remaining data suggest a satisfactory operation of the cryogenic circulator and an acceptable agreement of the temperature levels of the experimental setup with the thermodynamic model, especially for the first stage temperature regime. Future research will have to confirm the effectiveness of the envisioned cooling system and the accuracy of the model. For now the predictions of the thermodynamic model are cautiously trusted. The present study acts as a first step to the design of the cryostat to be installed in BabyIAXO. The design and the thermodynamic model are highly modular and adaptable to support an ever evolving design of the cavity, RF DAQ system, and BabyIAXO haloscope. In addition to the cryostat design, it assists in specifying the layout of the electrical equipment. The model allows to relate the thermal noise temperature of the detection to the costs of installing and operating the cryostat. The predicted CM temperature of about 4.6 K seems competitive and further motivates the operation of the RADES resonant cavity detector in BabyIAXO.

The following subsequent studies are needed to fully design the present cryostat but are beyond the scope of the present work. Once the choice for the coaxial cable to be installed in BabyIAXO has been made, it seems compelling to experimentally investigate the heat leak through the cables, as the fit to the very limited data in the present work is insufficient (see Section 5.3). The final design of the resonant cavity and the tuning system enables the development of the support structure of the cavity and the TS inside the BabyIAXO bore. The influence of a quench of the BabyIAXO magnet on the present system must be investigated in a future study, as this requires future design details. During a quench the inductive coupling between the magnet and the structural elements results in Lorentz

forces acting on these structural components, making an investigation absolutely essential. These effects are also called quench back and more information can be found for example in [127, 128]. The structure of BabyIAXO thermal shield, BabyIAXO vacuum chamber, TS and CM depicts multiple cylindrical objects in a dipole field, each able to shield part of the change of magnetic field during the fast ramp down of the magnet. Thus, it requires 3D electromagnetic and mechanical modeling to determine whether a copper TS and cavity may be used. If a quench possesses damaging potential, the TS and the cavity might need to be sectioned into multiple parts or different materials be used. The BabyIAXO thermal shield is sectioned crosswise (see [129]). Lastly, a BabyIAXO bore mockup as a vacuum testing chamber at DESY should be built to test and construct the cryostat and resonant cavity before inserting the system into the BabyIAXO bore. The highly adaptable and independent cryostat designed in this work allows to install resonant cavities with little effort also at other magnets in cooled and warm bores without requiring cryogenic infrastructure. Additionally, structures other than resonant cavities can easily be cooled in a remote and low-interference manner; the application possibilities are numerous.

References

[1] Iain Nicolson. *Dark Side of the Universe: Dark Matter, Dark Energy, and the Fate of the Cosmos*. JOHNS HOPKINS UNIV PR, 2007. 192 pp. ISBN: 0801885922.

[2] A. De Rújula. *The Dark Side of the Universe*. 2021. URL: https://arxiv.org/abs/2108.01691.

[3] E. Armengaud et al. "Physics potential of the International Axion Observatory (IAXO)". In: *Journal of Cosmology and Astroparticle Physics* 2019.06 (2019), pp. 047–047. DOI: 10.1088/1475-7516/2019/06/047.

[4] Igor G. Irastorza. *An introduction to axions and their detection*. 2021. URL: https://arxiv.org/abs/2109.07376.

[5] E Armengaud et al. "Conceptual design of the International Axion Observatory (IAXO)". In: *Journal of Instrumentation* 9.5 (2014), T05002–T05002. DOI: 10.1088/1748-0221/9/05/t05002.

[6] A. Abeln et al. "Conceptual design of BabyIAXO, the intermediate stage towards the International Axion Observatory". In: *Journal of High Energy Physics* 2021.5 (2021). DOI: 10.1007/jhep05(2021)137.

[7] Alejandro Álvarez Melcón et al. "Axion Searches with Microwave Filters: the RADES project". In: *Journal of Cosmology and Astroparticle Physics* 2018 (2018). DOI: 10.1088/1475-7516/2018/05/040.

[8] J. Golm et al. *Thin Film (High Temperature) Superconducting Radiofrequency Cavities for the Search of Axion Dark Matter*. 2021. URL: https://arxiv.org/abs/2110.01296.

[9] A. Onufrena et al. "Remote cooling systems with mesh-based heat exchangers for cryogenic applications". In: *IOP Conference Series: Materials Science and Engineering, Advances in Cryogenic Engineering*. Unpublished. 2021.

[10] A. Onufrena et al. "Design of a compact mesh-based high-effectiveness counter-flow heat exchanger and its integration in remote cooling systems". In: *International Journal of Heat and Mass Transfer* 183 (2022). Submitted to International Journal of Heat and Mass Transfer, p. 122107. DOI: 10.1016/j.ijheatmasstransfer.2021.122107.

[11] Matic Lubej. *standard-model*. Online. [accessed 08.03.2022]. URL: https://github.com/mlubej/standard-model.

[12] Brian R. Martin and Graham Shaw. *Particle Physics*. 4th ed. Wiley, 2017. 486 pp. ISBN: 1118911903.

[13] Paul Langacker. *The Standard Model and Beyond*. 2nd ed. CRC Press, 2017. DOI: 10.1201/b22175.

[14] CERN. *CERN experiments observe particle consistent with long-sought Higgs boson*. Press release. Online. [accessed 08.03.2022]. 2012. URL: https://home.cern/news/press-release/cern/cern-experiments-observe-particle-consistent-long-sought-higgs-boson.

[15] Kenneth C. Freeman. "On the disks of spiral and S0 galaxies". In: *The Astrophysical Journal* 160 (1970), p. 811.

[16] Vera C. Rubin and W. Kent. Ford Jr. "Rotation of the Andromeda nebula from a spectroscopic survey of emission regions". In: *The Astrophysical Journal* 159 (1970), p. 379.

[17] P. J. E. Peebles and Bharat Ratra. "The cosmological constant and dark energy". In: *Reviews of Modern Physics* 75.2 (2003), pp. 559–606. DOI: 10.1103/revmodphys.75.559.

[18] Philip Bull et al. "Beyond ΛCDM: Problems, solutions, and the road ahead". In: *Physics of the Dark Universe* 12 (2016), pp. 56–99. DOI: 10.1016/j.dark.2016.02.001.

[19] Mariangela Lisanti. "Lectures on Dark Matter Physics". In: *New Frontiers in Fields and Strings*. 2016. DOI: 10.1142/9789813149441_0007.

[20] Kim Griest. "Galactic microlensing as a method of detecting massive compact halo objects". In: *The Astrophysical Journal* 366 (1991), pp. 412–421.

[21] Timothy D. Brandt. "CONSTRAINTS ON MACHO DARK MATTER FROM COMPACT STELLAR SYSTEMS IN ULTRA-FAINT DWARF GALAXIES". In: *The Astrophysical Journal Letters* 824.2 (2016), p. L31. DOI: 10.3847/2041-8205/824/2/l31.

[22] Giorgio Arcadi et al. "The waning of the WIMP? A review of models, searches, and constraints". In: *The European Physical Journal C* 78.3 (2018), pp. 1–57. DOI: 10.1140/epjc/s10052-018-5662-y.

[23] T. Kaluza. "Zum Unitätsproblem der Physik". In: *Sitzungsber. Königl. Preuss. Akad. Wiss.* (1921), pp. 966–972.

[24] Oskar Klein. "Quantentheorie und fünfdimensionale Relativitätstheorie". In: *Zeitschrift fuer Physik* 37.12 (1926), pp. 895–906. DOI: 10.1007/bf01397481.

[25] J. H. Christenson et al. "Evidence for the 2π Decay of the K_2^0 Meson". In: *Physical Review Letters* 13.4 (1964), pp. 138–140. DOI: 10.1103/physrevlett.13.138.

[26] R. D. Peccei and Helen R. Quinn. "*CP* Conservation in the Presence of Pseudoparticles". In: *Physical Review Letters* 38.25 (1977), pp. 1440–1443. DOI: 10.1103/physrevlett.38.1440.

[27] R. D. Peccei and Helen R. Quinn. “Constraints imposed by *CP* conservation in the presence of pseudoparticles”. In: *Physical Review D* 16.6 (1977), pp. 1791–1797. DOI: 10.1103/physrevd.16.1791.

[28] Steven Weinberg. “A New Light Boson?” In: *Physical Review Letters* 40.4 (1978), pp. 223–226. DOI: 10.1103/physrevlett.40.223.

[29] F. Wilczek. “Problem of Strong P and T Invariance in the Presence of Instantons”. In: *Physical Review Letters* 40.5 (1978), pp. 279–282. DOI: 10.1103/physrevlett.40.279.

[30] Frank Wilczek. *Time’s (Almost) Reversible Arrow*. Quanta Magazine. Online. [accessed 08.03.-2022]. 2016. URL: https://www.quantamagazine.org/how-axions-may-explain-times-arrow-20160107/.

[31] Jihn E. Kim. “Weak-Interaction Singlet and Strong *CP* Invariance”. In: *Physical Review Letters* 43.2 (1979), pp. 103–107. DOI: 10.1103/physrevlett.43.103.

[32] M. A. Shifman et al. “Can confinement ensure natural *CP* invariance of strong interactions?” In: *Nucelar Physics B* 166.3 (1980), pp. 493–506. DOI: 10.1016/0550-3213(80)90209-6.

[33] Michael Dine et al. “A simple solution to the strong *CP* problem with a harmless axion”. In: *Physics Letters B* 104.3 (1981), pp. 199–202. DOI: 10.1016/0370-2693(81)90590-6.

[34] A. R. Zhitnitskij. “On possible suppression of the axion-hadron interactions”. In: *Yadernaya Fizika* 31.2 (1980), pp. 497–504.

[35] Igor G. Irastorza and Javier Redondo. “New experimental approaches in the search for axion-like particles”. In: *Progress in Particle and Nuclear Physics* 102 (2018), pp. 89–159. DOI: 10.1016/j.ppnp.2018.05.003.

[36] Luca Di Luzio et al. “The landscape of QCD axion models”. In: *Physics Reports* 870 (2020), pp. 1–117. DOI: 10.1016/j.physrep.2020.06.002.

[37] H. Primakoff. “Photo-Production of Neutral Mesons in Nuclear Electric Fields and the Mean Life of the Neutral Meson”. In: *Physical Review* 81.5 (1951), pp. 899–899. DOI: 10.1103/physrev.81.899.

[38] P. Sikivie. “Experimental Tests of the "Invisible" Axion”. In: *Physical Review Letters* 51.16 (1983), pp. 1415–1417. DOI: 10.1103/physrevlett.51.1415.

[39] C. O’Hare. *AxionLimits*. Online. [accessed 08.03.2022]. URL: https://github.com/cajohare/AxionLimits.

[40] Javier Redondo. “Solar axion flux from the axion-electron coupling”. In: *Journal of Cosmology and Astroparticle Physics* 2013.12 (2013), pp. 008–008. DOI: 10.1088/1475-7516/2013/12/008.

[41] Klaus Ehret et al. “New ALPS results on hidden-sector lightweights”. In: *Physics Letters B* 689.4-5 (2010), pp. 149–155. DOI: 10.1016/j.physletb.2010.04.066.

[42] R Bähre et al. “Any light particle search II — Technical Design Report”. In: *Journal of Instrumentation* 8.09 (2013), T09001. DOI: 10.1088/1748-0221/8/09/t09001.

[43] K. Zioutas et al. “First Results from the CERN Axion Solar Telescope”. In: *Physical Review Letters* 94.12 (2005), p. 121301. DOI: 10.1103/physrevlett.94.121301.

[44] M. Arik et al. “Search for Sub-eV Mass Solar Axions by the CERN Axion Solar Telescope withHe3Buffer Gas”. In: *Physical Review Letters* 107.26 (2011), p. 261302. DOI: 10.1103/physrevlett.107.261302.

[45] S. J. Asztalos et al. “SQUID-Based Microwave Cavity Search for Dark-Matter Axions”. In: *Physical Review Letters* 104.4 (2010), p. 041301. DOI: 10.1103/physrevlett.104.041301.

[46] R. Khatiwada et al. *Axion Dark Matter eXperiment: Detailed Design and Operations*. 2020. URL: https://arxiv.org/abs/2010.00169.

[47] Alexander J. Millar et al. “Dielectric haloscopes to search for axion dark matter: theoretical foundations”. In: *Journal of Cosmology and Astroparticle Physics* 2017.01 (2017), pp. 061–061. DOI: 10.1088/1475-7516/2017/01/061.

[48] Allen Caldwell et al. “Dielectric Haloscopes: A New Way to Detect Axion Dark Matter”. In: *Physical Review Letters* 118.9 (2017), p. 091801. DOI: 10.1103/physrevlett.118.091801.

[49] P. Brun et al. “A new experimental approach to probe QCD axion dark matter in the mass range above 40 μeV”. In: *The European Physical Journal C* 79.3 (2019). DOI: 10.1140/epjc/s10052-019-6683-x.

[50] I.G Irastorza et al. “Towards a new generation axion helioscope”. In: *Journal of Cosmology and Astroparticle Physics* 2011.06 (2011), pp. 013–013. DOI: 10.1088/1475-7516/2011/06/013.

[51] Alejandro Díaz-Morcillo et al. “Design of New Resonant Haloscopes in the Search for the Dark Matter Axion: A Review of the First Steps in the RADES Collaboration”. In: *Universe* 8.1 (2021), p. 5. DOI: 10.3390/universe8010005.

[52] A. Álvarez Melcón et al. *Scalable haloscopes for axion dark matter detection in the 30 μeV range with RADES*. 2020. URL: https://arxiv.org/abs/2002.07639.

[53] P. Navarro et al. *Wide-band full-wave electromagnetic modal analysis of the coupling between dark-matter axions and photons in microwave resonators*. 2021. URL: https://arxiv.org/abs/2107.03137.

[54] A. Álvarez Melcón et al. “First results of the CAST-RADES haloscope search for axions at 34.67 μeV”. In: *Journal of High Energy Physics* 2021.10 (2021), pp. 1–16. DOI: 10.1007/JHEP10(2021)075.

[55] Sergio Arguedas Cuendis. “Dark Matter Axion Search Using Novel RF Resonant Cavity Geometries in the CAST Experiment”. Unpublished. PhD thesis. Universität Wien, 2021.

[56] Steven W. Van Sciver. *Helium Cryogenics*. Springer New York, 2012. DOI: 10.1007/978-1-4419-9979-5.

[57] N. H. Balshaw. *Practical cryogenics : an introduction to laboratory cryogenics*. Oxford Instruments, Scientific Research Division, 1996. ISBN: 0952759403.

[58] CERN. *Cryogenics: Low temperatures, high performance*. Online. [accessed 08.03.2022]. URL: https://home.cern/science/engineering/cryogenics-low-temperatures-high-performance.

[59] Nikolay Bykovskiy et al. "Design of the BabyIAXO Superconducting Detector Magnet". In: *IEEE Transactions on Applied Superconductivity* 30.4 (2020), pp. 1–5. DOI: 10.1109/tasc.2020.2988308.

[60] Nikolay Bykovskiy et al. "Superconducting Detector Magnet for BabyIAXO". In: *IEEE Transactions on Applied Superconductivity* 31.5 (2021), pp. 1–5. DOI: 10.1109/tasc.2021.3059603.

[61] H F P Silva et al. "Thermal analysis and cryogenics of the Baby-IAXO magnet". In: *IOP Conference Series: Materials Science and Engineering* 755 (2020), p. 012132. DOI: 10.1088/1757-899x/755/1/012132.

[62] A. Dudarev et al. *11th General IAXO Collaboration Meeting: BabyIAXO Magnet Design and R&D update*. 2020. URL: https://indico.cern.ch/event/877783/.

[63] Dassault Systèmes. *CST Studio Suite: Electromagnetic field simulation software*. Online. [accessed 08.03.2022]. URL: https://www.3ds.com/products-services/simulia/products/%20cst-studio-suite/.

[64] B. Walker. *Cryocoolers: Part 1: Fundamentals*. Plenum Press, 1983.

[65] Milind D. Atrey. *Cryocoolers: theory and applications*. Ed. by Milind D. Atrey. Springer International Publishing, 2020. DOI: 10.1007/978-3-030-11307-0.

[66] T. Trollier et al. "30 K to subK vibration free remote cooling systems". In: *22nd Cryogenic Engineering Conference and International Cryogenic Materials Conference*. 2019.

[67] A.P. Rijpma et al. "Construction and tests of a heart scanner based on superconducting sensors cooled by small stirling cryocoolers". In: *Cryogenics* 40.12 (2020), pp. 821–828. DOI: 10.1016/s0011-2275(01)00036-4.

[68] Neil Stilin et al. *Stable CW Operation of Nb_3Sn SRF Cavity at 10 MV/m using Conduction Cooling*. 2020. URL: https://arxiv.org/abs/2002.11755.

[69] Y. Wu et al. "Vibration-free Cooler for the METIS Instrument Using Sorption Compressors". In: *Physics Procedia* 67 (2015), pp. 411–416. DOI: 10.1016/j.phpro.2015.06.050.

[70] J. Tanchon et al. "A 40 K Turbo-Brayton Cryocooler forEarth Observation Applications". In: *Cryocoolers 20*. 2018.

[71] T. Trollier et al. “Remote helium cooling loops for laboratory applications”. In: *Cryocoolers 17*. 2012.

[72] D. Plachta et al. “NASA cryocooler technology developments and goals to achieve zero boil-off and to liquefy cryogenic propellants for space exploration”. In: *Cryogenics* 94 (2018), pp. 95–102. DOI: 10.1016/j.cryogenics.2018.07.005.

[73] Miguel Fernandes et al. “Optimized Cryogenic Current Comparator for CERN’s Low-Energy Antiproton Facilities”. In: *5th International Beam Instrumentation Conference*. Vol. IBIC2016. 2017. DOI: 10.18429/JACOW-IBIC2016-MOPG48.

[74] A.P. Rijpma et al. “Construction and test of a cryocooler-cooled low-Tc SQUID gradiometer system”. In: *Cryogenics* 48.1-2 (2008), pp. 61–67. DOI: 10.1016/j.cryogenics.2007.11.004.

[75] Kentaro Somiya. “Detector configuration of KAGRA–the Japanese cryogenic gravitational-wave detector”. In: *Classical and Quantum Gravity* 29.12 (2012), p. 124007. DOI: 10.1088/0264-9381/29/12/124007.

[76] A. Onufrena et al. “Cryogenic Performance of a Compact High-Effectiveness Mesh Counter-Flow Heat Exchanger”. Unpublished. 2021.

[77] A. Onufrena et al. “Characterization of Woven Copper Mesh as a Heat Transfer Matrix at Low Temperatures”. In: *International Cryocooler Conference, Cryocoolers 21*. 2021.

[78] Cryomech. *PT420 CRYOCOOLERS*. Online. [accessed 08.03.2022]. URL: https://www.cryomech.com/products/pt420/.

[79] Stirling Cryogenics BV. Online. [accessed 08.03.2022]. https://www.stirlingcryogenics.eu/.

[80] *VDI-Wärmeatlas*. Springer Berlin Heidelberg, 2013. DOI: 10.1007/978-3-642-19981-3.

[81] Jack Ekin. *Experimental Techniques for Low Temperature Measurements*. Oxford University Press, 2006. 560 pp. ISBN: 0198570546.

[82] Steffen Grohmann. *Cryogenic Engineering*. Institute of Technical Thermodynamics and Refrigeration, Karlsruhe Insitute of Technology. Lecture. Winter term 2020/21.

[83] V. Parma. “Cryostat Design”. In: *CAS - CERN Accelerator School: Superconductivity for Accelerators* (2014), pp. 353–399. DOI: 10.5170/CERN-2014-005.353.

[84] S. L. Bapat et al. “Experimental investigations of multilayer insulation”. In: *Cryogenics* 30.8 (1990), pp. 711–719. DOI: 10.1016/0011-2275(90)90235-5.

[85] James E. Fesmire and Stan D. Augustynowicz. “Cryogenic thermal insulation systems”. In: *16th Thermal and Fluids Analysis Workshop*. 2005.

[86] M. Donabedian et al. “Insulation”. In: *Spacecraft thermal control handbook* 1 (2002), pp. 161–205.

[87] Russel B. Scott. *Cryogenic engineering*. 11th ed. Van Nostrand, 1959. 368 pp.

[88] Valentina Venturi. "Thermodynamic and technological optimization of complex cryogenic insulation systems". PhD thesis. Politechnika Wrocławska, 2019.

[89] E. M. W. Leung et al. "Techniques for Reducing Radiation Heat Transfer between 77 and 4.2 K". In: *Advances in Cryogenic Engineering*. 1980, pp. 489–499. DOI: 10.1007/978-1-4613-9856-1_59.

[90] W. Lehmann. "Superisolation (SI)-deren Qualitat und Degradierung bei Anwendungen in der Kryotechnik". In: *DKV TAGUNGSBERICHT* 27.1 (2000), pp. 99–108.

[91] Ted C. Nast. "A review of multilayer insulation, theory, calorimeter measurements, and applications". In: *ASME-PUBLICATIONS-HTD* 267 (1993), pp. 29–29.

[92] James E. Fesmire. "Standardization in Cryogenic Insulation Systems Testing and Performance Data". In: *Physics Procedia* 67 (2015), pp. 1089–1097. DOI: 10.1016/j.phpro.2015.06.205.

[93] ASTM International. *Standard Guide for Thermal Performance Testing of Cryogenic Insulation Systems, ASTM C1774*. 2013.

[94] V. Venturi et al. "Experimental measurements on MLI performance from 20-60 K to 4.2 K". In: *IOP Conference Series: Materials Science and Engineering* 755 (2020), p. 012154. DOI: 10.1088/1757-899x/755/1/012154.

[95] S .L. Bapat et al. "Performance prediction of multilayer insulation". In: *Cryogenics* 30.8 (1990), pp. 700–710. DOI: 10.1016/0011-2275(90)90234-4.

[96] Germana Riddone. "Theoretical modeling and experimental investigation of the thermal performance of the LHC prototype lattice cryostats". PhD thesis. CERN, 1997.

[97] Michael A Green. *Cooling the MICE Liquid Hydrogen Absorbers using Small Cryogenic Coolers*. Tech. rep. MICE Note 108, 2004.

[98] H. Neumann et al. "Influence of tailored MLI for complex surface geometries on heat transfer". In: *IOP Conference Series: Materials Science and Engineering* 101 (2015), p. 012013. DOI: 10.1088/1757-899x/101/1/012013.

[99] Robert Richardson and Eric Smith. *Experimental techniques in condensed matter physics at low temperatures*. Addison-Wesley Pub. Co, 1988. ISBN: 0201150026.

[100] QAXIAL. *Semi-rigid coaxial cable, RG402-CU*. Online. [accessed 08.03.2022]. URL: https://www.rf-microwave.com/en/qaxial/rg402-cu/semi-rigid-coaxial-cable/rg402-cu/.

[101] KEYCOM. *Semi-Rigid Cables for Cryogenic (Super Low Temperature) Applications, ULT-05*. Online. [accessed 08.03.2022]. URL: https://www.keycom.co.jp/eproducts/upj/upj2/page.htm.

[102] National Institute of Standards and Technology (NIST). *Properties of solid materials from cryogenic toroom temperatures*. Online. [accessed 08.03.2022]. URL: https://trc.nist.gov/cryogenics/materials/materialproperties.htm.

[103] Eckels Engineering and Cryodata Inc. *Cryocomp Software*.

[104] Lake Shore Cryotronics, Inc. *Appendix I: Cryogenic Reference Tables*. Online. [accessed 08.03.2022]. URL: https://www.lakeshore.com/docs/default-source/product-downloads/literature/lstc_appendixi_l.pdf?sfvrsn=5f2ab85b_4.

[105] E Gmelin et al. "Thermal boundary resistance of mechanical contacts between solids at sub-ambient temperatures". In: *Journal of Physics D: Applied Physics* 32.6 (1999), R19.

[106] R. Berman. "Some Experiments on Thermal Contact at Low Temperatures". In: *Journal of Applied Physics* 27.4 (1956), pp. 318–323. DOI: 10.1063/1.1722369.

[107] M. Satter and T. Ashworth. "An investigation of thermal contact resistance in thermal conductivity measurements of a thin nylon sample". In: *Thermal Conductivity 18*. 1985.

[108] L.J. Salerno et al. "Thermal conductance of pressed metallic contacts augmented with indium foil or Apiezon grease at liquid helium temperatures". In: *Cryogenics* 34.8 (1994), pp. 649–654. DOI: 10.1016/0011-2275(94)90142-2.

[109] Curbell Plastics. *G10/FR-4 Glass Epoxy Properties*. Online. [accessed 08.03.2022]. URL: https://rb.gy/eorffd.

[110] Alwayse Engineering. *Ball Transfer Unit: EURO 0 UNITS*. Online. [accessed 08.03.2022]. URL: https://www.alwayse.co.uk/515-0-euro-units.html.

[111] Joanna Liberadzka-Porret. *Thermal Conductivity of Stainless Steel and Zirconium Oxide Ball Transfer Unitsunder Compression Force for the PUMA Project*. Tech. rep. https://edms.cern.ch/document/2443998/3. CERN, 2021.

[112] Association Francaise du Froid. *Cryogenie*. 2019. ISBN: 978-2-37620-356-8.

[113] ANSYS. *Ansys 2020 R2 Workbench*. Online. [accessed 08.03.2022]. URL: https://www.ansys.com/products/ansys-workbench.

[114] P. Duthil. "Material Properties at Low Temperature". In: *CAS - CERN Accelerator School: Superconductivity for Accelerators*. 2014. DOI: 10.5170/CERN-2014-005.77.

[115] Low Noise Factory. *LNF-LNC4-16B*. Online. [accessed 08.03.2022]. URL: https://www.lownoisefactory.com/products/cryogenic/4-16-ghz/.

[116] HUBER+SUHNER. *65-SMA-50-0-1/111-NE*. Mouser Electronics. Online. [accessed 08.03.2022]. URL: https://eu.mouser.com/ProductDetail/HUBER%20SUHNER/65_SMA-50-0-1-111_NE?qs=sGAEpiMZZMvShe%2BZiYheiji7VlHbjK/qoJKv1BnP1hw=.

[117] Lennard Niclas Busch. "Heat Transfer Studies of Cryogel® Z under Mechanical Pressure for Large-Scale Insulation of Particle Detectors". https://cds.cern.ch/record/2718621?ln=en. MA thesis. Karlsruhe Institute of Technology, 2019.

[118] Boyan Naydenov. “Development of a Cryocooler-based Remote Cooling System at Low Temperature”. Unpublished. MA thesis. Institut supérieur de l’aéronautique et de l’espace, 2020.

[119] SciPy. *CloughTocher2DInterpolator*. Online. [accessed 08.03.2022]. URL: https://rb.gy/1xqal8.

[120] Horizon Technologies. *HEPAK Software*. Online. [accessed 08.03.2022]. URL: https://htess.com/hepak/.

[121] V. Arp. “Forced Flow, Single-Phase Helium Cooling Systems”. In: *Advances in Cryogenic Engineering*. 1972, pp. 342–351. DOI: 10.1007/978-1-4684-7826-6_38.

[122] J. W. Dean et al. “Temperature Profiles in a Long Gaseous-Helium-Cooled Tube”. In: *Advances in Cryogenic Engineering*. 1978, pp. 250–254. DOI: 10.1007/978-1-4613-4039-3_31.

[123] William Morrow Kays and Alexander Louis London. *Compact heat exchangers*. McGraw-Hill, New York, NY, 1984.

[124] K. W. Taconis et al. “Measurements concerning the vapour-liquid equilibrum of solutions of He3 in He4 below 2.19K”. In: *Physica* 15.8-9 (1949), pp. 733–739. DOI: 10.1016/0031-8914(49)90078-6.

[125] Nikolaus Rott. “Damped and thermally driven acoustic oscillations in wide and narrow tubes”. In: *Zeitschrift für angewandte Mathematik und Physik ZAMP* 20.2 (1969), pp. 230–243. DOI: 10.1007/bf01595562.

[126] Youfan Gu and Klaus D. Timmerhaus. “Experimental Verification of Stability Characteristics for Thermal Acoustic Oscillations in a Liquid Helium System”. In: *Advances in Cryogenic Engineering*. 1994, pp. 1733–1740. DOI: 10.1007/978-1-4615-2522-6_212.

[127] M. A. Green. “Quench back in thin superconducting solenoid magnets”. In: *Cryogenics* 24.1 (1984), pp. 3–10. DOI: 10.1016/0011-2275(84)90049-3.

[128] F. Sonnemann and R. Schmidt. “Quench simulations for superconducting elements in the LHC accelerator”. In: *Cryogenics* 40.8-10 (2000), pp. 519–529. DOI: 10.1016/s0011-2275(01)00008-x.

[129] A. Dudarev et al. *13th General IAXO Collaboration Meeting: BabyIAXO Magnet Design and R&D update*. 2021. URL: https://indico.cern.ch/event/1011471/.

[130] National Instruments. *Fundamentals, System Design, and Setup for the 4 to 20 mA Current Loop*. Online. [accessed 08.03.2022]. 2019. URL: https://www.ni.com/en-us/innovat%5C-ions/white-papers/08/fundamentals--system-design--and-setup-for-the-4-to-20-ma-curren.html.

[131] Innovative Sensor Technology. *Application Note RTD Platinum Sensor*. Online. [accessed 08.-03.2022]. URL: https://www.ist-ag.com/en/downloads.

[132] Temati. *CCS Carbon Ceramic Sensors*. Online. [accessed 08.03.2022]. URL: https://www.temati-uk.com/site/ccs-sensors.html.

[133] International Electrotechnical Commission. *IEC 60751: Industrial platinum resistance thermometers and platinum temperature sensors*. 2008.

[134] Lake Shore Cryotronics. *Temperature Sensor Information*. Online. [accessed 08.03.2022]. URL: https://www.lakeshore.com/resources/sensors.

[135] WIKA. *Model S-10 high-quality pressure transmitter*. Online. [accessed 08.03.2022]. URL: https://www.wika.com/en-en/s_10.WIKA.

[136] Emerson. *Rosemount 3051 Coplanar Pressure Transmitter*. Online. [accessed 08.03.2022]. URL: https://www.emerson.com/en-gb/catalog/rosemount-3051-coplanar-pressure-transmitter-it-it.

[137] ADCMT. *DC Voltage Current Source 6146 / 6156*. Online. [accessed 08.03.2022]. URL: https://www.adcmt.com/en/products/vig/6146.

[138] National Instruments. *PXI-6289 PXI Multifunction I/O Module*. Online. [accessed 08.03.2022]. URL: https://www.ni.com/en-us/support/model.pxi-6289.html.

[139] Lake Shore Cryotronics. *Product Information Obsolete Documentation*. Online. [accessed 08.03.2022]. URL: https://www.lakeshore.com/resources/product-information.

[140] Tektronix. *Keithley 2700 Multimeter/Data Acquisition/Switch Systems*. Online. [accessed 08.03.2022]. URL: https://www.tek.com/en/products/keithley/switching-and-data-acquisition-systems/2700-multimeter-data-acquisition-switch-system.

[141] Tektronix. *Keithley Model 2000 6 1/2-Digit Multimeter Specifications*. Online. [accessed 08.03.2022]. URL: https://www.tek.com/en/documents/specification/keithley-model-2000-6-1-2-digit-multimeter-specifications.

[142] Rohde & Schwarz. *DC Power supplies*. Online. [accessed 08.03.2022]. URL: https://www.rohde-schwarz.com/ch/produkte/messtechnik/dc-netzgeraete_64067.html.

[143] National Instruments. *PXI-6224 PXI Multifunction I/O Module*. Online. [accessed 08.03.2022]. URL: https://www.ni.com/en-us/support/model.pxi-6224.html.

[144] BIPM, IEC, IFCC, ILAC, ISO, IUPAC, IUPAP and OIML. *JCGM 100:2008 Evaluation of measurement data — Guide to the expression of uncertainty in measurement*. Online. [accessed 08.03.2022]. 2008. URL: https://www.bipm.org/en/committees/jc/jcgm/publications.

Appendix

A List of Figures

B List of Tables

C Cooling methods

Table C.1: *First half. Advantages and drawbacks of the different considered cooling methods.*

Conduction cooling		Convection of He inside cavity	
Advantage	Drawback	Advantage	Drawback
• No cooling fluid needed • No safety equipment needed	• Large temperature gradients • Additional structures for heat transport needed • Low flexibility for the cavity: shape, material, thickness, tuning mechanism • Strong exported vibrations	• Good usage of the space • No structure or vessel around cavity • Helium does not worsen the experimental sensitivity	• Need of transfer pipes • Complex system for multiple cavities • Great effort for creating an even flow in the cavity • Cavity cannot be opened for tuning or have any openings • Tuning mechanism needs to be leak tight • Low flexibility for the cavity: shape, tuning mechanism

Table C.2: *Second half. Advantages and drawbacks of the different considered cooling methods.*

Helium bath (vapor / liquid)		Remote cooling via pipes	
Advantage	Drawback	Advantage	Drawback
• Highest flexibility for the cavity (simply submerging) • Easy temperature control • Relatively easy to dimension • Good thermal stability	• Complex system • Large amount of helium needed • Very expensive (due to the helium and the helium infrastructure) • Less space because of the amount of auxiliary equipment needed • Additional pressure vessel and connections around the cavity needed • Large thickness of the vessel required due to the pressure difference to vacuum • Additional safety equipment and big evacuation lines needed • Heavy system • Large transfer lines and therefore a bigger heat load	• Good usage of the space, only cooling pipes around the cavity • Small amount of cooling fluid in the system • Few vibrations in the system • Easier handling than with liquid helium • Lightweight solution • Cost-effective solution	• Need of an effective heat exchanger to reach satisfactory low temperatures • Requires effort to create the thermal contact to the cavity • More complicated system (Cryogenic circulator, heat exchanger) • Requires effort to reach small temperature gradients in the structure

D Thermodynamic model

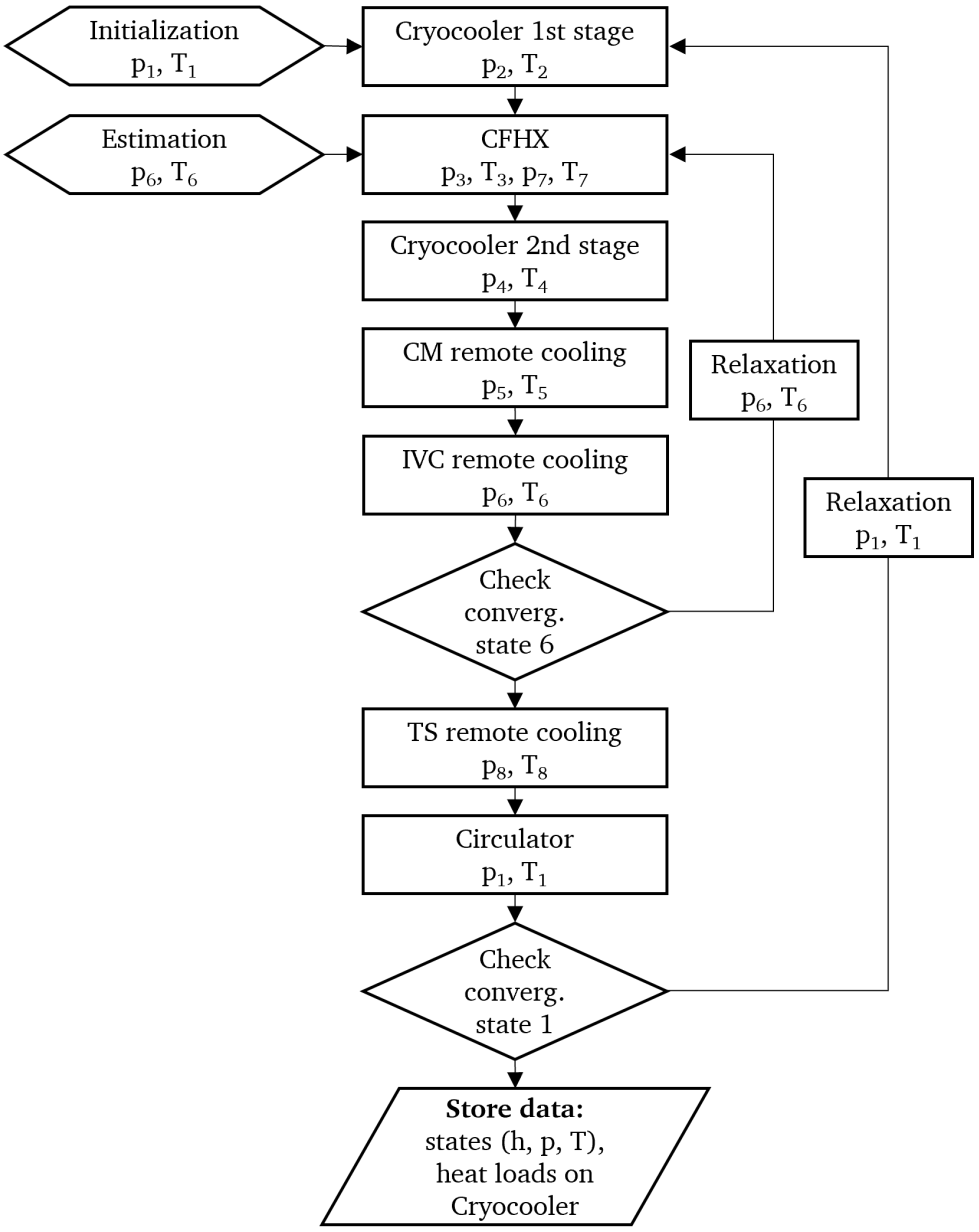

Figure D.1: *Flowchart of the thermodynamic model. The components of the system are structured into functions, which are depicted as rectangles. The first line in the rectangle describes the function and the second line specifies the output of the function. The numbers refer to the locations in Figure 6.1.*

Table D.3: *Temperatures and pressures at multiple locations in system, as results from the thermodynamic model. The numbers refer to the locations according to the sketch of Figure 6.1. The results are valid for a system consisting of two PT420 cryocoolers [78] connected in series, a Noordenwind circulator [79], a first stage HEX length of* 2 m*, and a second stage HEX length of* 2 m *for a nominal pressure of* 20 bar *and a mass flow rate of* 0.5 g/s*.*

Location	Temperature (K)	Pressure (Pa)
1 (after circulator)	40.55	2 000 000
2 (after first stage HEXs)	25.41	1 999 970
3 (after CFHX HP side)	6.11	1 999 954
4 (after second stage HEXs)	3.90	1 999 802
5 (after CM cooling)	4.62	1 999 475
6 (after IVC cooling)	4.83	1 999 461
7 (after CFHX LP side)	24.68	1 999 444
8 (after TS cooling)	35.50	1 996 082

E Measurement and measurement uncertainty calculation

When measuring the resistance of a component by supplying a precise electrical DC current and recording the resulting voltage with a voltmeter, the resistance of the wires and connections between the component and the voltmeter are included in the measurement. These parasitic resistances have a substantial influence on the measurement for small resistances of the component and high wire resistances due to many connections and high electrical resistivity of the wire material (e.g., manganin). Additionally, the resistance of the wire itself changes with the established temperature gradient. The four-wire measurement arrangement practically eliminates the influence of the parasitic resistances by relying on a second pair of wires as shown in Figure E.2 left. A current source provides a substantial current I_I, which is determined by an ammeter and flows through the wires with resistance $R_\mathrm{wire,I}$ and the component with resistance R_sensor, generating a certain voltage drop across the component. The second pair of wires is connected to the component and the voltmeter, which measures the voltage difference resulting from the resistances $R_\mathrm{wire,V}$, and R_sensor and the current I_V. The inner resistance of the voltmeter is high (typically much higher than 1 MΩ) and, thus, I_V is negligible compared to I_I. Therefore, the voltage drop across $R_\mathrm{wire,V}$ is minuscule and the voltmeter effectively only captures the difference of voltage generated at the component. Combining the measurement results of ammeter and voltmeter allows to determine the resistance of the component via Ohm's law. In the present setup this measuring principle is applied to accurately capture the resistance of the RTDs as well as the resistance of the electric heaters.

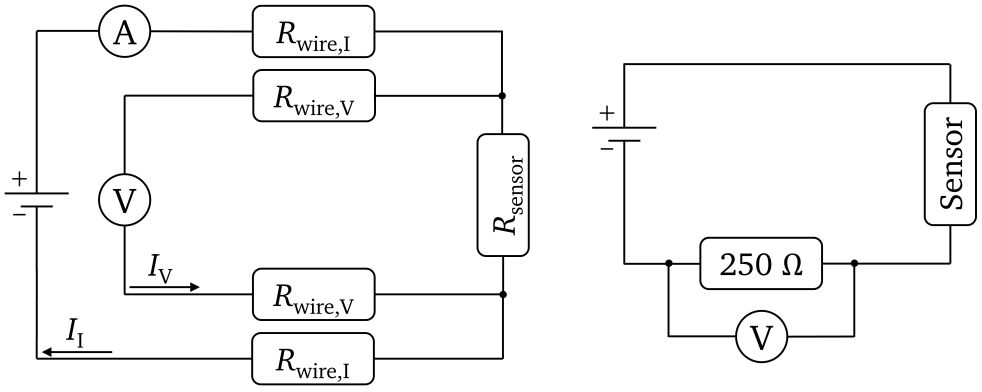

Figure E.2: *Sketch of the electric circuit for a four-wire measurement (left) and for the conversion of a signal of the sensor from current to voltage (right).*

The installed pressure sensors (PT850, PDT801, PDT802 in Figure 6.5) transmit their measuring signal as a current of 4—20 mA as is standard in industry [130]. Such current loop allows to differentiate a live zero signal from a failure in the system [130]. Though many benefits stem from this practice, the current signal needs to be converted into a voltage signal to be recorded in the present setup by the DAQ system. For this purpose high precision resistors of 250 Ω intercept the wire carrying the signal as shown in Figure E.2 right. This additional resistor does not interfere with

the operation of the sensor and allows to determine the voltage drop across it with a voltmeter. The wires connecting the voltmeter to the current loop consist of copper and their inherent resistance can be neglected in relation to the resistor. The described layout thus converts the current signal of 4 −20 mA to a voltage signal of 1 −5 V following Ohm's law.

The Pt100 sensors are classified as class Y [131] (which tolerance corresponds to 1/3 of class B) and the TVO RTDs are TMi Carbon Ceramic Sensors™type A2 [132]. According to the standard IEC 60751 [133] Pt100 sensors are interchangeable above 70 K, thus matching a standard curve with a certain precision [134]. The permissible deviation of the un-calibrated sensor then corresponds to the separated classes of Pt100 sensors [134]. The absolute precision of the sensors below 70 K is extrapolated to the 50 K range. The main interest for the mass flow rate evaluation is the direct offset between two Pt100 sensors due to the heating of the flow. Therefore, all Pt100 sensors have been submerged in liquid nitrogen at the same time to identify the sensors with a similar response curve and match the sensors to their application. An additional in-situ offset adjustment of the Pt100 sensors for the mass flow rate measurement allows for minimum measurement uncertainty, as described below in equation 8.4. The TVO sensors are individually calibrated. The absolute pressure is determined by a WIKA® Model S-10 pressure transmitter [135] and the differential pressure is assessed by two Emerson® Rosemount™3051 Coplanar™pressure transmitters [136]. The Pt100 and TVO RTDs are supplied with 1 mA and 10 µA, respectively, by ADCMT® 6156 DC current sources [137] and the resulting voltage is recorded by two National Instruments® PXI-6289 M Series DAQ modules [138]. The first stage of the cryocooler is regulated by a Lake Shore Cryotronics® 330 PID controller [139] which is connected to a Pt100 sensor and an electric heater mounted on the first stage. The four-wire measurement voltage drop across the electric heater is assessed by a Keithley® 2700 multimeter [140]. Analogously, the second stage of the cryocooler is regulated by a Lake Shore Cryotronics® 331 PID controller [139], a TVO sensor, an electric heater, and a Keithley® 2000 multimeter [141]. A Rohde & Schwarz® HMP4040 DC power supply [142] was used to supply current and read the resulting voltage for both the electric heater for the mass flow rate measurement and the one in the cavity mockup. The signal of the pressure sensors and the circulator are recorded with a National Instruments® PXI-6224 M Series DAQ module [143].

The uncertainty in the measurement is assessed in accordance with the guide to the expression of uncertainty in measurement of the International Bureau of Weights and Measures (BIPM) [144]. The notation in the following paragraphs is adopted from the guide to the expression of uncertainty in measurement and its use is limited to those paragraphs. In a measurement, the measurand Y depends on multiple input quantities X_i for which a mathematical relationship $Y = f(X_1, X_2, ..., X_N)$ exists. In reality, however, the result of a measurement is merely an estimate of the true value and, thus, is only complete with the respective uncertainty of that estimate. This output estimate y is a function of N input estimates $x = \overline{X}_i$: $y = f(x_1, x_2, ..., x_N)$. It has to be noted that this uncertainty cannot include the influence of systematic errors of, e.g. poor thermal contact of the sensors, self heating, parasitic heat loads, and thermal radiation from the surrounding. According to the BIPM [144] two different ways of evaluating uncertainty components classified as Type A and Type B standard

uncertainty exist, which are both based on probability distributions. Type A standard uncertainty $u_{\mathrm{A}}(x_i)$ calculates the uncertainty by statistical analysis of series of observations and Type B standard uncertainty $u_{\mathrm{B}}(x_i)$ applies other means [144].

In the present work the recorded data points at steady state are assumed to be independent observations obtained under the same conditions, so the Type A uncertainty evaluation method can be applied to estimate the influence of noise. The best estimate then corresponds to the arithmetic mean of the observations and $u_{\mathrm{A}}(x_i)$ is described by the experimental standard deviation of the mean [144]. The Type B uncertainty evaluation is applied to assess the resulting uncertainty from the limited accuracy of every element in the measurement chain. This includes the uncertainty due to the mathematical fit function of the sensor response curve (*fit*), the uncertainty of the sensor calibration setup (*cal*), the current source (*current*), and the voltage measurement (*voltage*). Type B standard uncertainties possess a varying strong influence on y and need to be weighed by the respective sensitivity coefficient, which corresponds to the partial derivative of y. The sum of the squared standard uncertainties (Type A and B) and sensitivity coefficients is called combined standard uncertainty $u_{\mathrm{c}}(y)$, which, following [144], is given by

$$u_{\mathrm{c}}(y) = \sqrt{\sum_{i=1}^{N} \left(\frac{\partial f}{\partial x_i} \right)^2 u^2(x_i)} \,. \tag{8.1}$$

According to the BIPM [144] the result of the measurement is expressed as $Y = y \pm k u_{\mathrm{c}}(y)$, where k denotes the so-called coverage factor [144]. In the present work $k = 2$ is chosen, which results in the uncertainty interval having a level of confidence of about 95 percent, by assuming an approximately normal probability distribution of y and $u_{\mathrm{c}}(y)$ [144].

All uncertainties are calculated in accordance with the above given references and measurement chains and the values can be found in the respective data sheets of the devices. The combined standard uncertainty of a TVO temperature sensor $u_{\mathrm{c,TVO}}\left(\overline{T}\right)$ is expressed as

$$u_{\mathrm{c,TVO}}\left(\overline{T}\right) = \sqrt{u^2_{\mathrm{A,noise}}\left(\overline{T}\right) + u^2_{\mathrm{B,fit}}\left(\overline{T}\right) + u^2_{\mathrm{B,cal}}\left(\overline{T}\right) + \left(\frac{\partial \overline{T}}{\partial \overline{U}} \right)^2 u^2_{\mathrm{B,voltage}}\left(\overline{U}\right) + \left(\frac{\partial \overline{T}}{\partial \overline{I}} \right)^2 u^2_{\mathrm{B,current}}\left(\overline{I}\right)} \,, \tag{8.2}$$

where $\overline{T}$ corresponds to the mean temperature for which the uncertainty is assessed, $\overline{U}$ denotes the mean voltage, and $\overline{I}$ is the mean current at this measuring point. The sensitivity coefficients are calculated by the differentiation of the TVO resistance-temperature correlation and replacing the resistance accordingly via Ohm's law. The combined standard uncertainty of an electric heater $u_{\mathrm{c,EH}}\left(\overline{\dot{Q}}\right)$ corresponds to

$$u_{\mathrm{c,EH}}\left(\overline{\dot{Q}}\right) = \sqrt{\overline{I}^2 u^2_{\mathrm{B,voltage}}\left(\overline{U}\right) + \overline{U}^2 u^2_{\mathrm{B,current}}\left(\overline{I}\right)} \,, \tag{8.3}$$

with $\overline{\dot{Q}}$ being the mean generated heat due to Joule heating. The combined uncertainty of the mass flow rate measurement $u_{\mathrm{c,mflow}}\left(\overline{\dot{M}}\right)$ can be correlated with the above described standard uncertainty

of the inlet temperature, the outlet temperature, and the electric heater. However, the mass flow rate mainly depends on the resulting temperature difference due to the operation of the electric heater. The influence of the uncertainty of the absolute temperature value and the pressure on the mean isobaric heat capacity in (6.12) is small. Therefore, this uncertainty contribution on the can be neglected for the combined uncertainty of the mass flow rate, as preliminary studies revealed. The in-situ adjustment of the temperature difference includes the influence of parasitic heat loads, thermal contact, and self heating. The two indicated temperatures depend on the same type of sensor, temperature correlation, current source and voltage measurement. Thus, it is assumed that all Type B standard uncertainties cancel each other out in the temperature difference. $u_{\mathrm{c,mflow}}\left(\overline{\dot{M}}\right)$ as a function of the mean mass flow rate $\overline{\dot{M}}$ is estimated with

$$u_{\mathrm{c,mflow}}\left(\overline{\dot{M}}\right)=\sqrt{\left(\frac{\partial\overline{\dot{M}}}{\partial\overline{\dot{Q}}}\right)^{2}u_{\mathrm{c,EH}}^{2}\left(\overline{\dot{Q}}\right)+\left(\frac{\partial\overline{\dot{M}}}{\partial\overline{T}_{\mathrm{in}}}\right)^{2}u_{\mathrm{A,Tin}}^{2}\left(\overline{T}\right)+\left(\frac{\partial\overline{\dot{M}}}{\partial\overline{T}_{\mathrm{out}}}\right)^{2}u_{\mathrm{A,Tout}}^{2}\left(\overline{T}\right)}\,. \tag{8.4}$$

The mathematical relation between the mass flow rate, the temperatures, and the heat is given by equation (6.12). Examples of the resulting uncertainty in the measurement of the temperature and the mass flow rate are given in Table F.4 and Table F.5, as well as in Section 7.1.

In order to optimize the accuracy of the measurement the dominating factor of the combined uncertainty should be reduced. For the mass flow rate measurement at (18.45 ± 0.07) bar and 4000 rpm, equation (8.4) equals

$$\begin{aligned}u_{\mathrm{c,mflow}}\left(0.60\times10^{-3}\,\frac{\mathrm{kg}}{\mathrm{s}}\right)=&\left[\left(2.617\times10^{-4}\,\frac{\mathrm{kg}}{\mathrm{s\,W}}\right)^{2}\left(64.678\times10^{-4}\,\mathrm{W}\right)^{2}+\right.\\&\left(8.274\times10^{-4}\,\frac{\mathrm{kg}}{\mathrm{s\,K}}\right)^{2}\left(47.946\times10^{-4}\,\mathrm{K}\right)^{2}+\\&\left.\left(8.270\times10^{-4}\,\frac{\mathrm{kg}}{\mathrm{s\,K}}\right)^{2}\left(14.621\times10^{-4}\,\mathrm{K}\right)^{2}\right]^{0.5}\\=&\left[\left(1.693\times10^{-5}\,\frac{\mathrm{kg}}{\mathrm{s}}\right)^{2}+\left(3.967\times10^{-5}\,\frac{\mathrm{kg}}{\mathrm{s}}\right)^{2}+\left(1.209\times10^{-5}\,\frac{\mathrm{kg}}{\mathrm{s}}\right)^{2}\right]^{0.5}.\end{aligned} \tag{8.5}$$

The contributions reveal that the uncertainty of the mass flow rate measurement stems to 78 % from the Type A standard uncertainty of the preceding Pt100, to 14 % from the measurement of the electric heater, and to 7 % from the Type A standard uncertainty of the subsequent Pt100. Note the differing sensitivity coefficient values of the two Pt100 sensors indicating the non-linearity of the dependency. Also it is evident in (8.5) that the noise of the preceding sensor is substantially larger than the noise from the following sensor. This could be attributed to the sensor itself or to a different mounting of the sensors. Changing the preceding Pt100 sensor or a hardware filter to reduce the noise of the temperature measurements of both sensors could efficiently reduce the uncertainty of the mass flow rate result.

F Tabulated experimental results

Table F.4: *Experimental mass flow rate results of the supercritical helium flow for different Böhmwind circulator [79] impeller speeds at two nominal pressures (*(12.21 ± 0.07) bar *and* (18.45 ± 0.07) bar*) and at* (55.0 ± 0.1) K *and* (13.0 ± 0.2) K *first and second stage of the PT420 cryocooler [78], respectively. The circulator temperature corresponds to the mean temperature between the inlet and the outlet of the circulator.*

	Run (12.21 ± 0.07) bar		Run (18.45 ± 0.07) bar	
Circ. impeller speed (rpm)	Mass flow rate (g/s)	Circ. temperature (K)	Mass flow rate (g/s)	Circ. temperature (K)
1000			0.11±0.01	67.5 ± 0.9
2000	0.15±0.02	65.0 ± 0.9	0.27±0.04	61.1 ± 0.9
3000	0.24±0.02	62.0 ± 0.9	0.44±0.05	59.9 ± 0.9
4000	0.35±0.07	60.8 ± 0.9	0.60±0.11	59.2 ± 0.9
5000	0.48±0.18	60.2 ± 0.9	0.76±0.19	58.8 ± 0.9
6000	0.56±0.08	59.8 ± 0.9	0.96±0.29	58.5 ± 0.9
7000	0.62±0.13	59.5 ± 0.9		

Table F.5: *Experimental temperature results of the sensors illustrating one full circulation loop and model calculation at two pressures and mass flow rate regimes. The system is operated at a nominal pressure of* (12.41 ± 0.07) bar *and a mass flow rate of* (0.48 ± 0.18) g/s *and* (18.74 ± 0.07) bar *and* (0.60 ± 0.11) g/s*, respectively. An external heat load of* (6.36 ± 0.14) W *and* (5.20 ± 0.12) W*, respectively, is applied at the cavity mockup. The first stage of the PT420 cryocooler [78] is regulated at* (55.0 ± 0.1) K *and the second stage is not regulated. The conditions of the experiment are inserted into the thermodynamic model and an offset heat load of* 6.3 W *from a measurement without external heating of the cavity mockup is added at the cavity.*

Description	TT853 (K)	TT850 (K)	TT854 (K)	TT852 (K)
12 bar, 0.5 g/s experiment	56.5 ± 0.9	61.3 ± 0.9	55.0 ± 0.1	58.0 ± 0.9
12 bar, 0.5 g/s model (6.3 W offset)	47.8	53.8	48.9	48.9
18 bar, 0.6 g/s experiment	56.1 ± 0.9	60.8 ± 0.9	55.0 ± 0.1	57.7 ± 0.9
18 bar, 0.6 g/s model (6.3 W offset)	48.3	54.2	49.5	49.5

Description	TT856 (K)	TT855 (K)	TT858 (K)
12 bar, 0.5 g/s experiment	21.2 ± 0.5	13.3 ± 0.6	18.4 ± 0.6
12 bar, 0.5 g/s model (6.3 W offset)	18.0	12.8	17.0
18 bar, 0.6 g/s experiment	19.7 ± 0.5	13.6 ± 0.7	16.8 ± 0.4
18 bar, 0.6 g/s model (6.3 W offset)	16.8	12.8	15.8

G Equipment specifications

Cryocooler – Cryomech® PT420

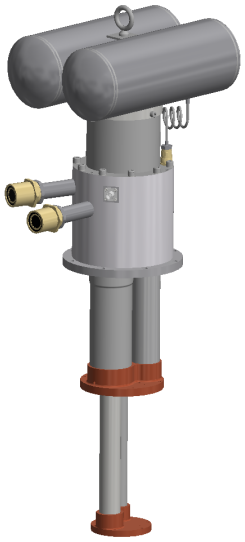

Figure G.3: *CAD drawing of the Cryomech® PT420 cryocooler [78] provided by the manufacturer.*

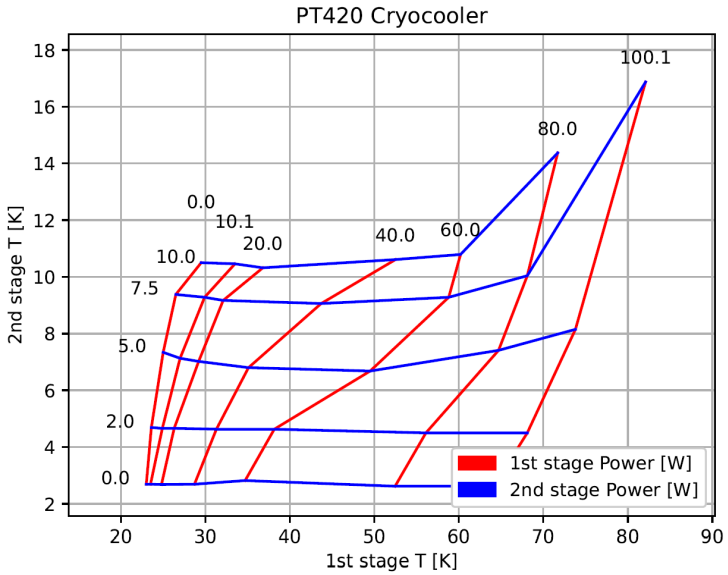

Figure G.4: *Capacity map of the Cryomech® PT420 cryocooler [78] measured experimentally at the CCCL by Busch [117]. Red and blue lines represent the powers that can be extracted at each stage at the corresponding temperatures. The maximum temperature and power measurement uncertainties are* ±0.1 K *and* ±0.1 W*, respectively.*

Cryogenic circulator – Stirling Cryogenics®

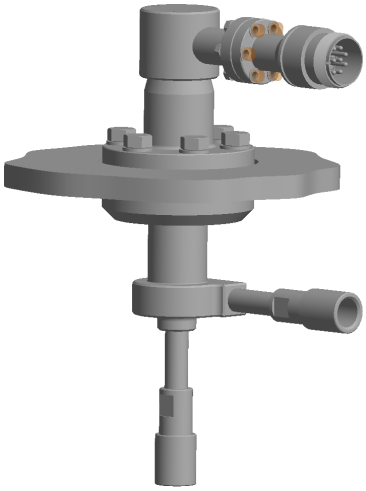

Figure G.5: *CAD drawing of the Stirling Cryogenics® Cierzo cryogenic circulator [79] provided by the manufacturer.*

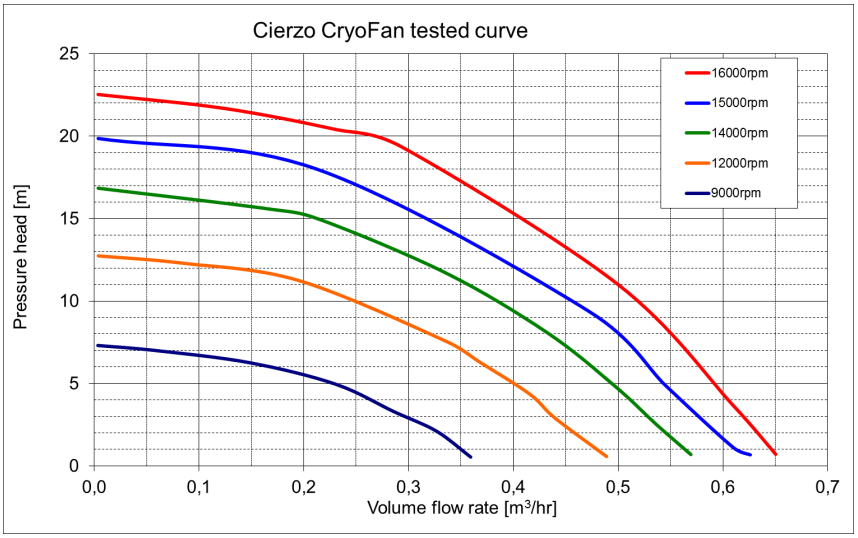

Figure G.6: *Flow curve of the Stirling Cryogenics® Cierzo cryogenic circulator [79] for different impeller speeds provided by the manufacturer.*

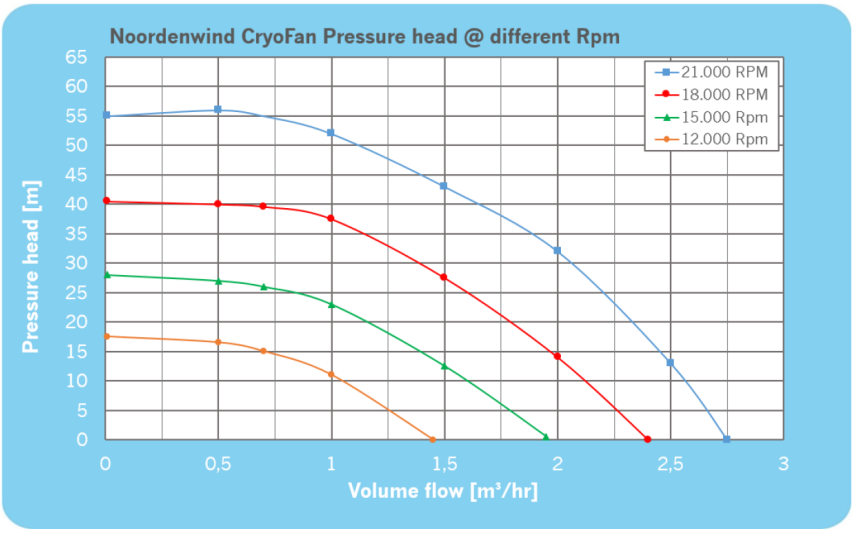

Figure G.7: *Flow curve of the Noordenwind Cryogenics® Cierzo cryogenic circulator [79] for different impeller speeds provided by the manufacturer.*

H System drawings

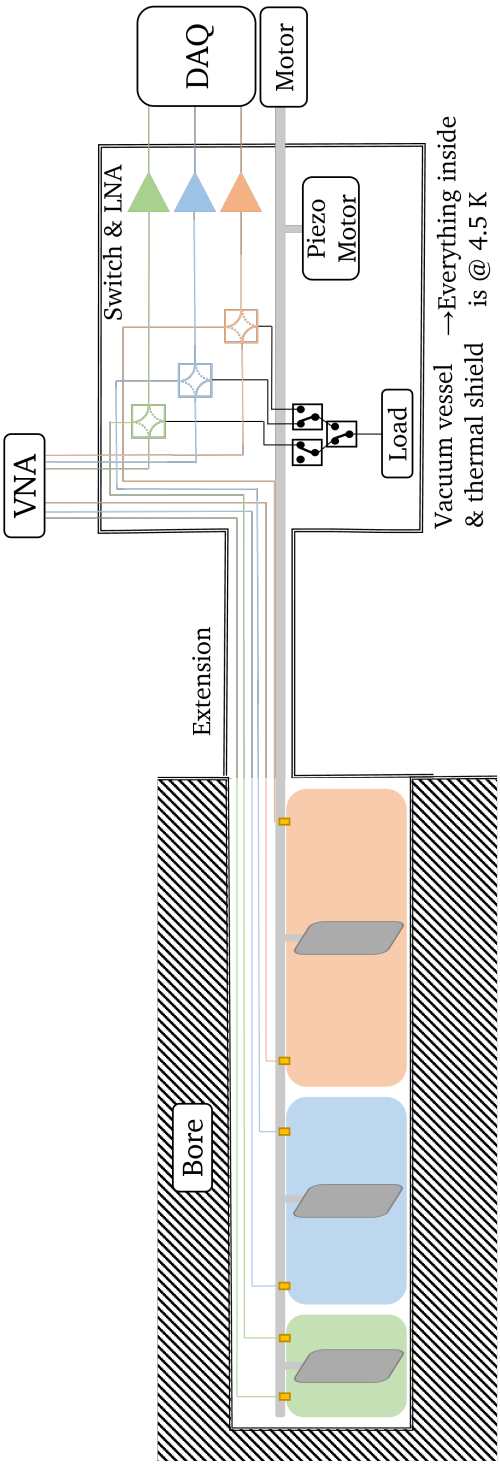

Figure H.8: *Sketch of the electrical layout and the devices required for the operation of the haloscope. Three cavities are assumed and the cooling system is omitted here.*

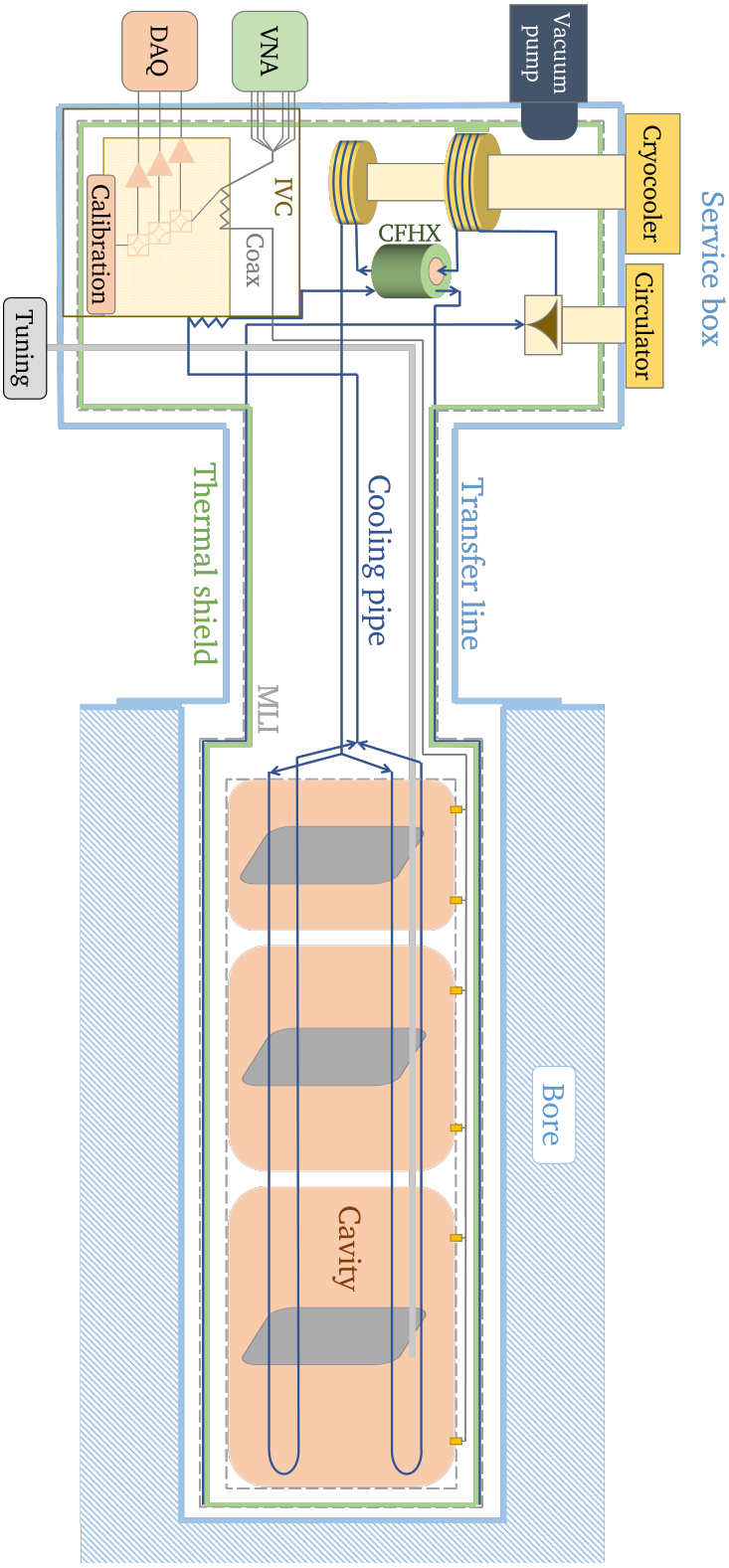

Figure H.9: *Sketch of the preliminary system layout including the electrical devices, coaxial cables, components of the remote cooling system, cooling pipes and remote cooling interfaces. Three cavities are assumed.*

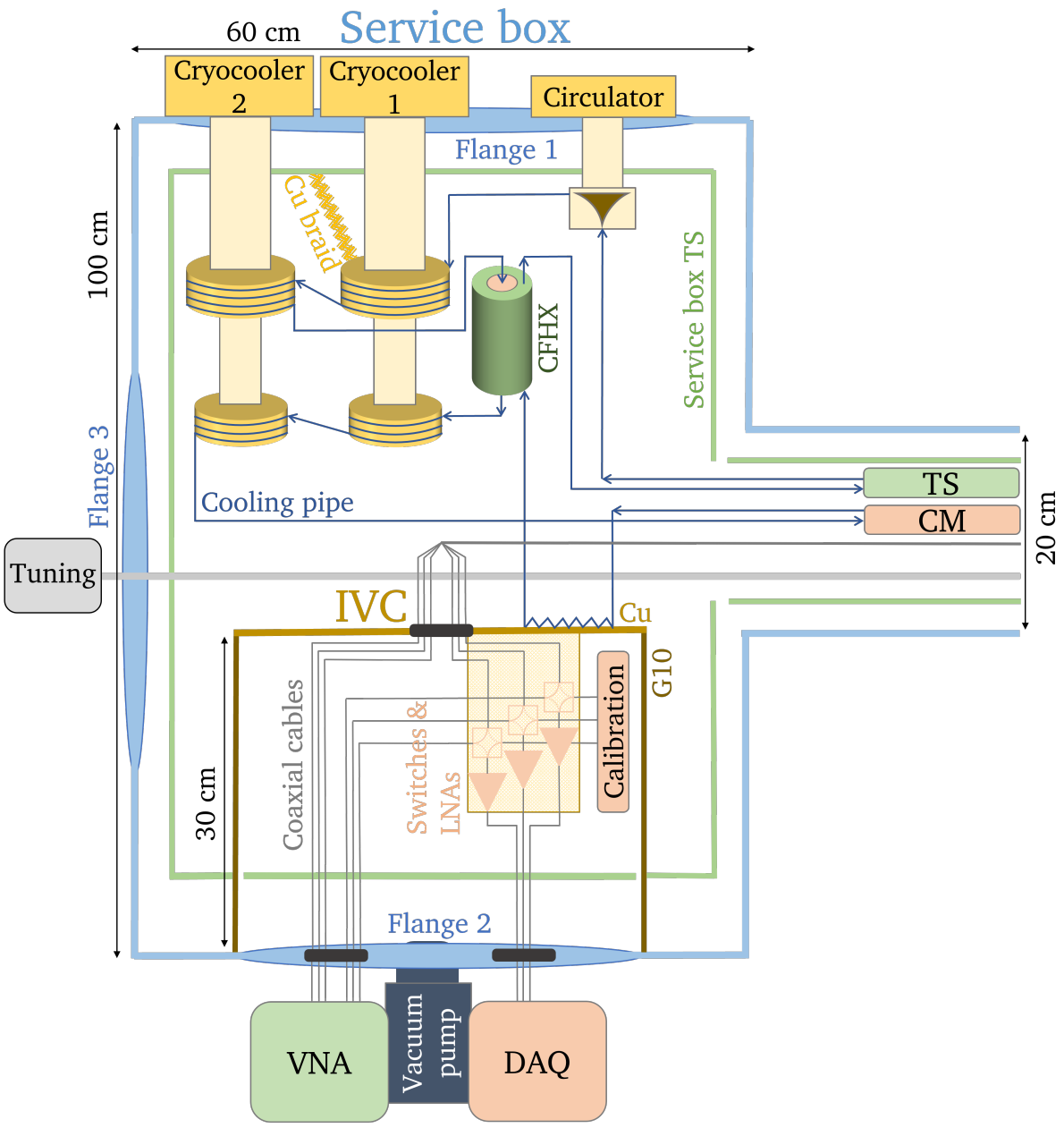

Figure H.10: *Sketch of the service box layout in a cross flange with explanatory labels and dimensions. The cooling system layout with two cryocoolers in series is depicted and the connection points of the cooling pipes are shown. The electrical equipment is installed in a separate vacuum inside the IVC inside the service box.*

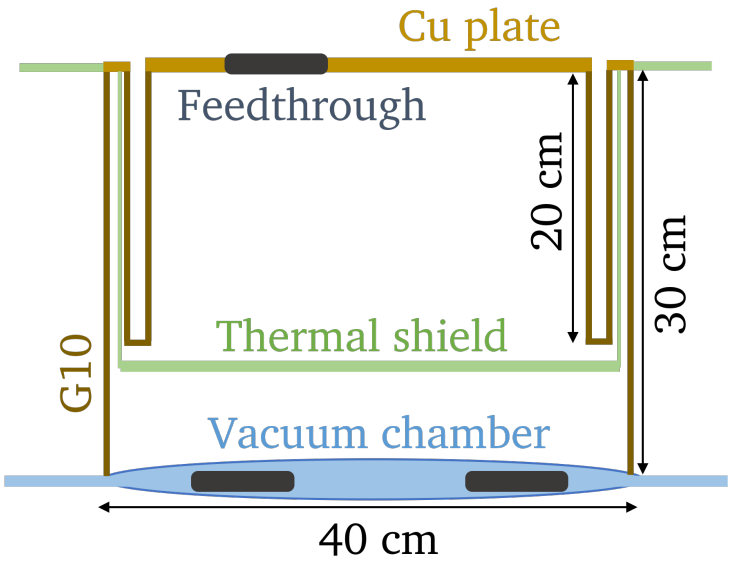

Figure H.11: *Sketch of the instrumentation vacuum chamber (IVC) structure. The IVC is installed in the service box and allows to create a separate vacuum environment for the electrical equipment. The electrical equipment is omitted in the sketch.*

I Pictures

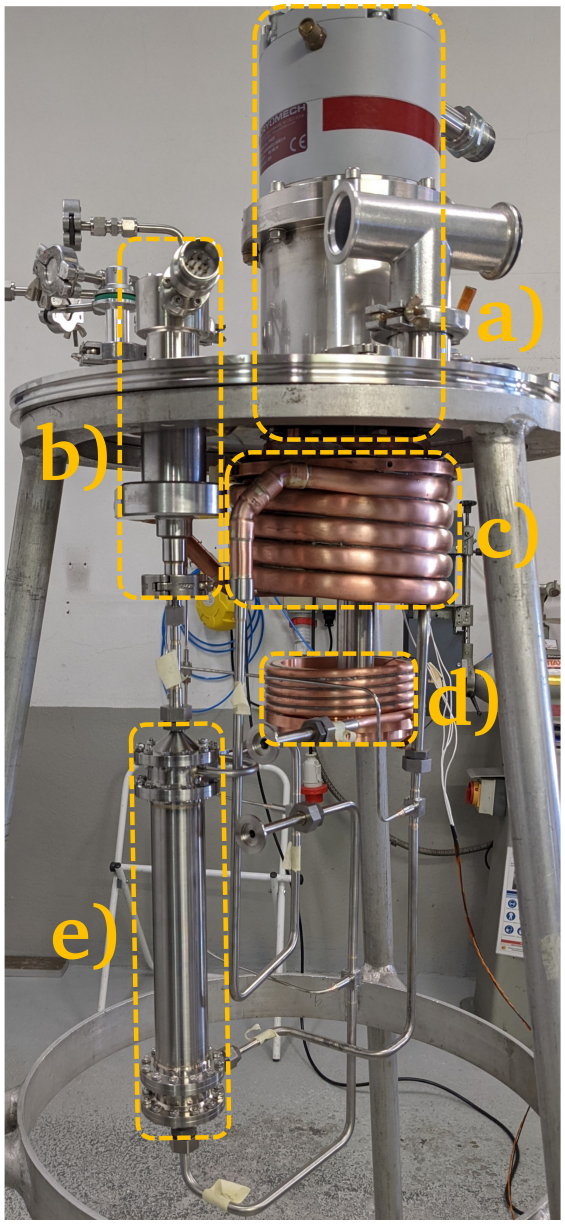

Figure I.12: *Experimental setup with only the fundamental components installed. a) Cryocooler, b) cryogenic circulator, c) coiled pipe HEX of the first stage, d) coiled pipe HEX of the second stage, e) CFHX.*

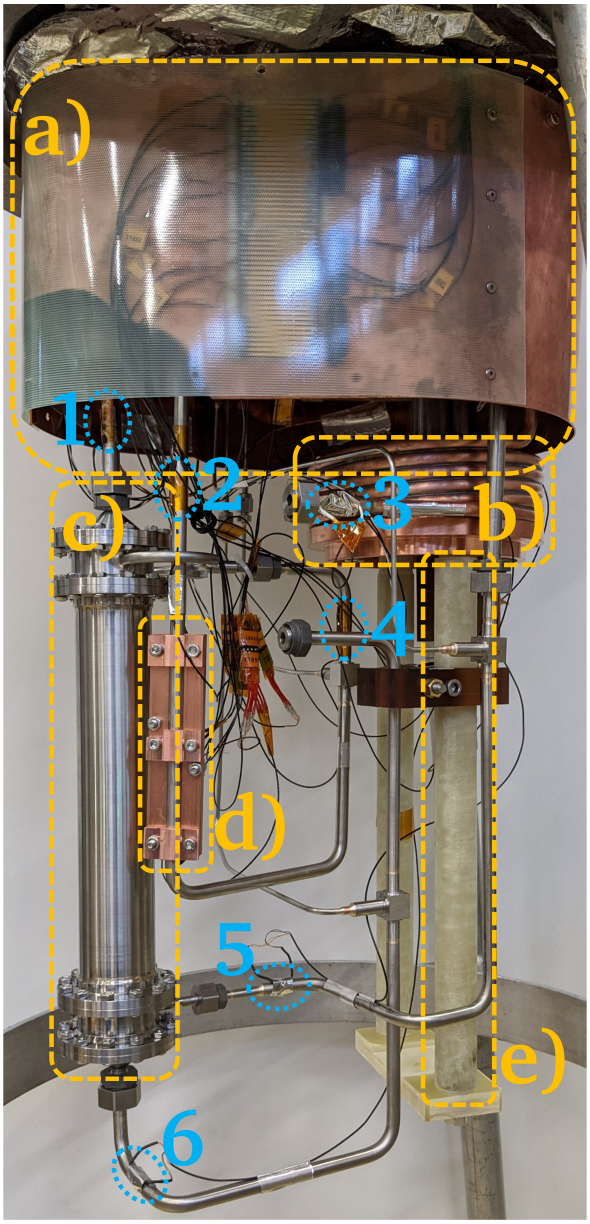

Figure I.13: *Experimental setup with the sensors mounted. The visible temperature sensors are numbered and specified according to the naming in Figure 6.5. a) Copper thermal shield thermalized at the first stage including the thermalization of the cables of the sensors, b) coiled pipe HEX of the second stage, c) CFHX, d) electrical heater mounted on the cooling pipe with a copper block, e) G10 rod (for stability during installation). 1: TT853, 2: TT851, 3: TT857, 4: TT852, 5: TT856, 6: TT858.*

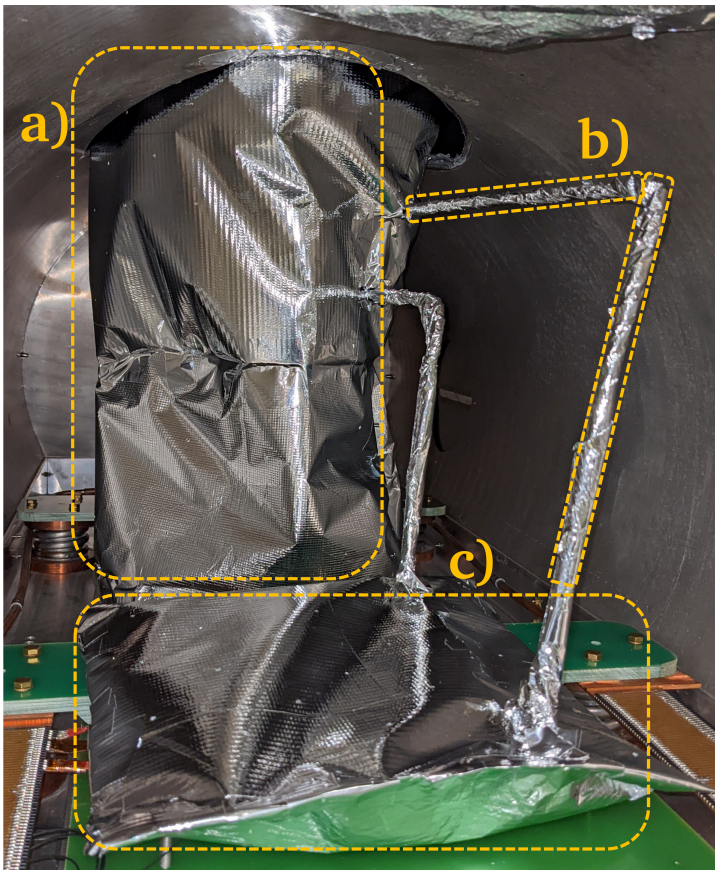

Figure I.14: *Experimental setup covered by MLI and installed in the cryostat. The background shows the liquid nitrogen thermal shield. a) MLI covered insert of the cooling system. b) Cooling pipe transporting the cooling power from the cooling system to the remote application to be cooled. The cooling pipe is protected from radiation by a single layer of MLI. c) MLI covered cooling application. In the present setup this is imitated by an electrical heater.*